Copyright

by

Dat Truong Ma

2007

The Dissertation Committee for Dat Truong Ma
Certifies that this is the approved version of the following dissertation:

Laser Processing of $Tb_{0.3}Dy_{0.7}Fe_{1.92}$ Films

Committee:

Desiderio Kovar, Supervisor

Michael Becker

John Keto

Llewellyn Rabenberg

Arumugam Manthiram

Laser Processing of $Tb_{0.3}Dy_{0.7}Fe_{1.92}$ Films

by

Dat Truong Ma, B.S.; M.S.

Dissertation

Presented to the Faculty of the Graduate School of
The University of Texas at Austin
in Partial Fulfillment
of the Requirements
for the Degree of

Doctor of Philosophy

The University of Texas at Austin
December, 2007

Dedication

This work is dedicated to my parents and grandparents for their sacrifices and hard work.

Acknowledgements

During my time at the University of Texas at Austin, I have benefited from a great number of individuals. First and foremost, I would like to thank my advisor, Dr. Desiderio Kovar, for his patience, guidance, expertise and support. I would also like to thank my co-advisors, Dr. Michael Becker and Dr. John Keto, for their time and contribution. In addition, I would like to thank Dr. Ji-Ping Zhou and Dr. Llewellyn Rabenberg for their support, especially on the TEM. Finally, research would be difficult without the assistance and kindness of many dear friends and colleagues.

Laser Processing of $Tb_{0.3}Dy_{0.7}Fe_{1.92}$ Films

Publication No._____________

Dat Truong Ma, Ph.D.

The University of Texas at Austin, 2007

Supervisor: Desiderio Kovar

In the past decade, there has been an increased interest in magnetostrictive materials for micro actuators and sensors. Of particular importance are the Fe_2R intermetallics, where R = Tb, Dy. In this study, films of $Tb_{0.3}Dy_{0.7}Fe_{1.92}$ were prepared by three laser processing techniques (pulsed laser deposition, flat plate ablation and laser ablation of microparticles) to explore the effect of processing parameters on particle size, crystallinity and magnetic properties. The laser used in the experiments was a KrF laser with a 12 ns pulse width.

Pulsed laser deposition of an alloyed target in vacuum produces dense amorphous films with the similar composition to the target, low coercivity (46 Oe) and good magnetostriction ($\lambda_{\|}$ = 305 ppm at 2300 Oe). Flat plate ablation and laser ablation of microparticles produced amorphous nanoparticles at 1 atm. The particles were subsequently jet deposited onto substrates to form thick films. Nanoparticle films produced by flat plate ablation resulted in oxidized and segregated particles due to extended, non-uniform plume expansion, laser target modification, and open porosity. Laser ablation of microparticles produced thick films with M_s = 13.8 emu/g. Two types

of annealing treatments were performed to close porosity and increase Youngs modulus. Annealing of LAM films at temperatures up to 700˚C *in-situ* and 950˚C in a reducing atmosphere did not result in coarsening of the particles or crystallization of the Laves phase due to the core-shell structure of nanoparticles (rare earth oxide shell, Fe rich core) brought about by oxidation-induced segregation.

Table of Contents

List of Figures

List of Tables

Chapter 1

Introduction

1.1 Motivation

Sensors and actuators are an ubiquitous part of everyday life. Mechanical sensors monitor mechanical forces and displacements by converting mechanical signals to electrical signals. Actuators control mechanical displacement by converting electrical signals to mechanical movements. These devices are unobtrusive yet integral components of common instruments such as printers, cars, airplanes, etc.

There has been a great deal of research and development since the 1970s to reduce the size of devices and to integrate two or three functions (sensors, actuators and signal processors) onto a single micro-electro mechanical system (MEMS) device. MEMS is generally used to describe such devices with sizes that range from 1 μm to 1000 μm. Miniaturization has reduced the material required for each device and enhanced device performance by reducing weight, cost, and power consumption. These advances have led to development of new application for MEMS devices such as drug delivery systems, fiber optic switches, deformable aircraft wings, and optical computing systems.

There are a number of choices for the active material that is used in MEMS devices. Shape memory actuators are based on alloys that change shape in response to temperature variations. Thermal actuators rely on thermal expansion to produce motion. Chemical actuators are polymers or waxes that swell or contract due to changes in the pH of the surrounding environment. Although all of these materials can develop large strains, their response times are especially slow.

Piezoelectric materials such as lead zirconate titanate (PZT) are often used in MEMS devices because they can function as strain sensors and actuators. They are capable of producing large forces, have the capability of achieving high strain, and can be driven at MHz frequencies.[1] Piezoelectrics are reversible, meaning they deform in the response to an applied potential (actuator) or generate electric charge due to applied stress (sensor). Unfortunately, maximum strain is limited to ~0.1%.

Another subclass of smart materials being currently being explored for MEMS applications is magnetostrictive materials. These materials deform reversibly in the presence of an applied magnetic field. They offer several advantages over PZT. Magnetostrictive materials are also capable of large forces, can exhibit strains up to four times larger than PZT and do not require hard wiring.[2] However a drawback in bulk magnetostrictive materials is they can only be driven up to kHz frequencies due to eddy current losses. In addition, actuation of bulk magnetostrictive materials usually requires large magnetic fields. Methods are needed for reducing the magnetic fields required to drive magnetostrictive actuators while maintaining or enhancing their force capacity.

1.2 Magnetostriction

Magnetostriction is defined as a change in physical dimensions of a material in response to a change in its magnetization, where magnetization is the magnetic moment per unit volume or mass.[3] Magnetostriction is a manifestation of magnetoelasticity or the coupling of the elastic and strain properties of a material with its magnetic properties. Magnetic moments are the result of imbalances in electron orbital and electron spin angular momenta. In addition, partially filled orbital shells result in nonspherical electron density. Although many atomic elements have these imbalances, most solids are not magnetic. This is because when atoms bond with each other, they usually share electrons in such a manner where the disproportional spin and orbital contributions are negated. Thus, the majority of solids that retain any magnetism are made of elements whose imbalances are in the inner orbital shells: transition metals, rare earths and the actinides.

Magnetostriction can be observed and brought about by varying the temperature or applied magnetic field. In volume magnetostriction, cooling below the Curie temperature (T_c) causes a spontaneous change in all dimensions of the sample. This is due to cooperative ordering of magnetic moments in many atoms (typically 10^{12}-10^{15} atoms) into domains at the Curie temperature.[4] Above the Curie temperature, thermal fluctuations dominate and atomic moments are random. Below the Curie temperature, magnetic exchange interactions dominate and the moments are aligned (spontaneously magnetized) within a domain. In other words, upon cooling the material goes from a paramagnetic (disordered) state above the Curie temperature to a ferromagnetic (ordered) state below. Figure 1.1 illustrates clusters of randomly oriented atoms above T_c aligned into ordered domains below T_c. In Joule magnetostriction, application of a magnetic field below T_c causes a change in dimensions with very little change in volume. The dimensional change that is observed during Joule magnetostriction is caused by the aligning of ordered domains in an applied magnetic field. Joule magnetostriction is the property of interest in this research and will simply be referred to as magnetostriction from this point forward. The strain produced by such a rotation is

$$\lambda = \Delta L / L, \tag{1.1}$$

where λ is magnetostriction, ΔL is the change in length and L is the original length.

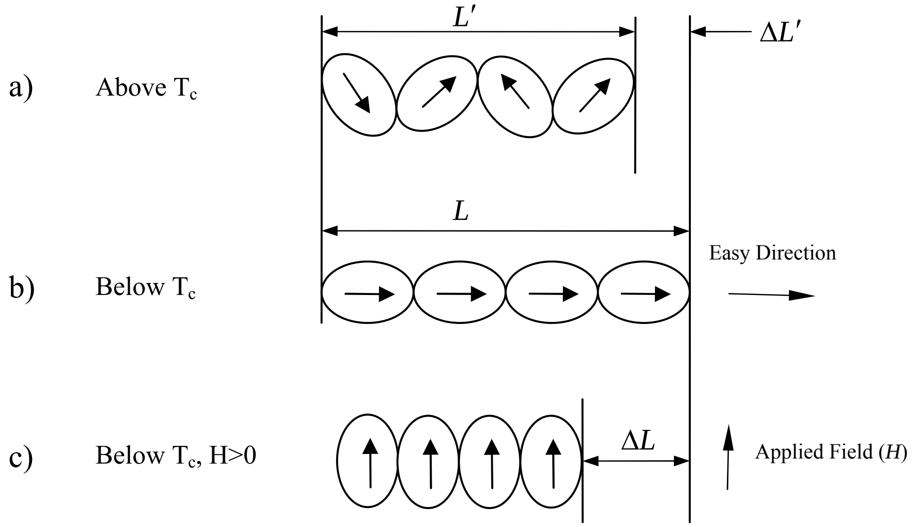

Figure 1.1: Illustration of magnetostriction showing progression from a) paramagnetic behavior above T_c to b) ferromagnetic behavior below T_c. c) Alignment of the domains results in strain under application of a magnetic field at temperatures below T_c.

From the interactions between spin-orbit-lattice, we can show that the degree of magnetostriction in a solid depends on how strong the coupling is between the direction of spin and the orientation of the electron orbital.[5] As stated previously, below T_c there is a spontaneous magnetization in domains or a preferred spin and orbit orientation. The resulting moment vector is known as the easy direction. If a field reorients the spin from the easy direction, then the orbital tries to rotate to retain the same relative position. However, orbital motion is opposed by strong orbital lattice interaction. The energy required to rotate the spin from the easy direction is the anisotropy energy. Spin-orbit coupling is usually weaker than orbit-lattice coupling and thus spin-lattice coupling is usually weak.

If spin-orbit coupling is very strong, the spin moment is “rigidly attached” to the anisotropically shaped electron cloud. In a sufficiently high field, they rotate together in response to a rotating field. Rotation of the anisotropic electron cloud changes the internal energy and lowers crystal symmetry. Figure 1.2 is a two dimensional atomic illustration of an ideal case where spin moment and orbital shell are reoriented away from the easy direction by an applied magnetic field. This motion forces neighboring atoms in one dimension to move further apart while neighboring atoms in the other dimension move closer together. The interaction between spin moment, electron cloud and neighboring atoms is the magnetoelastic coupling that is responsible for (Joule) magnetostriction.

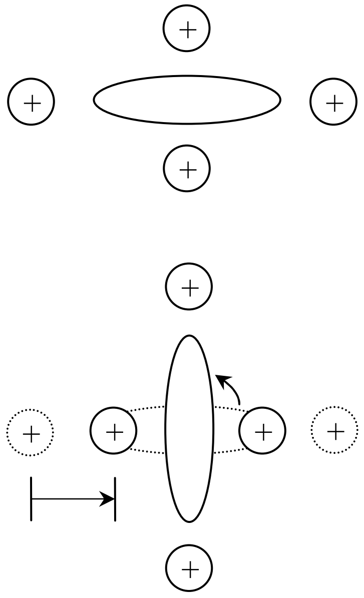

Figure 1.2: Shifting of neighbors due to a rotated spin-orbital.

Macroscopic magnetostrictive strain requires reorientation of magnetic moments in many atoms. For a given volume of material, the extent of moment reorientation in an applied field is the magnetization. Since moments can be rotated without moving the electron orbital (weak spin-orbit coupling), magnetization is by no means a direct measure of magnetostriction. However, for the same material at a given field, the ratio of magnetizations is a reasonable surrogate for measuring magnetostriction.

1.3 Magnetostrictive Materials

All ferromagnetic materials exhibit some amount of magnetostriction. However, most materials only exhibit a small amount of magnetostrictive strain because the amount of reorientation of the electron clouds in an applied field is quite low. This is not true of rare earth metals whose electron imbalance is in the tightly bound 4*f* orbital shell. In addition to spin imbalances, the partially filled 4*f* shell leads to a non-spherical electron cloud. Since the 4*f* shell does not participate in bonding, spin orbit coupling is strong. Dy and Tb have the largest known magnetostrictions because of their oblate electron cloud. However, the non-bonding magnetic orbital is isolated and magnetic exchange is weak. Thus, the spontaneous magnetic ordering of rare earths only occurs at very low temperatures. Although Dy and Tb have large magnetostriction, large strains only occur below room temperature which obviates them from most applications.

In 1971, research on low temperature magnetostriction in rare earth elements and high temperature magnetostriction in rare earth alloys at the Naval Ordnance Laboratory resulted in the discovery of an intermetallic compound capable of above room temperature strains of 10^{-3}. These giant magnetostrictive (GMS) alloys combined the high T_c of transition metals with the large magnetostriction of rare earth elements.[6] Of the GMS alloys studied, $TbFe_2$ was found to have the greatest magnetostriction above room temperature. $TbFe_2$ is a Laves phase (C15) crystal and has high crystal anisotropy with λ_{111} much greater than λ_{100}. Figure 1.3 is a reproduction of experimental results on the Tb-Fe system by Clark et al. that shows the change in magnetostriction with variation in composition. In this and similar systems, composition is critical because magnetostriction quickly degrades with either rare earth rich or iron rich compositions.

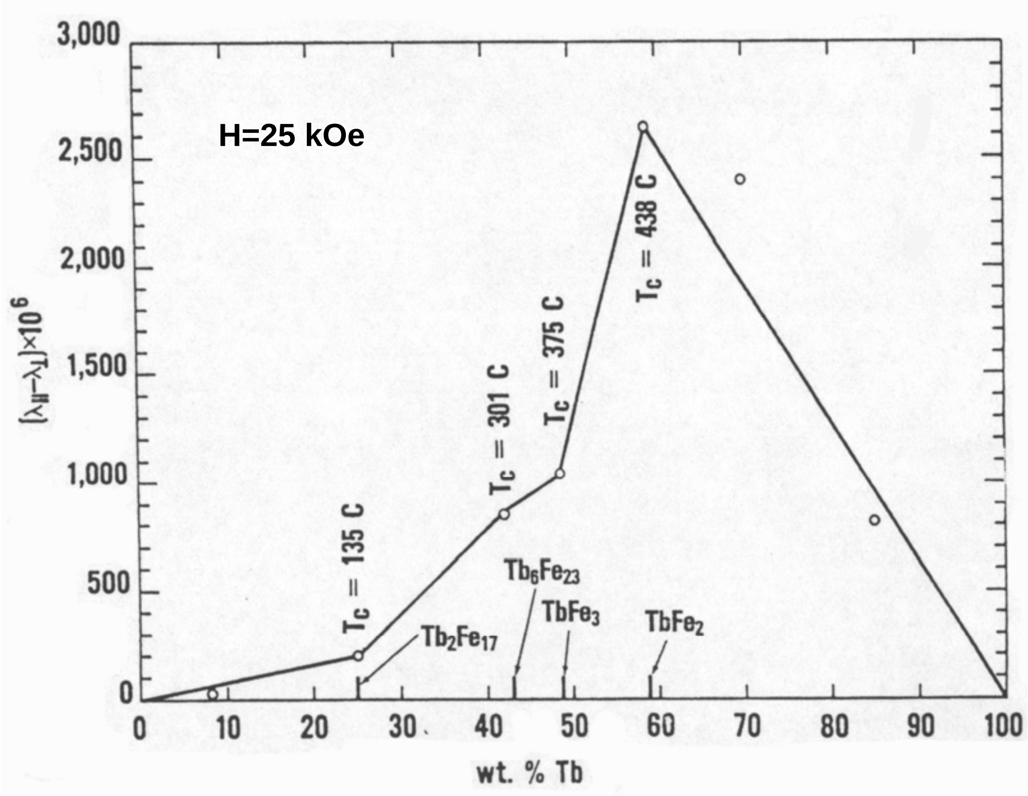

Figure 1.3: Magnetostriction as a function of composition in the Tb-Fe system.[6]

1.4 Magnetic Properties

An ideal GMS actuator should be capable of large deflections at low external fields with small coercivities, the applied field required to reduce the magnetization to zero from a magnetized state. In order to achieve maximum deflection with minimum power input, the magnetization should saturate at the low applied fields because magnetostriction is tied to magnetization. Ideally, coercivity is small so that low fields are required to reverse the magnetostriction. Low fields can be generated and cycled quickly so the actuator can be driven at high frequencies. Simply stated, these parameters are chosen to maximize the ratio of work output to energy input combined with the capability of operating the device at high frequencies.

Since the magnetic properties of materials can be tailored to reduce the required magnetic saturation field (H_s) and coercivity, we start by choosing the Fe-Tb system because it has the highest magnetostriction above room temperature. Next the aim is to reduce H_s by changing composition and microstructure. H_s is related to the magnetic anisotropy constant (K) and saturation magnetization (M_s) by [7]

$$H_s = \frac{2K}{M_s}. \tag{1.2}$$

H_s can be reduced by lowering K and by increasing M_s. M_s reaches a maximum in the Fe-Tb system when the ratio of the iron to rare earth is 2:1. K is lowered due to exchange interaction when the grain size or film thickness is smaller than the ferromagnetic exchange length (L_o),

$$L_o = \varphi_o \sqrt{\frac{A}{|K_1|}}. \tag{1.3}$$

φ_o is a proportionality constant, A is the exchange stiffness and K_1 is the local magnetic anisotropy constant. Typical values for Fe alloys are $L_o \approx$ 20-40 nm. Small grains or particle sizes have the added benefit of lowering the coercivity. This is because when grains or particles are small, each act as a single domain.

Additional reduction of K is possible with elements that have the same sign magnetostriction and opposite anisotropy. Pseudo-binary systems that met these criteria were $Tb_{1-x}Dy_xFe_2$, $Tb_{1-x}Ho_xFe_2$ and $Tb_{1-x}Pr_xFe_2$. $Tb_{0.7}Dy_{0.3}Fe_{1.92}$ was found to have the highest room temperature magnetostriction of the anisotropy compensating systems.[2] It is commercially available from Etrema Products Inc. (Ames, IA).

1.5 Previous Work on $Tb_{0.3}Dy_{0.7}Fe_{1.92}$

1.5.1 Thin Film Processing of $Tb_{0.3}Dy_{0.7}Fe_{1.92}$

Thin films (< 2 μm) of GMS compounds that function well as sensors and actuators are commonly made using thin film processing methods such as sputtering.[8] High quality $Tb_{0.3}Dy_{0.7}Fe_{1.92}$ films with soft magnetic properties appropriate for sensors and actuators have been produced by ion beam sputtering (IBS). In this process, an Ar ion beam is extracted at 10 kV and directed at a target surface of $Tb_{0.3}Dy_{0.7}Fe_{1.92}$. The plasma ejects atomic material from the target and deposits it on the substrate. As-deposited films are nanocrystalline with grain sizes smaller than a few nanometers. Films have been produced using IBS with a saturation magnetization (M_s) of 15.2 emu/g and a coercively (H_c) < 100 Oe. This process produces films of $Tb_{0.3}Dy_{0.7}Fe_{1.92}$ with good magnetic properties but the deposition rate is very slow (0.01 to 0.3 nm/sec). As a result, IBS is limited to depositing thin films for sensor applications. These films are very responsive because their low coercivity allows the GMS material to act like a soft magnet. However, thin films do not produce enough displacement or force to be used in most actuators.

1.5.2 Thick Film Processing Method

Applications for magnetostrictive materials could be extended to include micropumps, microvalves, optical deflectors, and ultrasonic devices if thicker films could be incorporated for greater deflection and force capacity. A simple means for increasing the deflection and force capacities is to increase the thickness of the films. However, methods for producing thin films cannot be extended to thick films because they are either too slow or require high temperatures. High processing temperatures can cause film fracture or debonding if large stresses arise between the film and substrate from thermal expansion mismatch.

Thick films (> 10 μm) of GMS materials have been produced previously by embedding microparticles in a polymer matrix.[9, 10] More recently, thick magnetostrictive films were made with microparticles that were oriented in the [112] direction. The milled "needles" of $Tb_{0.3}Dy_{0.7}Fe_{1.92}$ had an aspect ratio of at least 2 to 1 and a particle length of 100-500 μm. Measured magnetostriction of these films was about 33% of bulk $Tb_{0.3}Dy_{0.7}Fe_{1.92}$. No coercivity data was provided but it would be expected to be large due to the large size of the particles. These films are capable of generating larger displacements compared to thin films by IBS. However, performance (displacement and modulus) is degraded by the inactive polymer matrix and the micron-sized crystalline particles that require large fields to operate.

1.6 Methods for Producing Nanoparticle Films

An alternative method of fabricating thick film magnetostrictive actuators is to fabricate them from nanoparticles. Nanoparticles can be produced by a number of methods. High energy attrition milling uses mechanical collision to reduce the size of material to nanometer size scales. The particles can then be consolidated and sintered to produce bulk solids or thin films. Metals, composites, ceramics and intermetallic nanoparticles have been created using this technique. For example, titanium particles have been made with steel milling media after 30 hours.[11] Average particles size is 35 nm. However, the size distribution is large with particles ranging from 12-70 nm. In addition, attrition milling often adds impurities from the container and milling media to the powder.

Chemical synthesis methods have produced a wide variety of high quality nanoparticles and other nanostructures.[12-14] In this process, nanoparticles precipitate from a solution of organometallics compounds, solvents and surfactants. This process is scalable and there are many examples of nanoparticles grown in this manner. Although particles with a very narrow size distribution can be produced, each particle is coated with an inactive organic layer. Also, many chemicals used in this process are toxic to the environment.

Inert gas condensation is another method to produce nanoparticles. Materials are evaporated either by flash evaporation or by a heating above the boiling point.[15] The material is vaporized into an inert atmosphere where nanoparticles coalesce. Unlike methods discussed previously, the resultant nanoparticles from condensation are pure but since there is no organic present the nanoparticle agglomerate. In addition, films can be made directly using this method.

1.7 Laser Methods for Film Production

Pulsed laser deposition (PLD) is versatile method of making nanoparticles and high quality films.[16] In this method, a bulk material is irradiated with a high energy beam. In this interaction, the target is instantly vaporized and a plume of material is ejected. Films can be made in vacuum by directing the plume of high energy material onto a substrate. In addition, nanoparticles and nanostructured films can be created by laser ablation. At sufficiently high pressures, vapor from ablated flat plates[17] (flat plate ablation, FPA) or micron sized particles[18] (laser ablation of microparticles, LAM) nucleate and coalesce in an inert atmosphere. If ablation is performed in an aerosol, then the particles can be deposited into films by impaction. In contrast to some of the other methods, films can be made by different laser processing techniques without exposing highly reactive nanoparticles to the atmosphere. Materials processed by lasers are also pure because the only possible material interaction is between the target material, the photons and inert gas. Details about PLD, FPA and LAM and their experimental setups are provided in Chapter 2.

1.8 Research Objectives

To date there have been few attempts at making GMS films for eventual inclusion in MEMS devices by laser processing. The goal of this research project was to study the relationships between processing parameters, material nano and microstructures, and magnetic properties of $Tb_{0.3}Dy_{0.7}Fe_{1.92}$ films produced by laser ablation. In this work, films made by three laser processing methods were fabricated and investigated. A discussion of laser processing techniques and experimental setup is presented in Chapter 2. Because working with an intermetallic with rare earth and Fe elements at plasma temperatures presents special challenges, a portion of Chapter 2 is dedicated to the handling of raw material and diagnostics used to monitor laser ablation. Chapter 3 continues with analysis techniques used to analyze deposited films of $Tb_{0.3}Dy_{0.7}Fe_{1.92}$. Chapters 4, 5, and 6 show the results of films made by PLD, FPA and LAM, respectively. Chapter 7 discusses the combined results and future direction.

Chapter 2

Laser Processing

2.1 Introduction

In this chapter, the effects of three laser processing methods, pulsed laser deposition (PLD), flat plate ablation (FPA), and laser ablation of microparticles (LAM), on $Tb_{0.3}Dy_{0.7}Fe_{1.92}$ are discussed. The major experimental components, their design and the details of each processing method are described in the following sections. Additionally, since the Tb, Dy and Fe are reactive elements, there are special precautions that must be taken when processing these materials at high temperatures. The equipment and procedures to monitor and minimize reactions with gasses are presented.

2.2 Experimental Equipment

The laser used is a Lumonics PM-800 laser with KrF (248 nm wavelength) gas as the lasing medium. The composition of the gas mixture is 0.1% F_2, 2% Kr and 97.9% Ne. The laser has a pulse length of 12 ns and is capable of repetition rates up to 200 hz. The beam exiting the laser has a rectangular cross section of 35 mm × 12 mm.

The three laser processing techniques are conducted in an ablation chamber and two large ultra high vacuum (UHV) chambers (Figure 2.1). The ablation chamber is used to make nanoparticles in flowing gas by flat plate ablation and LAM. Nanoparticles are deposited from the ablation chamber through a nozzle to chamber 1 (C1). Chamber 2 (C2) is used for PLD. In addition, C2 has a heating stage that allows *in-situ* annealing in high vacuum. A substrate is loaded through a load lock that can be purged with a dry pump. A magnetic arm is used to move samples from the load lock to C1 and C2. The UHV chambers are pumped by a turbo molecular pump attached to C1 and a cryopump attached to C2. The chambers are usually kept at 1×10^{-8} Torr or lower when deposition is not taking place.

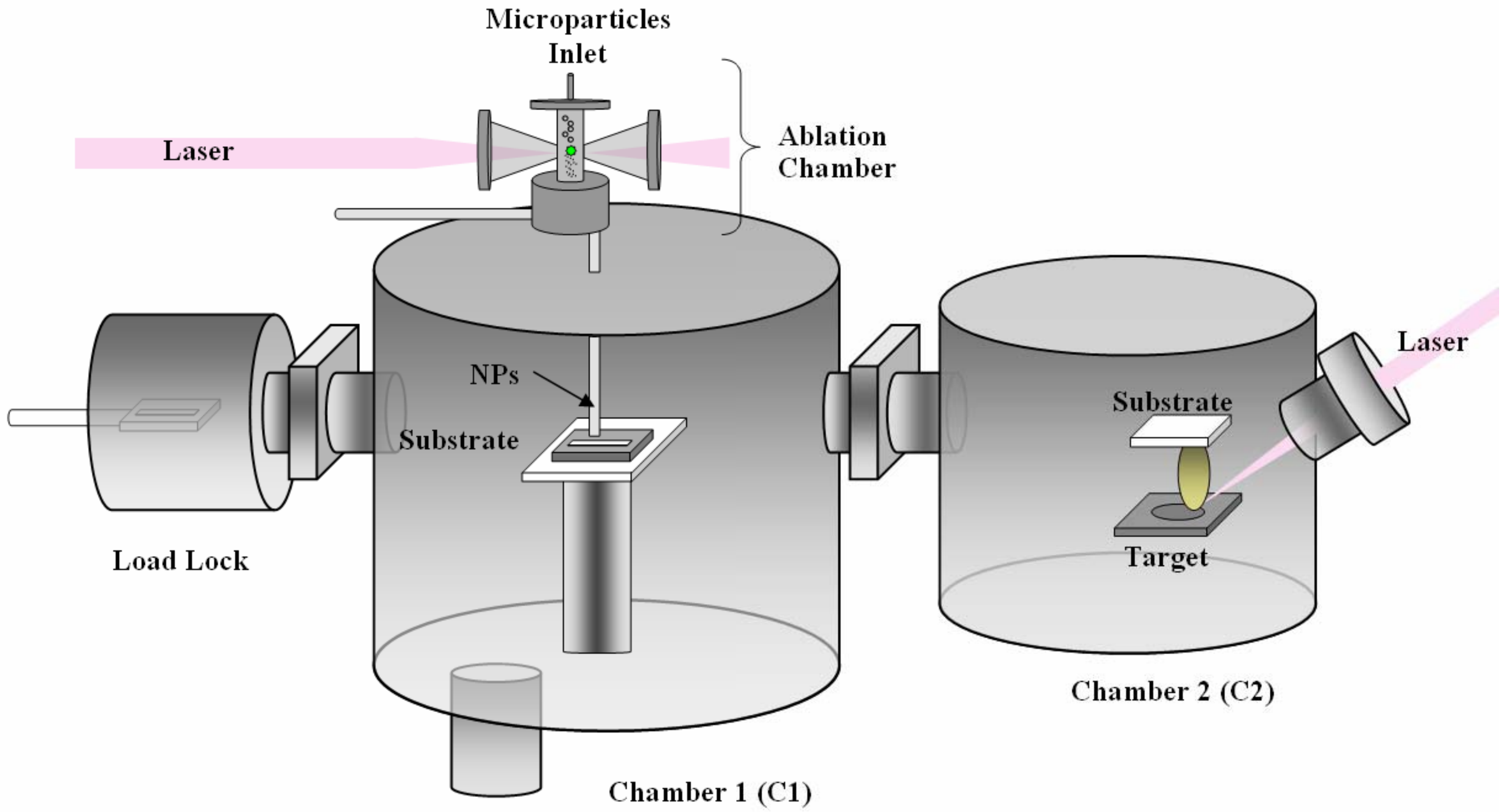

Figure 2.1: Schematic of laser processing system

2.3 Pulsed Laser Deposition

2.3.1 PLD Process Description

Pulsed laser deposition (PLD) is a thin film deposition process that relies on intense pulses of energy to eject target atoms. PLD is a relatively new technique that started in the 1970s with the advent of the short pulse Q-switched laser. PLD gained much more attention in the 1980s when growth of the low temperature perovskite superconductor, $YBa_2Cu_3O_7$, by PLD was demonstrated and perfected. Although the experimental setup for PLD can be very simple, the laser-target interaction is very complex. A brief description is given below. A more in-depth treatment can be found in text by Chrisey and Hubler.[16]

In its simplest form, a target and substrate sit parallel to one another inside a vacuum chamber (Figure 2.2). A laser pulse is focused and directed through a vacuum chamber window on the surface of the target. Photons are absorbed by the target. Electronic excitation of the target atoms is converted into thermal, chemical and mechanical energy.[19] This results in the formation of a plasma and ejection of excited atoms. In addition, a molten layer or Knudsen layer forms on the target. The vaporization process creates a large recoil pressure on the molten layer and ejects large droplets of molten material. The plume of ejected material travels normal to the target surface and reaches the substrate in milliseconds. At low vacuum pressures, the mean free path is high and thus the ejected material arrives at the substrate with high kinetic energy. The resultant film is dense and can be either crystalline or amorphous depending on material and cooling rate. At high vacuum pressures, the mean free path is low and the vaporized material in the plume nucleates and particles coalesce. The density and particle/grain size of the film depends on the pressure and gas species. Gases can also be introduced to intentionally react with the ejected material to form compounds or to help preserve target stoichiometry in the case of compounds that easily dissociate (e.g. AlN).

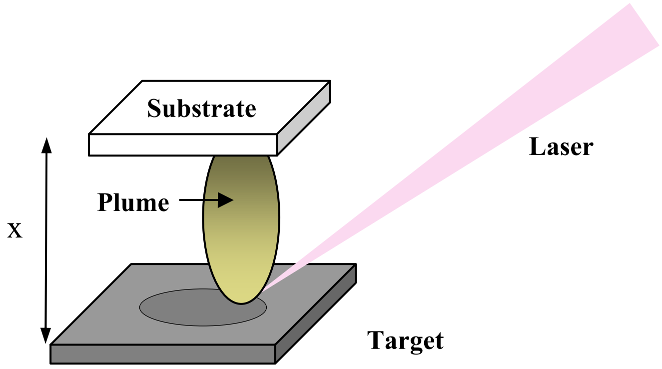

Figure 2.2: Schematic of PLD process. x denotes the target-to-substrate distance.

The power required to evaporate the target material, P, is dependent on the sublimation energy of the target material and the size of the heat affected zone. Combined with the pulse length,

$$P = \frac{2U_s(K\tau)^{1/2}\rho}{\tau} = 2U_s K^{1/2}\tau^{-1/2}\rho \qquad (\mathrm{W/cm^2}) \qquad (2.1)$$

where U_s is the sublimation energy, K is the thermal diffusivity, τ is the pulse length, and ρ is the density of the target.[20]

There are many advantages to the PLD method for producing films. 1) The purity of films made by PLD is usually high because the only possible interaction is between the gas species and the target material. 2) For low vacuum pressures, the kinetic energy of ejected material is high and the resultant film can be as dense as bulk material. 3) For higher vacuum pressures, nanoparticles and nanostructured films can be produced. 4) Multi-component target stoichiometry is often preserved because the rapid heating rate and rapid removal rate of material limits atomic segregation.

There are also a few disadvantages to producing films with PLD. 1) The ejected plume is highly directional and can lead to non-uniform film thicknesses. 2) "Splashing" of the molten target can produce large micron sized defects (for optical films) on an otherwise smooth film. 3) Although the PLD method can deposit high quality films, it is limited to deposition rates of nanometers per minute.

2.3.2 PLD Experimental Setup

PLD experiments of $Tb_{0.3}Dy_{0.7}Fe_{1.92}$ were done in C2 under vacuum. Although, the PLD chamber is pumped with a turbo pump, due to absorbed gases on the target, pressures in the deposition chamber can range from 10^{-8}-10^{-7} Torr. Figures 2.3 and 2.4 show the optics setup and a diagram of the UHV C2 for PLD.

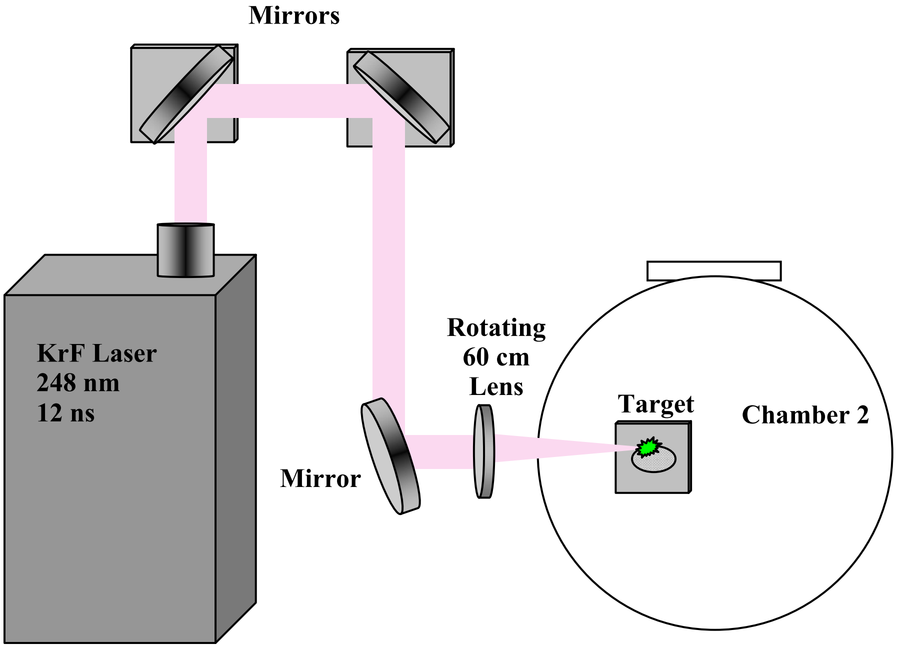

Figure 2.3: Diagram of optics setup for PLD process.

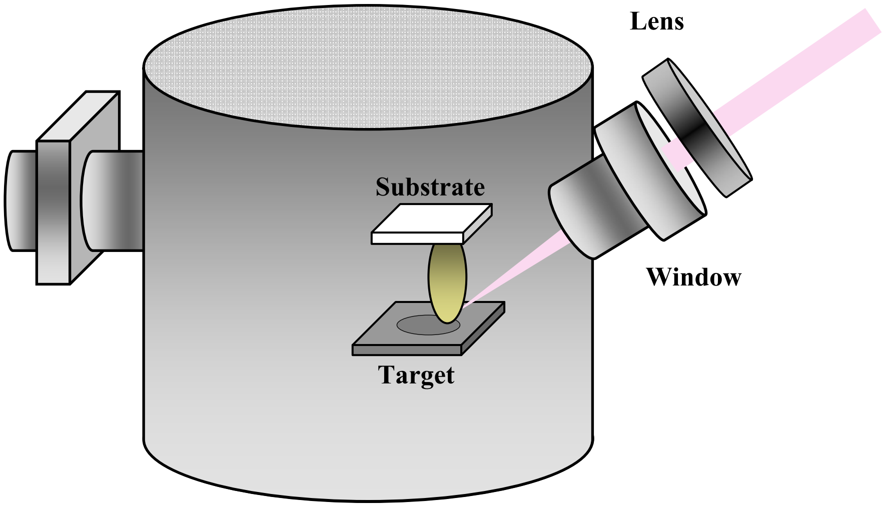

Figure 2.4: Diagram of UHV C2 used for PLD.

The KrF laser is directed to C2 by reflecting off of three mirrors on kinematic optical mounts. It is then focused by a 60 cm spherical lens mounted outside of the vacuum chamber on the window port. The laser repetition rate used in all experiments was 10 Hz and the target was a 6.35 × 6.35 × 0.7 cm solid piece of $Tb_{0.3}Dy_{0.7}Fe_{1.92}$ purchased from Etrema (Ames, IA). Interaction between the laser and target generates a plume of target material. Since the plume is very directional, the 60 cm lens was eccentrically rotated to move the focal spot on the target. The lens was rotated at 5 RPM. The resulting film was more uniform than a film made with a stationary lens. A drawback of this configuration was that the beam comes in at an angle relative to the target causing the area of the laser spot on the target to vary by a factor of 2. In addition, portions of the unfocused beam were cut off by the rotating lens. Common solutions for both problems in dedicated PLD systems are rotating targets, rotating substrates or both rotating targets and substrates.

2.4 Flat Plate Ablation

2.4.1 FPA Process Description

FPA is very similar to PLD. In both cases, a solid target is irradiated by a laser pulse and a plume of target material is ejected. In FP ablation, rather than ejecting a plume of material directly onto a substrate under vacuum, the plume is ejected into a gas at or around atmospheric pressure. The ejection of a plume into atmosphere results in several physical differences. 1) The rapid expansion of material from the target results in a shock wave that expands symmetrically into the gas. Due to finite energy in a laser pulse and expansion into an atmosphere of gas, the velocity of the shock wave decreases with increasing distance from the ablation. 2) Ionization and breakdown of the atmospheric gas can lead to lower fluence at the target and thus a lower rate of ablation. 3) Plume dynamics are altered when expansion occurs into an atmosphere. The pressure of background gas species results in rapid deceleration of ejected material which causes the dense plume of hot material and ions to collide with each other. These collisions result in nucleation, growth and condensation of nanoparticles. The particles are then accelerated from atomospheric pressures to vacuum and impacted onto substrates to make thick films. Figure 2.5 illustrates the FPA process.

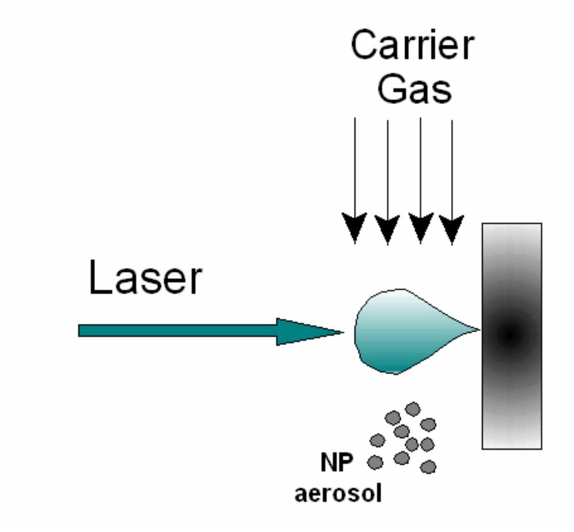

Figure 2.5: Illustration of flat plate ablation. NPs nucleate from plume in carrier gas.

2.4.2 FPA Experimental Setup

A schematic of the ablation chamber, composed of the "horn cell" and virtual impacter, used for FPA is shown in Figure 2.6. Flowing gas enters the ablation cell through the top of a flange. The gas was forced to fill the central tube and flow in a laminar stream using a diffuser plug. The diffuser plug pressurizes the gas upstream and distributes the gas to laminarize the flow downstream. The laser was focused through the two conical sections protruding from the central tube. This entire assembly is the ablation chamber. A piece of solid $Tb_{0.3}Dy_{0.7}Fe_{1.92}$ was held in place at the back of central tube where the laser spot size was 2 mm × 4 mm. The ends of the ablation chamber were sealed by rubber o-rings pressed between a circular window and a flange. The conical portions of the ablation chamber leave the gas flowing through the central tube mostly undisturbed because gas fills the cones and stagnates. The windows, made of quartz with anti-reflection coatings for 248 nm on both sides, were located away from the central tube to increase the laser spot size passing through the window, thus lowering the laser fluence on the quartz windows and minimizing damage to the windows. The conical shape of the ablation chamber was also used to reduce gas turbulence in the central tube by minimizing the volume of stagnant gas in the protruding window holders while allowing the focusing laser beam to pass through.

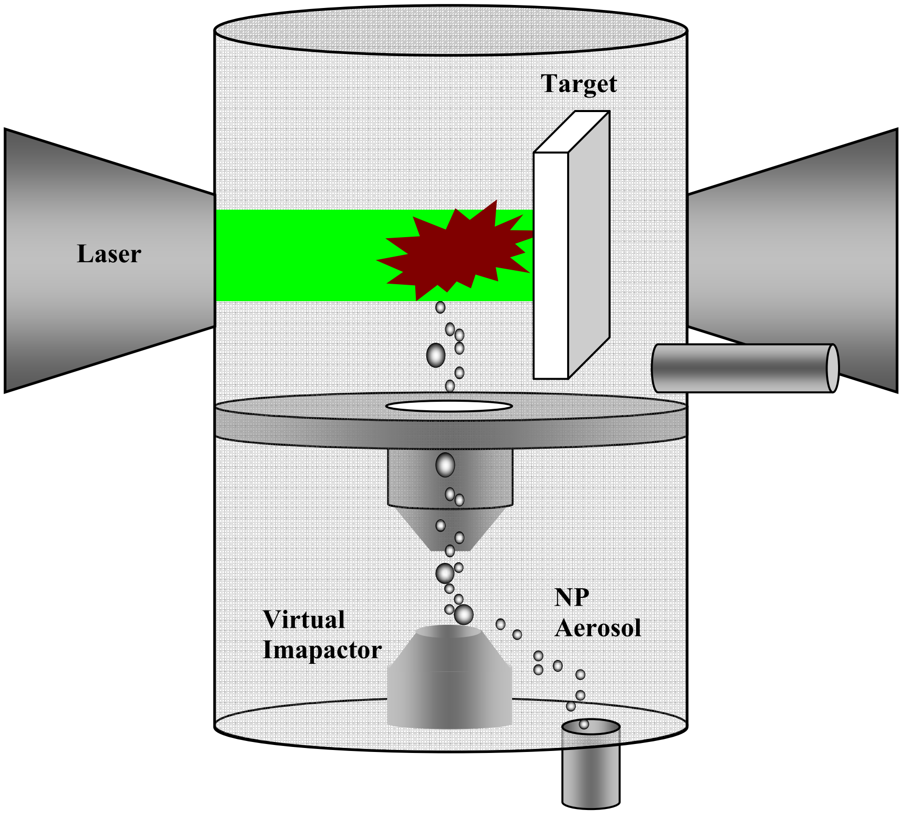

Figure 2.6: Illustration of ablation chamber and setup used for FPA.

Figure 2.7 shows the optics setup for FPA. For laser processing in the ablation cell, the laser beam is reflected off of a mirror on a kinematic mount and then focused with two cylindrical lenses. Two lenses are used to control the focus height and width independently allowing for greater freedom in spot size and shape at the target. The vertical dimension of the beam is focused with a 110 cm quartz lens and the horizontal dimension is focused with a 14 cm lens.

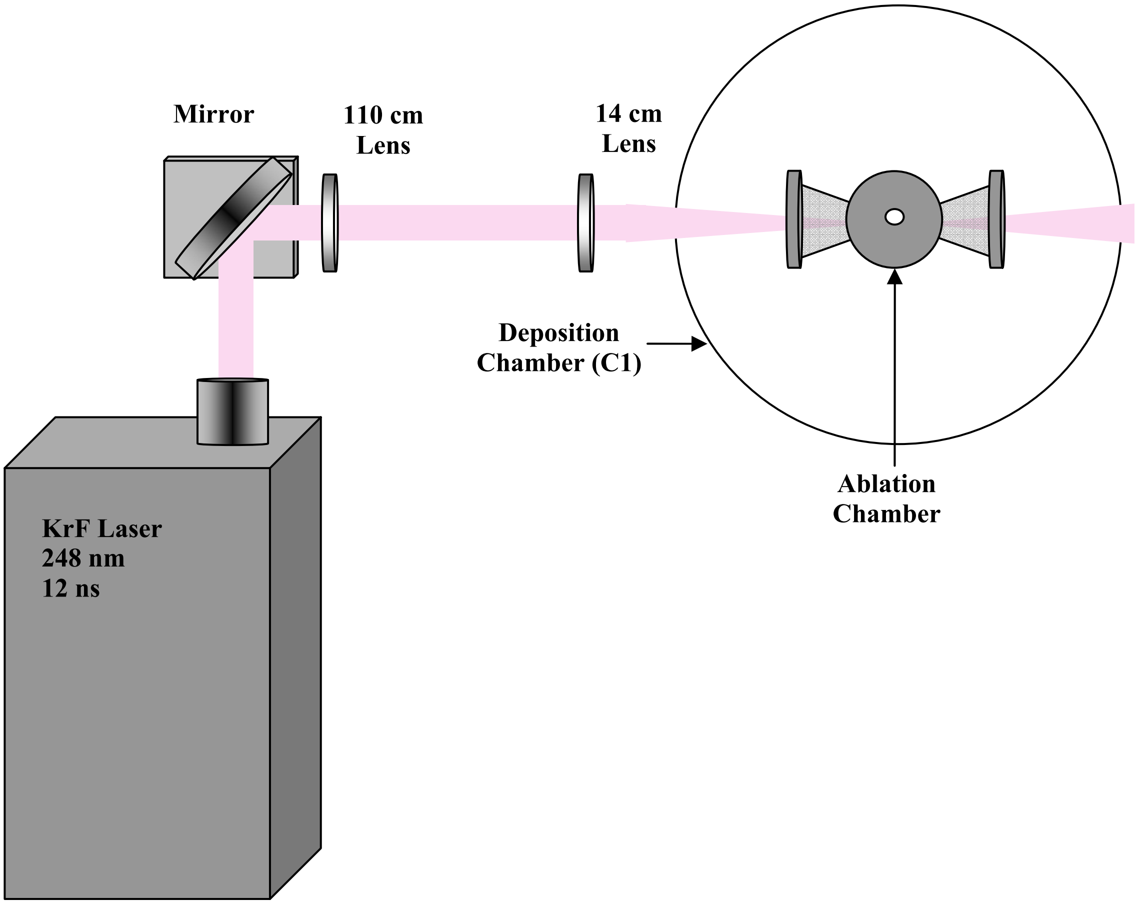

Figure 2.7: Schematic of optics setup for FPA and LAM.

In the central tube of the "horn cell", the focused beam irradiates a solid target, nanoparticles are generated and become entrained in the flowing gas. The nanparticle aerosol travels toward the virtual impactor. Although most nanoparticles generated from ablation are small (< 100 nm), fracturing of the target can lead to the inclusion of larger particles in the aerosol. The large particles are removed from the aerosol by the virtual impactor.[21] A detailed description of the virtual impactor design used here is discussed by Henneke.[22] Briefly, the virtual impactor consists of a nozzle positioned directly above a hollow cone. Nanoparticles exiting the nozzle follow the gas streamline around the opening of the cone while the larger particles (>500 nm) have too much momentum and are forced to enter the hole and are removed from the aerosol. The remaining aerosol of nanoparticles continues down into the deposition nozzle in C1.

The deposition nozzle is a 100 cm long tube that is 6.35 mm in diameter. The tube ends in a flat plate with a 250 μm opening. The nanoparticle aerosol goes from atmospheric pressure to ~ 200 mTorr inside C1. This pressure difference accelerates the particles up to 1000 m/s depending of gas type and particle size.[23] The deposition nozzle is positioned 2-4 mm from the substrate. Upon impaction with the substrate, the NPs have enough kinetic energy to bond to the substrate and other NPs. The substrate sits on an x-y motor-controlled stage which allows patterning of thick films of nanoparticles. Spirals, serpentines and films have been directly written using this system.

2.5 Laser Ablation of Microparticles

2.5.1 LAM Process Description

LAM was developed at the University of Texas at Austin and has been used to generate nanoparticles of many different materials (AlN, CdSe, W, Si, PZT, Au, Ag, Nd glass, Cu, $Tb_{0.3}Dy_{0.7}Fe_{1.92}$) and devices (inductors, hermetic seals, cantilevers). LAM is similar in concept to both PLD and FPA.[24] Instead of solid targets, LAM uses microparticles entrained in an aerosol as feedstock.

Physically, the ablation process in LAM is fundamentally different from the solid target ablations. In this process, each microparticle is irradiated with a pulse of the KrF laser. A schematic of the breakdown process is shown in Figure 2.8. Ideally, the microparticle absorbs all of the energy within the skin depth (~ 10 nm for $Tb_{0.3}Dy_{0.7}Fe_{1.92}$) of the particle. The particle rapidly heats up until the breakdown threshold is reached. Visual observation and simulation of the breakdown suggest that a shock wave forms at the front edge and expands radially. The shock wave compresses and heats the microparticle above its critical point.[25] Behind the shock wave, there is a low pressure region where the vapor nucleates and condenses to form nanoparticles. Size distribution studies by Nichols et al. have shown a bimodal distribution of nanoparticles.[26] The smaller size particles were attributed to the formation of particles in the low pressure region behind the shock wave. The larger size particles were attributed to evaporation that occurred before the formation of a shock wave. Particle size can be altered by adjusting processing parameters such as background pressure and gas type.[27] It has been shown that increasing the background pressure results in larger nanoparticles. Also, ablation in a background of argon gas results in larger particles than in nitrogen which in turn results in larger particles than those made in helium.

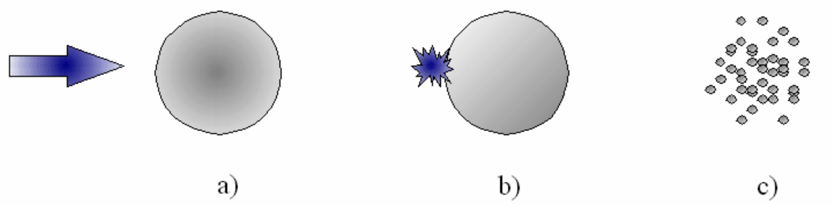

Figure 2.8: Illustration of LAM process. a) Laser is focused on microparticle. b) Laser ionizes front surface of microparticle. c) NPs nucleate in carrier gas.

The LAM process has several advantages over ablation from a solid target. 1) The finite size of the microparticle combined with the assistance of the shock wave lowers the fluence required to vaporize the material. 2) There is very little vapor plume expansion from the breakdown process. The confinement of the plume leads to a more consistent nanoparticle size than particles made by FPA. 3) LAM is a more efficient process for generating nanoparticles because a large fraction of the microparticles is converted into nanoparticles. 4) Ablation of microparticles instead of a solid target prevents alteration of composition of the target and nanoparticles that may occur over time due to preferential evaporation of one species present in the target.

2.5.2 LAM Experimental Setup

Figure 2.9 shows the ablation chamber setup for LAM. The setup for LAM is similar to the setup used in FPA. See Figure 2.7 for an illustration of the optics setup. Flowing gas and microparticles enter the ablation cell through the top of a flange. The gas is forced to fill the central tube and flow in a laminar stream by a diffuser plug. This flow will be referred to as the outer flow. In the LAM process, there is an additional tube, the ablation tube, which goes down through the center of the central tube where the aerosol of microparticles enters. This will be referred to as the center flow. The linear velocity of the center flow was adjusted to assure each microparticle was irradiated. With the area of the ablation tube at 4.6 mm^2, the spot size of the focused beam at 2 mm x 4 mm and a maximum laser repetition rate of 200 hz, the center flow was set at 158 sccm which corresponds to a linear velocity of 13.3 mm/s. The linear velocity of the outer flow was adjusted to match that of the inner flow in order to retain laminar flow and constrain the aerosol of microparticles.

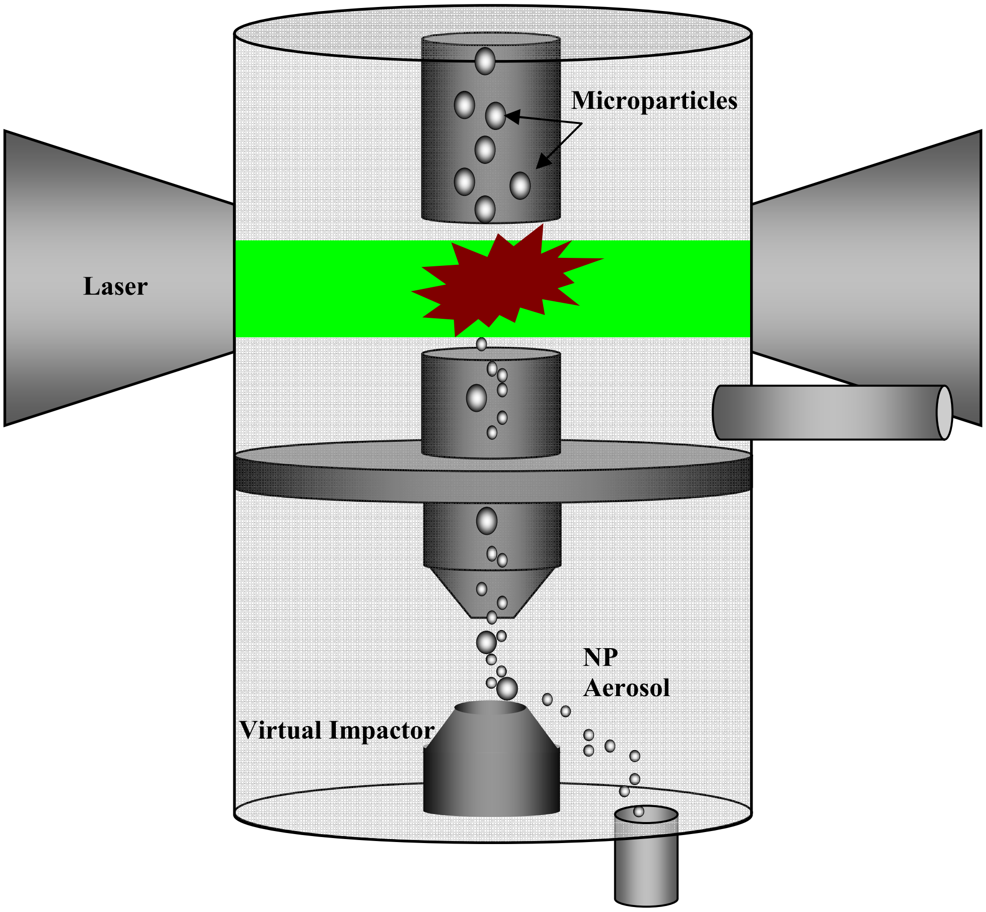

Figure 2.9: Illustration of ablation chamber for LAM process.

In the central tube of the "horn cell", the focused laser irradiates the aerosol of microparticles where the nanoparticles are generated and are constrained by the outer flow of gas. In LAM, a skimmer is inserted to separate the nanoparticle aerosol from the excess gas. The skimmer is a tube that is positioned in the center of the flow right below the ablation zone. The nanoparticle aerosol, still constrained by the outer flow, goes into the tube and the outer flow is directed out of the ablation chamber into a fume hood. The skimmer tube leads to the nozzle of the virtual impactor where large particles are separated from the aerosol stream. The nanoparticle stream is then directed through the deposition nozzle onto a substrate in C1.

Although gas flow rates are adjusted so that each microparticle is ablated, a virtual impactor is used because there are circumstances where microparticles could travel through the ablation region without being ablated. 1) Microparticles could be out of the ablation region and never be illuminated. This could occur if the aerosol stream is slightly misaligned with the focused laser beam. 2) In an aerosol, there is a possibility that microparticles could be directly positioned behind another microparticle and thus the particle is shadowed and never illuminated or only partially illuminated. This scenario could occur anytime there is a high density of microparticles in the aerosol. Another possibility for shadowing is the agglomeration of microparticles and the feeding of agglomerates.

2.6 Procedures to Minimize Contamination

2.6.1 Introduction

The intermetallic of Tb, Dy and a transition metal (Fe) compose the magnetostrictive material used in this study. All of these elements are highly reactive. Figures 2.10 and 2.11 show the effect of contamination on bulk $Tb_{0.3}Dy_{0.7}Fe_{1.92}$. Oxide and nitride compounds of all three elements cause degradation in the magnetization and magnetostriction when compared to the pure elements or the intermetallic and thus are to be avoided. Oxidation and nitridation is even more rapid at the high temperatures that occur during laser processing and thus are particularly important for this work. Since oxygen, nitrogen and water are abundant in the atmosphere, they are difficult if not impossible to completely eliminate. In the three laser processing techniques investigated, there are many possible sources of gas contamination. The following section outlines the procedures taken to minimize the contamination of the starting material and gas-phase reactions that could occur during the film processing.

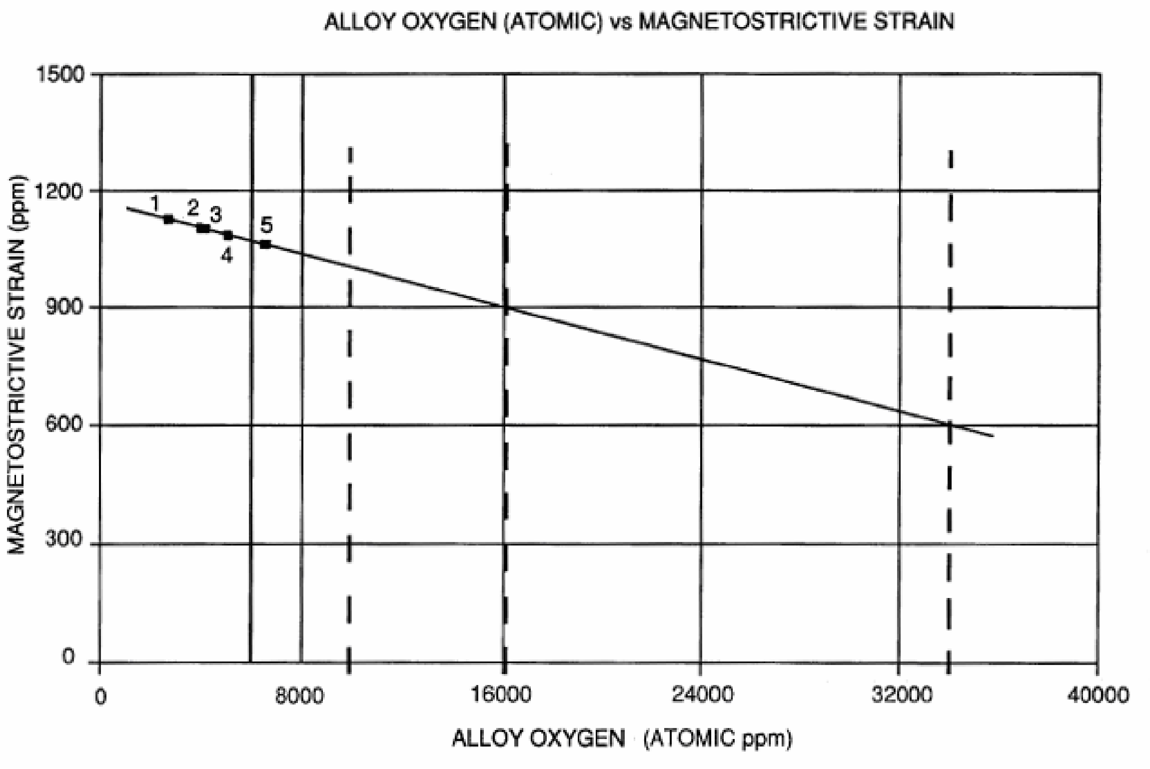

Figure 2.10: Reduction in magnetostriction with increasing oxygen content for bulk $Tb_{0.3}Dy_{0.7}Fe_{1.92}$.[28]

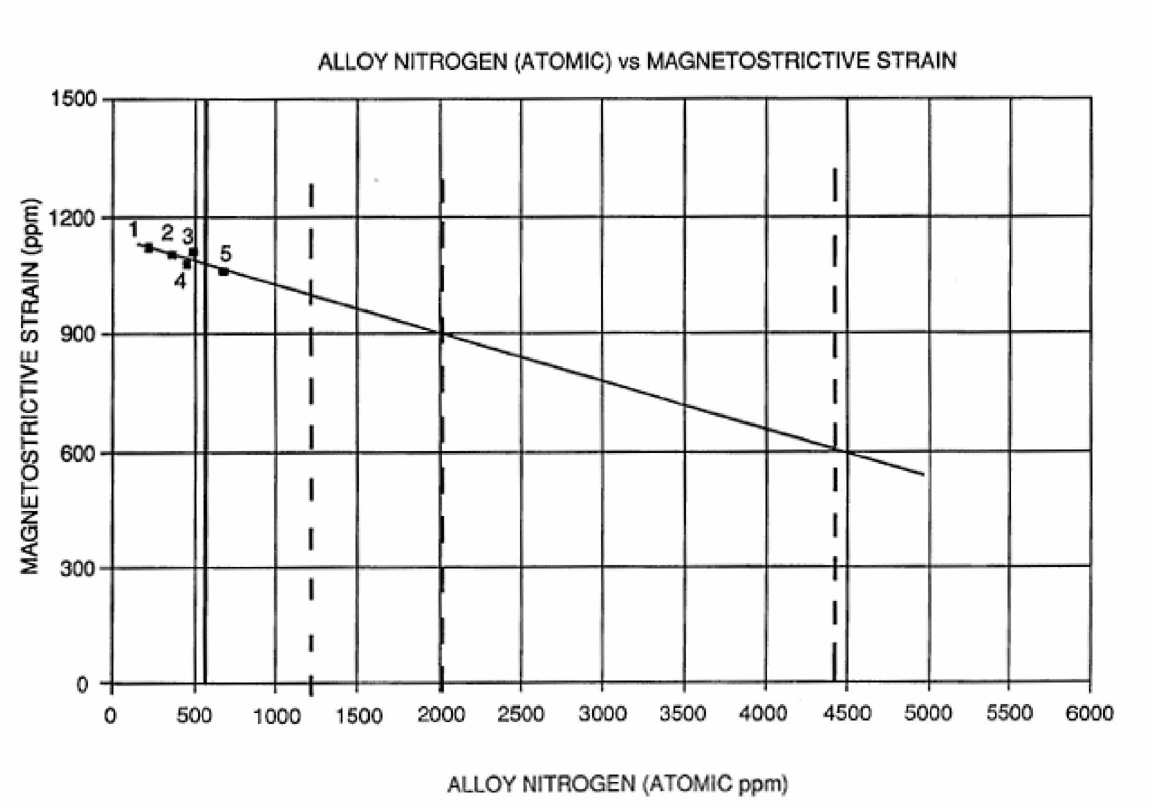

Figure 2.11: Reduction in magnetostriction with increasing nitrogen content for bulk $Tb_{0.3}Dy_{0.7}Fe_{1.92}$.[28]

2.6.2 Gas Handling System

In the laser processing methods of FPA and LAM, the nucleation of nanoparticles occurs from a plasma in one atmosphere of flowing gas. This is a particularly critical place to avoid contamination because in this region the temperature can reach several thousand Kelvin and the surface area of the $Tb_{0.3}Dy_{0.7}Fe_{1.92}$ is at its highest. To avoid reactions, the purity of the carrier gas must be maintained throughout the delivery system. This is accomplished by an all metal gas delivery system (Figure 2.12). The tubing is either copper or stainless steel with face metal seals at all points of connection. The system is attached to a dry pump and bellows sealed valves with stainless steel or ceramic seats used throughout to close off unused sections. The gas system is checked for leaks, purged multiple times and baked using a heat gun and heating tape prior to conducting experiments.

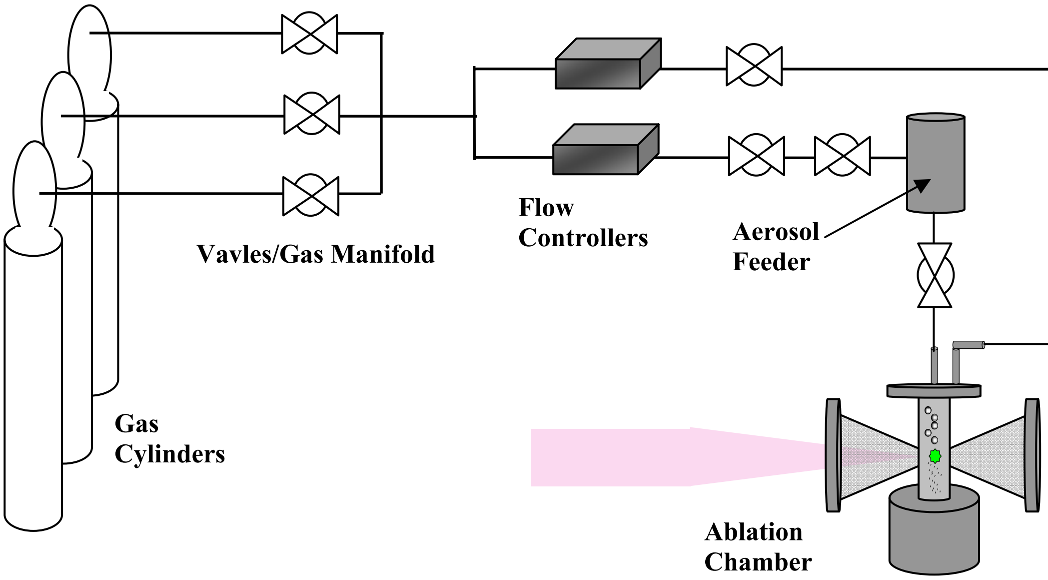

Figure 2.12: Illustration of gas handling system for FPA and LAM.

2.6.3 Ablation Chamber

The ablation chamber and downstream components are intricate and much more complicated than the gas handling system. Due to complex components, like the "horn cell" that required a quartz window-to-metal seal, there are several rubber (Viton) o-ring seals in this section. These parts can be closed off from the rest of the gas handling system. The entire ablation cell is attached to a separate mechanical pump and also connected to C1. Prior to all experiments, these components are baked with heating tape and purged multiple times with the mechanical pump. These parts are then pumped down to 2×10^{-7} Torr through the turbo pump in C1.

2.6.4 Preparation of Target Material

For the FPA and PLD experiments, solid pieces of $Tb_{0.3}Dy_{0.7}Fe_{1.92}$ are used to produce nanostructured and dense films. A potential source of contamination in the deposited films is the surface of the solid target. To minimize the introduction of oxygen and nitrogen present on the target surface into the films, after cutting the pieces of $Tb_{0.3}Dy_{0.7}Fe_{1.92}$ to the desired size, each piece was cleaned in phosphoric acid (50/50) to remove organics. The pieces are rinsed and sonicated in methanol and then ethanol before being placed inside the chambers for ablation.

For FPA, the ablation chamber is purged > 5 times and then baked at 200° C under technical vacuum (dry pump). It is then pumped down to 2×10^{-7} Torr by the turbo pump. For PLD, the chamber and target is baked at 200° C under vacuum for 48 hours prior to deposition. The pressure of the vacuum chambers (C1 and C2) are typically less than 5×10^{-9} Torr after baking. Even after taking these steps, there are absorbed gases on the surface of the target. We can see this by monitoring the partial pressure of ionized gas species during ablation using a residual gas analyzer (RGA). This is especially prevalent during the first few minutes of ablation. RGA details are provided later in this chapter.

For the LAM process, the target material is microparticles entrained in an aerosol. Since microparticles have higher surface area than the solid targets, it is critical to use more extensive measures to minimize the amount of contamination. Thus, powder preparation was performed inside a glove box with a 99.9995% purity argon gas atmosphere. In early experiments, microparticles (0-300 μm) of $Tb_{0.3}Dy_{0.7}Fe_{1.92}$ were purchased and ball milled in a polyethylene bottle with tungsten carbide milling media for 24 hours (Figure 2.13). Although this preparation technique results in a more ideal target material (nearly spherical particles with a narrow size distribution), it also has many sources of contamination. Water and oxygen can be on the inside of the bottle and the surface of milling media. In addition, the conditions in which the microparticles from Etrema are collected are unknown and may not be consistent. To minimize the sources of contamination, another power preparation technique was employed. The target microparticles in all of the LAM data presented are produced from pieces of solid $Tb_{0.3}Dy_{0.7}Fe_{1.92}$ that are cleaned using the method presented above for the PLD target. The solid is then placed inside the glove box. Since $Tb_{0.3}Dy_{0.7}Fe_{1.92}$ is a brittle intermetallic, it can be reduced to microparticles easily using a mortar and pestle. The resulting microparticles are composed of irregularly shaped particles between 0.2 – 45 μm (Figure 2.14).

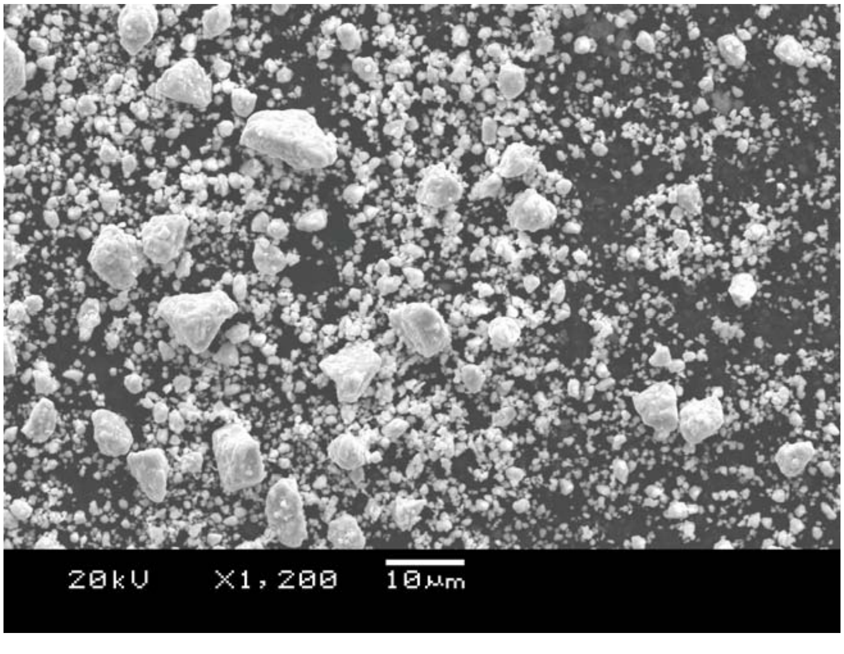

Figure 2.13: Microparticles of $Tb_{0.3}Dy_{0.7}Fe_{1.92}$ after ball milling 24 hrs with tungsten carbide milling media.

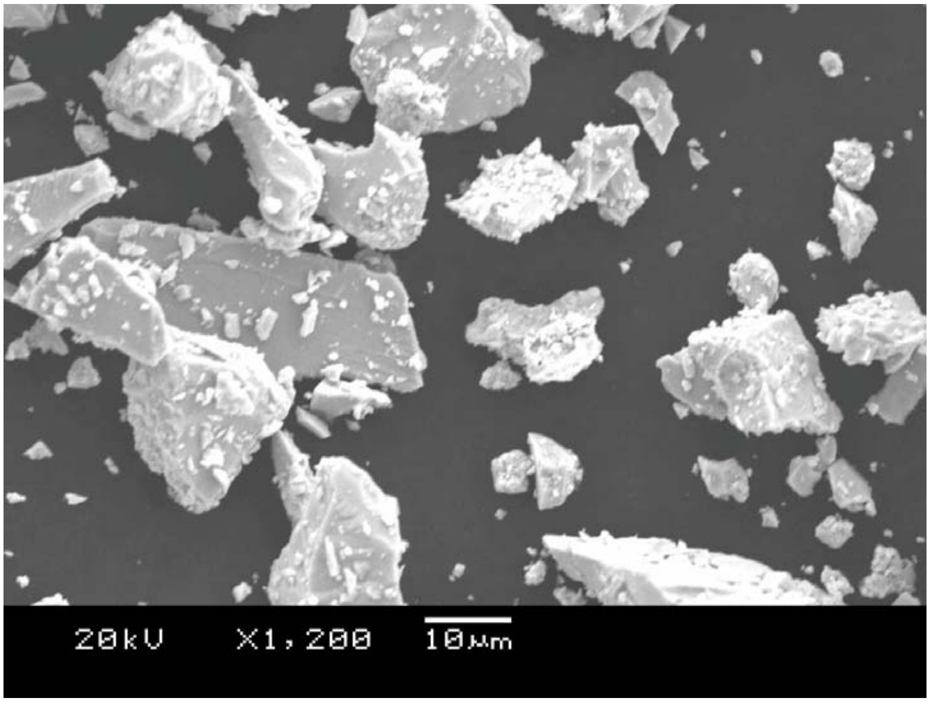

Figure 2.14: Microparticles of $Tb_{0.3}Dy_{0.7}Fe_{1.92}$ made by mortar and pestle.

2.6.5 Aerosol Feeder and Transporter

After grinding the $Tb_{0.3}Dy_{0.7}Fe_{1.92}$ inside the glove box, the microparticles must be transported and connected to the gas system without exposing the particles to air. In addition, a high density aerosol (10^4 - 10^6 particles/cm^3) is required at low gas rates. The design and construction of a combination transporter / aerosol generator was required to overcome these restrictions. The final design (Figure 2.15) used in all LAM experiments was high vacuum compatible and constructed with mostly stainless steel (SS). The aerosol generating part of the device is made of a SS cylinder with a 250 µm press fit aluminum nozzle. A reservoir of powder is placed in the volume above of the nozzle. With a nominal flow rate at the inlet of 158 sccm, most microparticles would not have enough drag force to be entrained in the gas. This nozzle aerosolizes the particles by increasing the linear velocity, and thus the drag force, at the outlet of the nozzle.

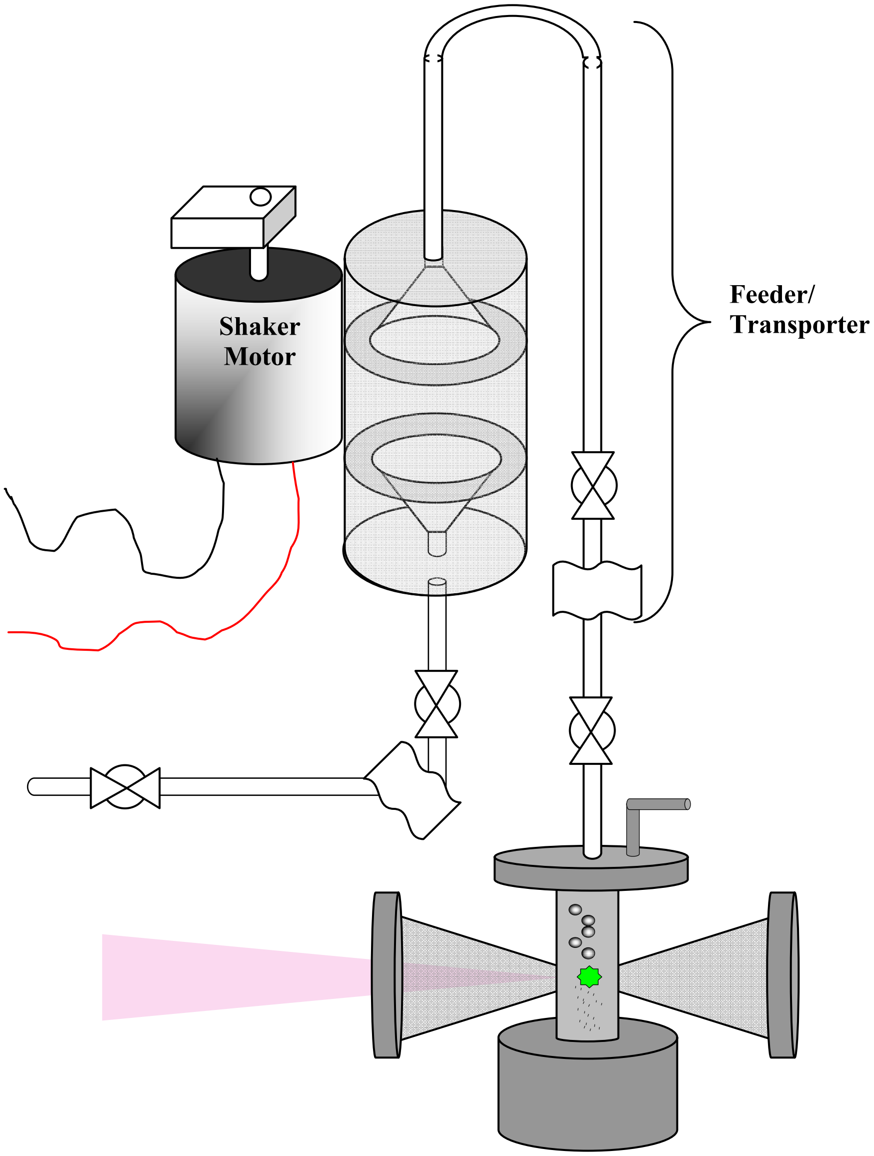

Figure 2.15: Illustration of transporter / aerosol feeder assembly. Breaks show where the feeder/transporter can removed from the rest of the system.

The aerosol feeder is connected to the rest of the transporter device with metal seals. A bend was placed below the aerosol feeder (inlet) to prevent any microparticles that fall through the nozzle from entering the gas handling system. Microparticles in the gas handling system can become lodged in the seat of valves causing it to leak. A bend was above the aerosol feeder (outlet) to prevent larger particles and big agglomerates from entering the ablation region. Larger particles and agglomerates are detrimental because they are too large to be completely ablated at the fluence used and clog the supersonic jet deposition nozzle. In addition, these types of particles absorb a large cross-section of the laser energy which leaves particles in the aerosol directly behind them "shadowed" and unablated. The last design feature was isolation of the transporter / aerosol feeder on the inlet and the outlet by two bellows-sealed valves.

2.6.6 Substrate Preparation

Silicon wafers (125 μm) and alumina plates (127 μm, Coors Tek AD996) are used as substrates for the experiments. The cleaning procedure is identical in both cases. After dicing into cantilevers, they are rinsed in acetone to remove the photoresist on the silicon and the adhesive used for dicing on the alumina. The substrates are cleaned with phosphoric acid (50/50) and then rinsed in methanol and ethanol. They are weighed and then placed inside C1 where the entire chamber is baked at 200°C for 2 hours to remove water introduced through the exchange chamber of the vacuum system and water on the surface of the substrate holder.

2.7 Monitoring Ablation and Vacuum Conditions

2.7.1 Introduction

With all of the precautions taken to assure the purity of the gas and target, it was important to observe the effects of these precautions on the resulting films. Qualitative analyses using SEM EDS, TEM EDS and XRD were shown to be ineffective because these tools were not available inside the deposition chambers (C1, C2) so the films have to be removed from the deposition chambers before these analyses could be preformed. Since there is no way of moving the deposited films from the chambers to the SEM, TEM or XRD in an inert atmosphere or vacuum, exposure of the films during transport to the oxygen in the atmosphere resulted in oxidation of the films. EDS analyses on all films, made with and without taking the precautions discussed earlier in this chapter showed similar oxygen concentrations further complicating quantification of the oxygen concentration.

2.7.2 Optical Emission Spectroscopy

It was critical to find an alternative technique for measuring the contamination in the system. As discussed earlier, a plasma is formed during the ablation process. As the excited atoms return to a lower energy state, they emit photons that are characteristic of the energy transition (ΔE),

$$\Delta E = h\upsilon , \tag{2.2}$$

where ν is the frequency of radiation and h is Plank's constant.[29] Due to electronic differences in elements and molecules, each has a specific characteristic emission frequency. Thus, optical emission spectroscopy (OES) can be used to monitor the ablation process. Unfortunately, the observed spectroscopic emission does not distinguish where the oxygen is coming from and therefore the major source of contamination cannot be distinguished using OES. However, gases, gas lines, components, and target must all be free of oxygen and water for any successful film deposition. OES is an effective means to determine if the precautions have successfully removed the oxygen and moisture.

A StellerNet EPP2000 NIR2 spectrometer with an integrated holographic grating (1200/lines nm) and a 2048 pixel (14 μm × 200 μm) CCD detector is used. The CCD is capable of detecting spectra from a fiber in the wavelength range of 600-1100 nm. A 400 μm diameter low OH, silica-clad, silica core fiber was used to collect the light emitted during ablation. A collimator (allowing wavelengths from 190-2000 nm) is attached to the fiber to increase the signal. The fiber and collimator are placed in an adjustable holder with a 77 mm lens to increase the signal-to-noise. This assembly was positioned directly in front of the ablation view port of the ablation cell. Since there are no internal filters in the spectrometer, second order emission could be captured. To remedy this, a Corning 2-63 cutoff filter was inserted between the port and lens to block emission of wavelengths less than 590 nm. A schematic of the setup is shown in Figure 2.16.

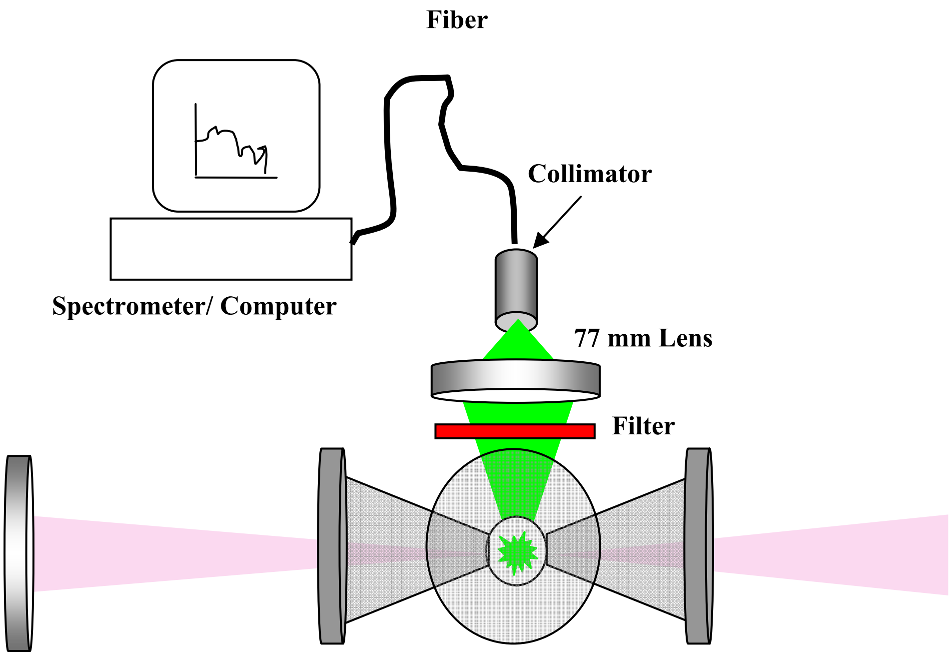

Figure 2.16: Schematic of experimental setup of OES for ablation chamber.

An oxygen lamp spectrum was measured to calibrate the spectrometer. The spectrum is shown in Figure 2.17. As expected the most intense peaks in the spectrometer range for oxygen are at 777 nm followed by 845 nm. Since the amount of signal in spectra from ablation is dependent on optical alignment and density of particles in the aerosol, it is difficult to get a quantitative comparison of oxygen contamination from counts of the oxygen peak alone. Instead, the most intense peaks of oxygen will be compared to the most intense peaks of iron to determine the relative degree of oxygen contamination.

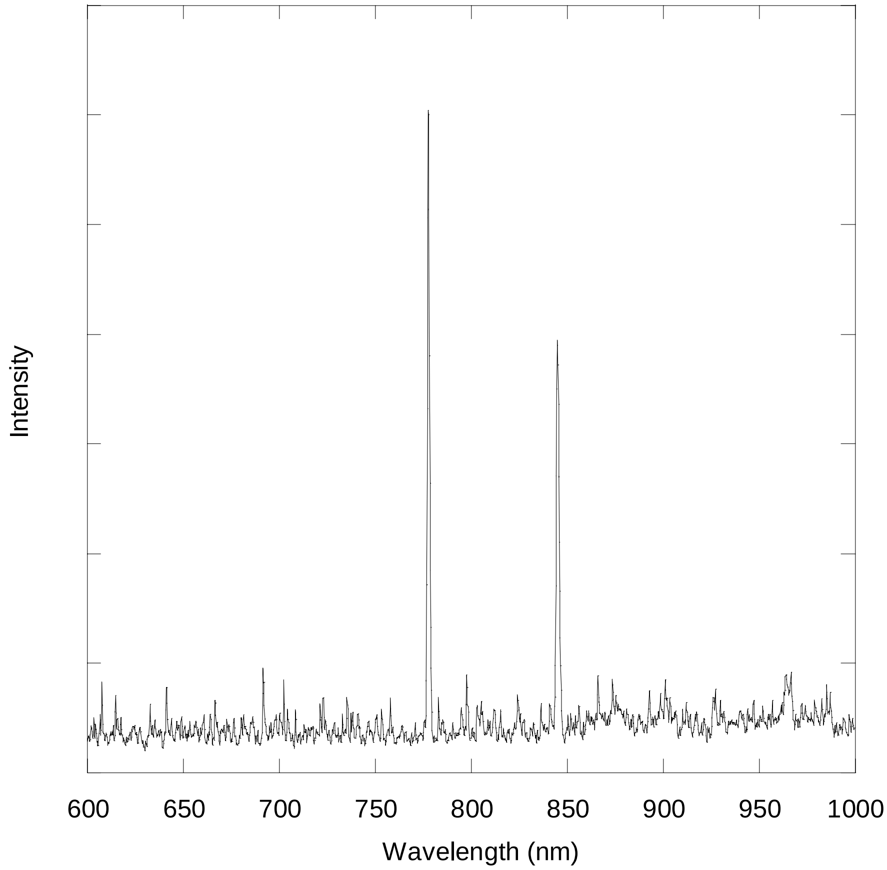

Figure 2.17: OES of oxygen lamp.

2.7.3 Residual Gas Analyzer

In addition to OES, the environment in the vacuum chambers is monitored by a residual gas analyzer (RGA). A RGA is a mass spectometer that analyzes gas phase ions by their mass-to-charge ratio. The ion signal at a given field correlates to a mass-to-charge ratio. A mass spectrum is obtaining by measuring the ion signal intensity throughout a scanned electric field. Because the response of the signal from a commercial device is nonlinear, the calibration for each gas phase is critical for accurate quantification of partial pressures. Here no calibrations were made and the RGA is used as a qualitative measure of residual gas species in the vacuum chamber.[30]

.

Chapter 3

Film Analysis

After films were deposited by PLD, FPA and LAM, their microstructure and magnetic properties were characterized. This chapter describes the methods and tools used to analyze the particles and films.

3.1 Mass Analysis

In order to characterize the magnetic susceptibility of a deposited sample, the mass of deposited $Tb_{0.3}Dy_{0.7}Fe_{1.92}$ must be determined. For PLD, deposition took place at low vacuum pressures and dense films were deposited. The mass was calculated from the volume of deposited material with the assumption that the films had the same density as bulk $Tb_{0.3}Dy_{0.7}Fe_{1.92}$. The volume was measured for the area of the substrate and the thickness of the film using a mechanical profilometer.

As deposited nanostructured films made by FPA and LAM were not quite as dense. Films of silver nanoparticles jet deposited under similar conditions to those used in this study have been shown to have densities ranging from 56-75% of bulk silver.[31] These measurements were calculated based on the resistivity of deposited films. The film density of $Tb_{0.3}Dy_{0.7}Fe_{1.92}$ could not be determined using the same techniques because accurate determination of film density requires measurement of electrical conductivity which was not performed as part of this study. As a result, the mass of the films made by FPA and LAM were determined directly from the weight. Substrates were first cleaned and then separated into labeled glass vials. They were then weighed in a thermal gravimetric analyzer (TGA, Perkin-Elmer TGA7). After deposition, the substrate and deposited film were weighed together and the mass of the film was determined by subtraction. A TGA is typically used to determine weight loss of materials as a function of time or temperature. In our case, the TGA was used to determine the mass of the samples because it is the most accurate balance available. Although the precision of the balance is 1.5×10^{-3} mg, actual measurements of an alumina substrate multiple times over a period of two months showed the accuracy was 1.5×10^{-2} mg. The alumina cantilevers used in the experiments weighed ~ 10 mg. Films deposited by FPA and LAM weighed between 0.20 and 0.71 mg.

3.2 Profilometry

A Dektak3 stylus profilometer was used to determine the profile and thickness of deposited films. A diagram of the cantilever, substrate holder and scan position is shown in figure 3.1. For PLD, cantilevers (substrates) were attached to a larger and thicker piece of silicon (backing plate). After PLD deposition, the cantilevers were removed from the substrate holder. During deposition, the cantilever acted as a mask and left a step between the bare silicon under the cantilever and the deposited film on the substrate holder. Since this step is the exact same height of the film on the cantilever, it was used to measure film thickness. The resulting film coverage of $Tb_{0.3}Dy_{0.7}Fe_{1.92}$ on the substrate was relatively uniform. The measured difference in film thickness from all scans on a single sample was typically less than 20 nm.

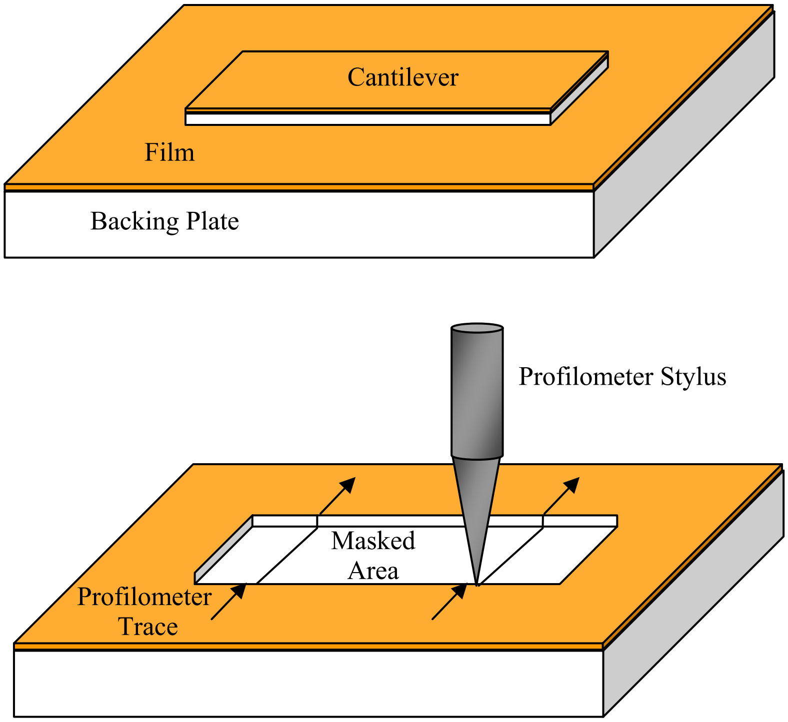

Figure 3.1: Illustration of substrate assembly depositing films using for PLD and for measuring film thickness.

The profile and thickness of nanostructured films made by jet deposition were also determined using the profilometer. The substrate assembly for the jet deposited films was similar to the one used in PLD. Since annealing experiments were performed on some of these samples, alumina was used as a substrate for these films instead of silicon to lower the thermal expansion mismatch between $Tb_{0.3}Dy_{0.7}Fe_{1.92}$ and the substrate. The motors in C1 were programmed so that the entire surface of the substrate was covered with some overspray in order to maximize film thickness and uniformity. Due to the small amount of overspray, thick films, and low film densities of <75%, the material deposited on the substrate holder was relatively weak. The cantilevers could not be removed without destroying some of film on the substrate holder. As a result, the thickness of the jet deposited films could not be consistently measured with the same method used for PLD films. Instead films were measured diagonally on the cantilever from a masked area. Figure 3.2 illustrates a film and profilometer stylus path for films made on alumina.

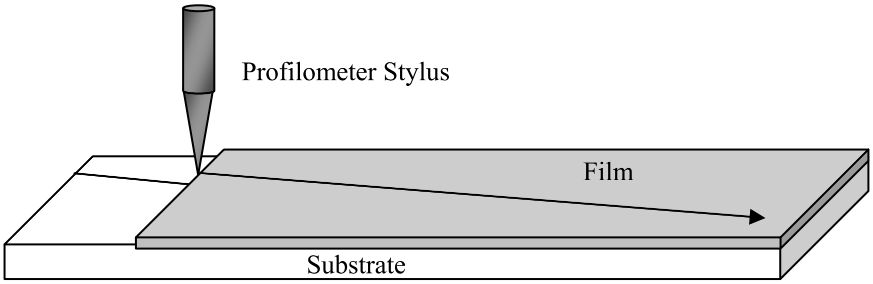

Figure 3.2: Profilometry scan path for films made by FPA and LAM

3.3 Magnetic Properties Measurements

In Chapter 1, the importance of magnetization and its relationship to magnetostriction was discussed. The detector used to measure the magnetization of a deposited film was a superconducting quantum interference device (SQUID). There is no device that is more accurate at measuring magnetic flux than a SQUID.[32] SQUIDs operate by combining flux quantization (flux is quantized in a closed superconducting loop) and Josephson tunneling (the movement of electrons between two superconductors, across an insulating layer, without an applied potential). The equipment used here was a dc SQUID made by Quantum Devices.

SQUID samples were prepared by first placing a deposited sample inside of a gelatin capsule. The capsule was packed with cotton to lower the sample noise by preventing it from moving. A hole was made at both ends of the capsule so that the air within the capsule could be purged. The capsule was then inserted into a plastic straw. The plastic straw was then placed in the quartz SQUID holder. After purging, the sample was slowly lowered into the detector. The capsule, cotton, straw and quartz holder have a very low signal compared to the $Tb_{0.3}Dy_{0.7}Fe_{1.92}$ and their contribution is small. However, because of the large relative mass of the silicon and alumina substrate, the signal from the capsule, cotton and substrates was in some cases substantial. The silicon cantilevers and alumina substrates both showed a diamagnetic response. In all SQUID experimental results presented, the diamagnetic substrate response was subtracted from the film by measuring the signal of a bare substrate then subtracting it from the signal of a deposited sample (substrate + film). In addition, although the SQUID is cooled by helium and usually kept at 35 K, all data was taken with the sample chamber at 300 K.

3.4 Magnetostriction

3.4.1 Cantilever Deflection

There are many ways to measure the magnetostriction of a material. Direct methods of measurement include strain gauges, capacitance, inductance, etc. There are also indirect methods to determine magnetostriction through transverse susceptibility, small angle magnetization rotation, and stress dependent magnetization.[33] One of the simplest methods of determining magnetostriction is measuring the tip displacement of a cantilever by reflecting a laser off one end. An illustration of a cantilever tip deflection setup is shown in Figure 3.3.

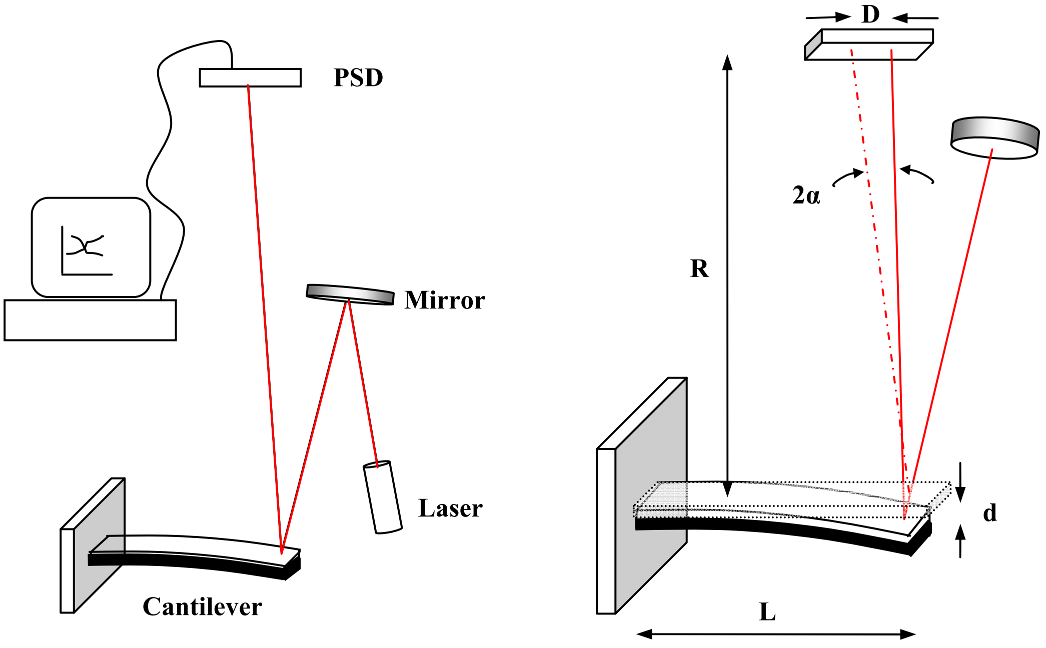

Figure 3.3: Illustration of cantilever setup for measuring tip deflection.

When the applied field $H_{\parallel}$ is parallel to the length of the cantilever, the measured magnetostriction is $\lambda_{\parallel}$. The tip displacement (d) is related to the displacement of the beam (D) by

$$\tan(2\alpha) = \frac{D}{R} \tag{3.1}$$

and

$$\tan\alpha = \frac{d}{L}, \tag{3.2}$$

where R is the distance from the cantilever to detector and L is the length of the cantilever. If α is small, then $\tan\alpha \approx \alpha$. Combining equations 3.1 and 3.2,

$$d = \frac{LD}{2R}. \tag{3.3}$$

In the setup used for all deflection measurements, R=1 m. The light source was a diode laser. D was determined using voltage output readings from a position sensitive diode (PSD).

The cantilever tip deflection (d) is related to magnetostriction (λ) by[34]

$$d = 3\lambda L^2 \frac{E_f h_f (1+\upsilon_s)}{E_s h_s^{\,2} (1+\upsilon_f)}, \tag{3.4}$$

where E is Youngs modulus, h is the thickness and ν is Poisson's ratio. The subscript s represents the substrate and f represents the film. If a sample is isotropic in the demagnetized state, then the magnetostriction ($\lambda_{\parallel}$) in a field parallel to the axis of the cantilever is equal to the saturation magnetostriction (λ_s). The observed magnetostriction $\lambda_{\perp}$ in the field perpendicular to the axis of the substrate is

$$\lambda_{\perp} = -\frac{\lambda_s}{2}. \tag{3.5}$$

However, even in the demagnetized state all ferromagnetic materials exhibit anisotropy and experimentally,

$$1 < -\frac{\lambda_{\parallel}}{2\lambda_{\perp}}. \tag{3.6}$$

Thus, it is more accurate to determine λ_s by measuring the difference between $\lambda_{\parallel}$ and $\lambda_{\perp}$ where[34]

$$\lambda_s = \frac{2}{3}(\lambda_{\parallel} - \lambda_{\perp}) = -\frac{2}{9}\frac{\mathrm{d}_{\parallel} - \mathrm{d}_{\perp}}{L^2}\frac{E_s h_s^{\,2}(1+\upsilon_f)}{E_f h_f(1+\upsilon_s)}. \tag{3.7}$$

This derivation is made with five assumptions. 1) The substrate is not magnetostrictive. 2) The cantilever length is large compared to the width. 3) The cantilever length is much larger than the thickness. 4) The film thickness is much less than the cantilever thickness. 5) The film covers the entire substrate uniformly. Our samples conform to almost all of these criteria. The 10 mm long substrates were made of alumina and silicon with thicknesses of 127 μm and 125 μm respectively and were 2-4 mm wide. Additionally, the $Tb_{0.3}Dy_{0.7}Fe_{1.92}$ film covered the entire substrate and were <20 μm thick. Films made by PLD were uniform. However films deposited by jet deposition were very non-uniform and had a high surface roughs. For these reason, magnetostriction in the thick films is only a qualitative measurement.

3.4.2 Magnet Mangle

To measure the cantilever deflection ($d_{\parallel}$ and $d_{\perp}$) in a magnetic field, an optical setup (Figure 3.4) and variable magnetic source are required. The optical setup was described in the previous section. A common magnetic field source is an electromagnet like the one used by our collaborators in Lille, France on a similar set up. A major drawback of their system was the large inductance of the electromagnet. This increased the transient time between magnetic fields and a full hysteresis loop would take 40 minutes. At the same time, the electromagnet emitted varying amounts of heat around the sample, thus causing tip deflection due to thermal expansion mismatch between the film and substrate. In addition, air currents, sunlight and room lights also add to the thermal drift problem.

To minimize the thermal drift problem, a deflection apparatus was designed and built by Daniel O'Brien and full details can be found in his dissertation.[35] Briefly, the idea of using vector addition of separate magnets to produce a larger field originated from Halbach.[36] A diagram a Halbach cylinder and an approximation of a Halbach cylinder is shown in Figure 3.4.

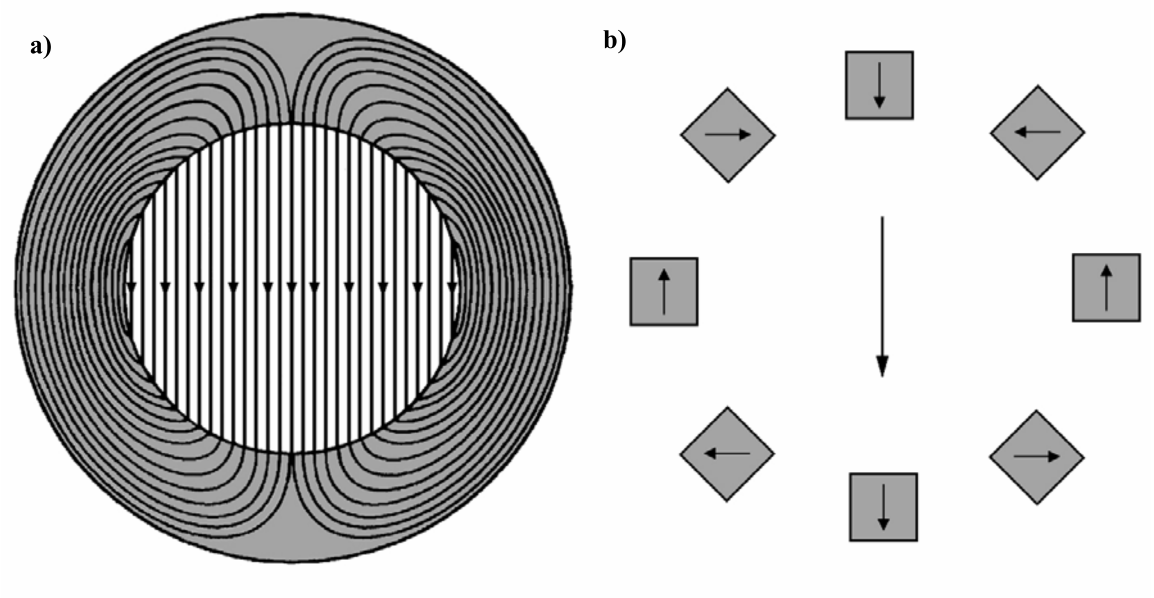

Figure 3.4: Illustration of a) Halbach cylinder and b) approximation of Halbach cylinder using rectangular magnets.[35]

In the Halbach cylinder, the cylinder is a monolithic piece of magnetic material. The field inside of the cylinder is very uniform and the flux is in one direction. A variable field device can be made by placing two cylinders with the same field together concentrically and rotating one of the cylinders. This is an approximation of a Halbach cylinder made of discrete magnets. The field inside of this approximation of a cylinder is not as uniform and depends on the number of discrete magnets used (more magnets = increased uniformity). However, an increase in the number of magnets requires a larger cylinder with a concomitant reduction in field. The magnetic field in this array is varied by rotating each magnet in a coordinated manner. Figure 3.5 shows the arrangement of discrete magnets, rotation motion and resulting field of an approximated Halbach cylinder.

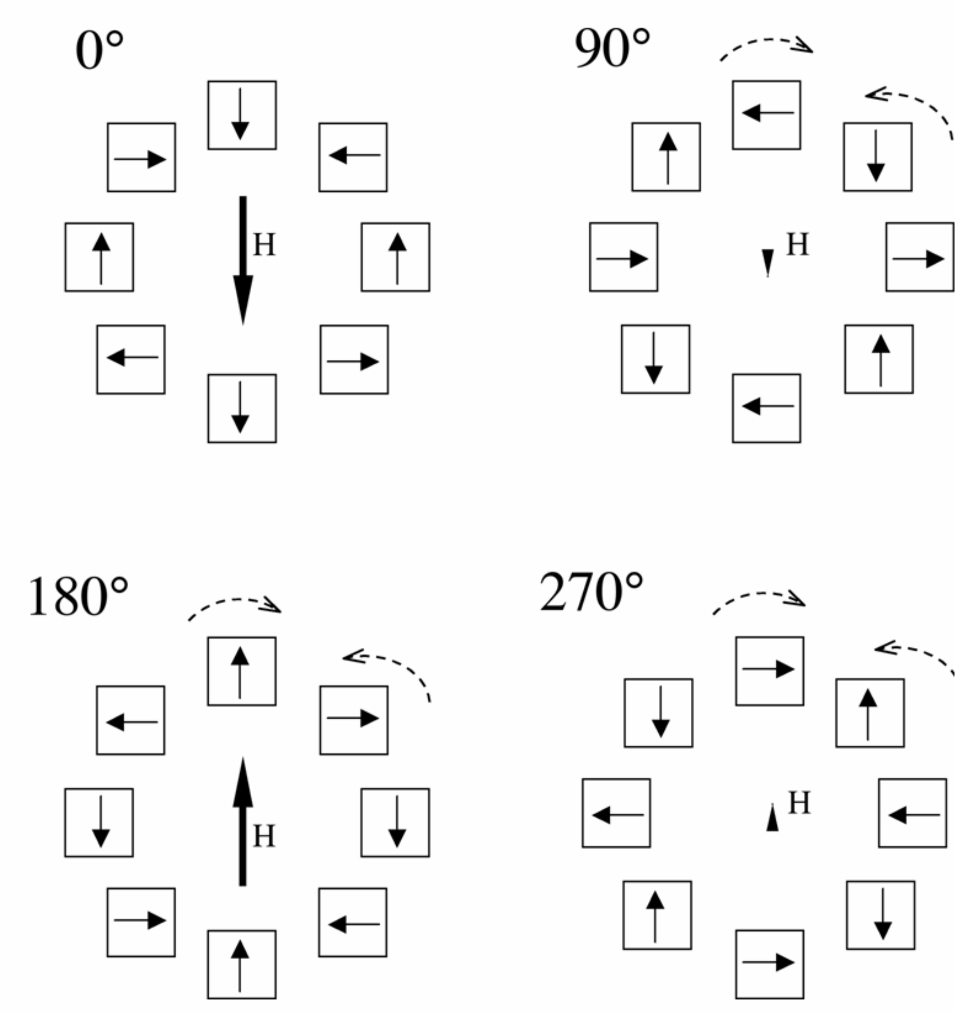

Figure 3.5: Magnet orientation and varying field of an approximate Halbach cylinder.[35]

Using the field of one magnet as a reference, at 0˚ the field is at its maximum. Rotating to 90 causes the field to reduce to approximately zero. Rotating from 90˚ to 180˚ increases the field in the opposite direction to its maximum. Rotating it more to 270˚ reduces the field to zero again.

The magnet mangle built was made from eight rectangular NdFeB magnets. Each magnet was 25 mm × 25 mm × 75 mm with their magnetization perpendicular to the long axis. The rotation of the magnets was performed using a stepper motor and could complete a hysteresis loop in < 1 minute. During a test, the temperature near the cantilever was monitored and found not to vary by more than 0.2˚C. The maximum field of the device was 2300 Oe.

Chapter 4

Pulsed Laser Deposition: Results and Discussion

4.1 Introduction

Films of $Tb_{0.3}Dy_{0.7}Fe_{1.92}$ were deposited at different laser fluences on silicon cantilevers by PLD. One set of films was deposited at a high fluence (HF: 5-10 J/cm^2). The other was deposited at a lower fluence (LF: 2-5 J/cm^2). In addition, thinner films were deposited on TEM grids with low fluence conditions to allow the film to be characterized. The target for PLD was a 6.35 mm thick piece of $Tb_{0.3}Dy_{0.7}Fe_{1.92}$ purchased from Etrema Products Inc. It was cleaned in the procedure outlined in Chapter 2 before it was placed in C2. The chamber was baked at 200˚C for 24 hours before each deposition. The target was initially ablated with 10 hz laser pulses of 3 J/cm^2 to remove any oxide surface layer. Subsequent processing conditions for PLD deposition are listed in Table 4.1. Films were analyzed according to methods described in Chapter 3. This chapter presents the microstructure, chemical composition, and magnetic properties of $Tb_{0.3}Dy_{0.7}Fe_{1.92}$ films deposited by PLD.

Target	$Tb_{0.3}Dy_{0.7}Fe_{1.92}$
Laser	KrF
Laser Wavelength	248 nm
Laser Pulse Length	12 ns
Laser Pulse Rate	10 Hz
Laser Fluence	2.5 - 10 J/cm^2
Vacuum Base Pressure	$< 1\times10^{-8}$ torr
Vacuum Processing Pressure	$< 5\times10^{-7}$ torr
Substrate Temperature	300-330 K
Target to Substrate Distance	60 mm

Table 4.1: Processing conditions for films made by PLD.

4.2 *In-situ* PLD Process Monitor: Residual Gas and Optical Emission

PLD was performed in C2 where it was possible to determine the gases present during the process. Gas spectra inside the vacuum chamber were obtained with a SRS RGA200 residual gas analyzer (RGA). After the chamber was baked out, vacuum was typically less than 1×10^{-8} Torr. A spectrum of C2 at room temperature after baking is shown in Figure 4.1.

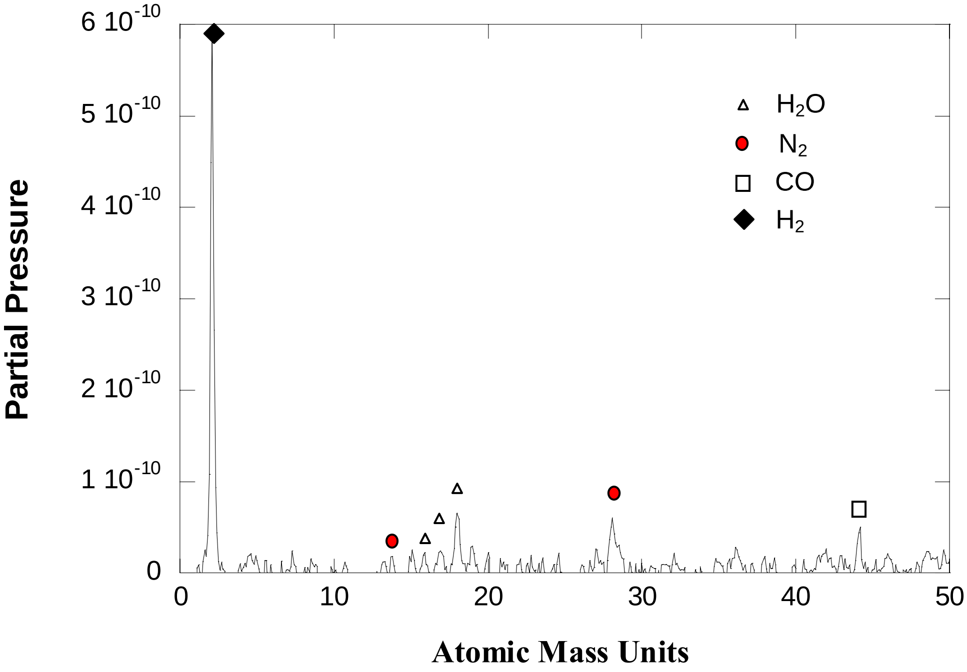

Figure 4.1: RGA spectrum of C2 at room temperature after baking at 200°C for 24 hours. Spectrum shows typical chamber conditions prior to deposition.

Typical residual gases and their atomic signatures are shown in Table 4.2. The spectrum shows that the chamber is clean. The major peak is at 2 AMU is from hydrogen and there are only low levels of water and nitrogen species present in the chamber. However, this does not mean that all contaminants have been removed from the chamber.

Air						
AMU	28	32	14	16	40	
Relative Intensity %	73	19.7	4.4	2.2	0.7	

Ar						
AMU	40	20	36	38	18	
Relative Intensity %	90.5	9	0.3	0.1	0.1	

CO						
AMU	44	28	16	12	45	46
Relative Intensity %	78.4	8.6	7.1	4.7	0.8	0.4

CO_2						
AMU	28	12	16	29	14	30
Relative Intensity %	91.6	4.6	1.8	0.9	0.9	0.2

H_2						
AMU	2	1				
Relative Intensity %	95.2	4.8				

He						
AMU	4					
Relative Intensity %	100					

N_2						
AMU	28	14	29			
Relative Intensity %	92.6	6.7	0.7			

O_2						
AMU	32	16	34	33		
Relative Intensity %	89.4	10.2	0.4	0.1		

H_2O						
AMU	18	17	16	20	19	
Relative Intensity %	74.4	17.1	8.2	0.2	0.1	

Table 4.2: Common residual gases, atomic mass units and relative intensities found in vacuum chambers.

Even after the rigorous cleaning, there are still gases absorbed on the target surface and surrounding fixtures. These can be seen during the laser cleaning process when they were continually being evolved (Figure 4.2). After laser cleaning, the spectral intensities of water and nitrogen were reduced but never completely eliminated.

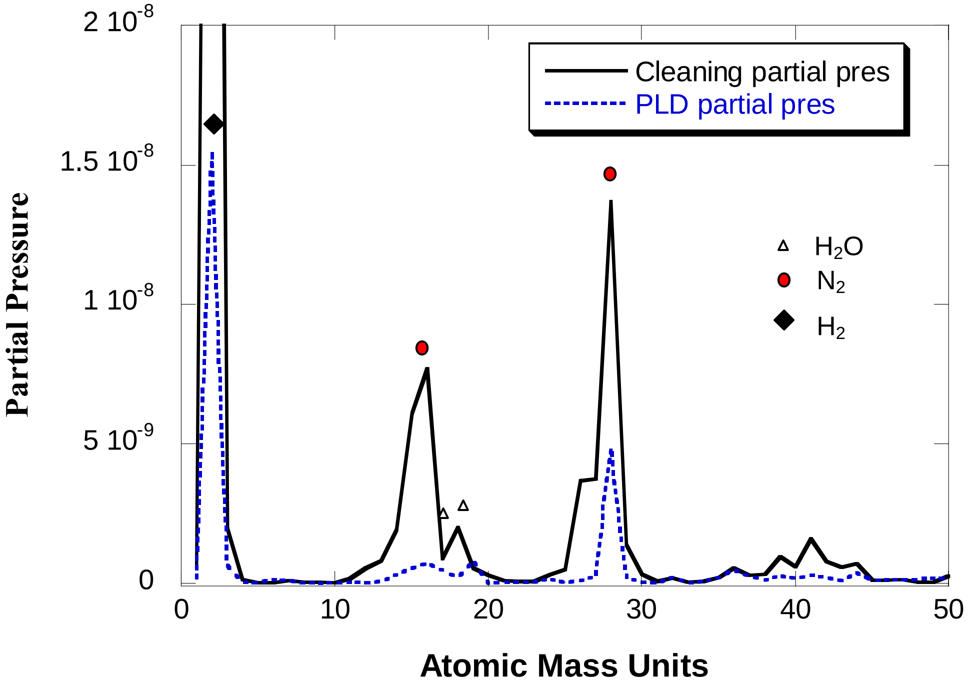

Figure 4.2: RGA spectra showing residual gases partial pressures during laser cleaning and PLD film deposition.

.

Another real-time analysis for PLD is the optical emission generated from the plasma. The OES was observed through a side port in the C2. A typical OES during PLD deposition is shown in Figure 4.3 along with a spectrum from an oxygen lamp for comparison. The spectrum shows almost no discernable peak from the major oxygen lines at 777.7 nm and 845.0 nm indicating that very low levels of oxygen are present in the plasma. This means that we can conclude that there were not significant amounts of oxygen present either on the surfaces of the target or vacuum chamber during deposition.

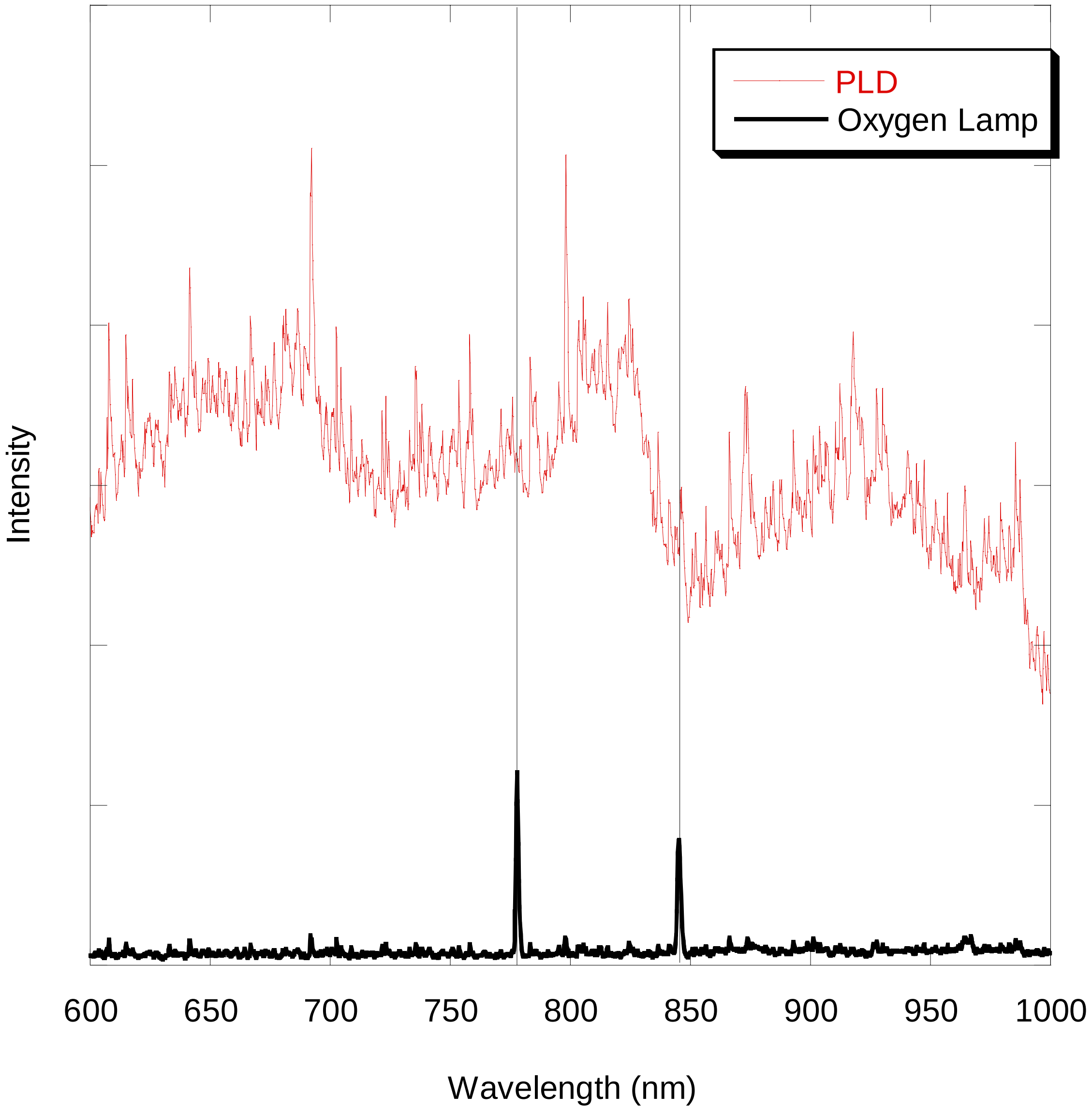

Figure 4.3: OES from PLD process and oxygen lamp.

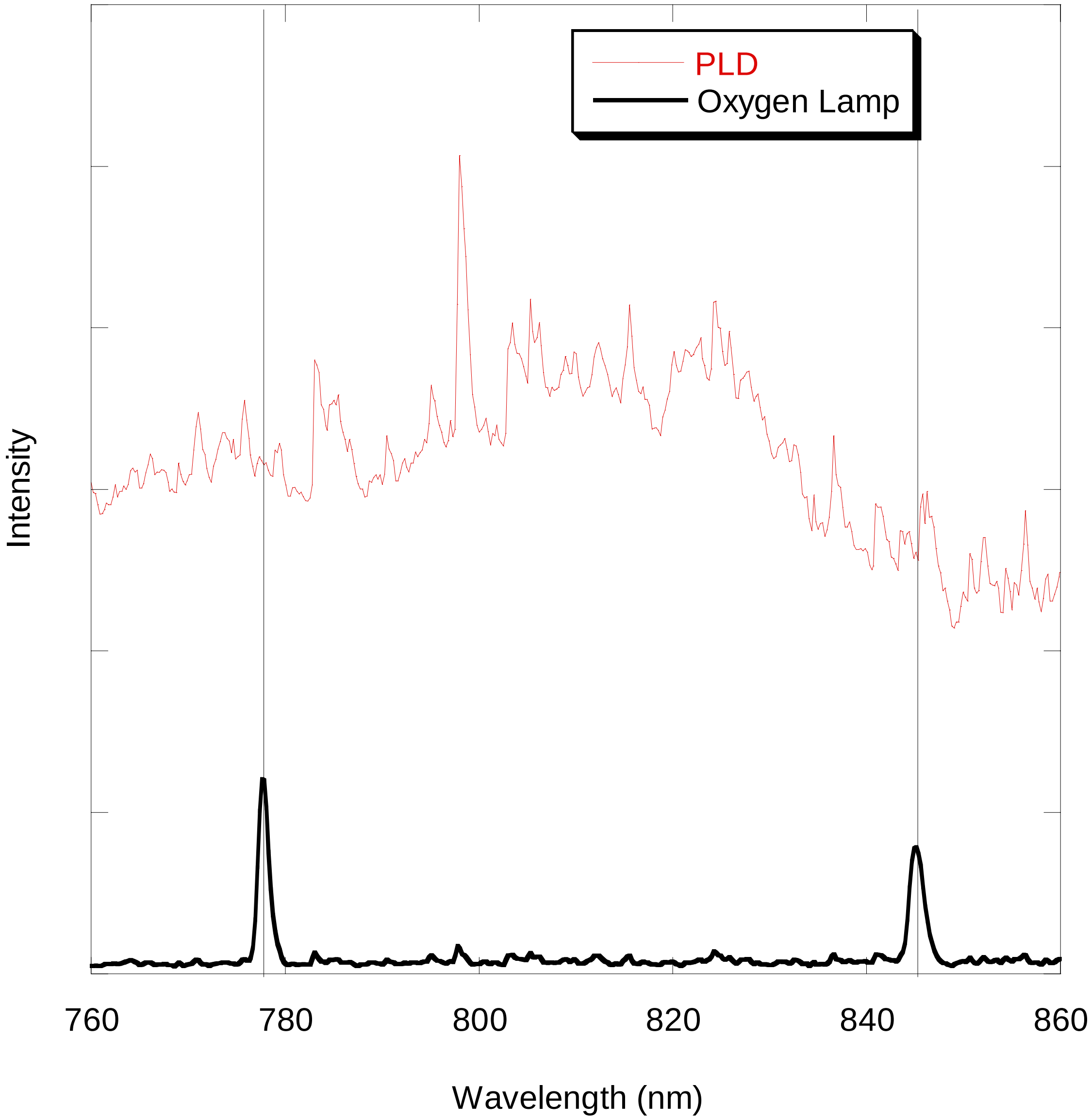

Figure 4.4: Enlarged OES from PLD highlighting oxygen emission lines at 777 and 845 nm.

4.3 Film Structure and Composition

PLD films were deposited on ultra thin, carbon-coated, copper grids (Electron Microscopy Sciences) to analyze their crystallinity and chemical composition. Films deposited on TEM grids were processed at LF conditions. The film covered the entire TEM grid. Figure 4.5 shows a high resolution TEM image of a representative PLD film along with the corresponding FFT. The film exhibits no evidence of crystallinity and the lack of systematic electron diffraction confirms that the films are amorphous. In addition, the lack of scattering shows that the film is dense. We know that a film is present and the image is not only the carbon grid because EDS indicates that the Fe, Dy and Tb are present. TEM EDS of using 2 nm diameter beams in various areas shows that the composition of the films is similar to the starting material.

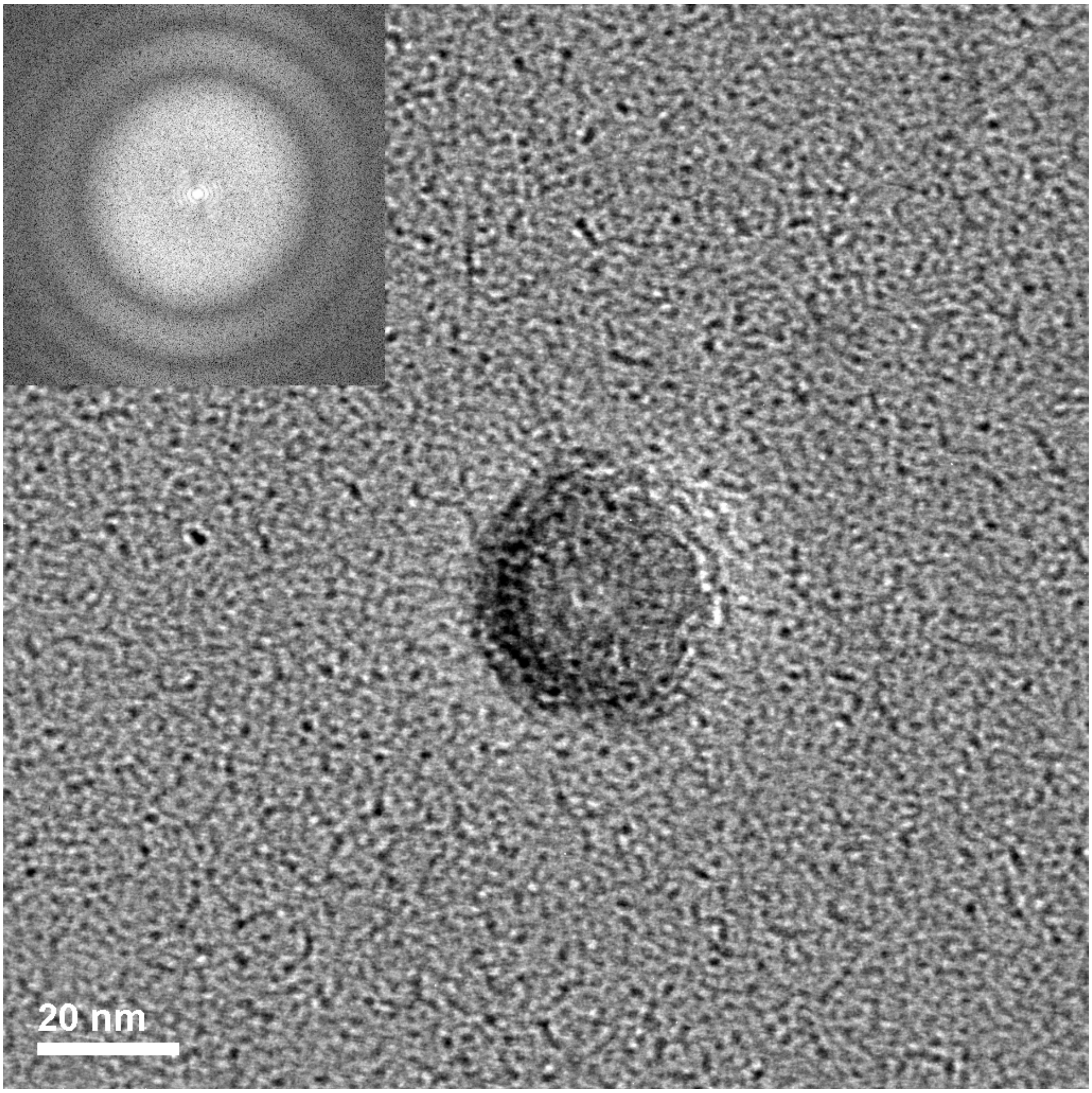

Figure 4.5: TEM image and fast Fourier transform of PLD film.

4.4 Film Analysis

4.4.1 Profilometry

Profilometry scans were performed to measure film thickness. Figure 4.7 shows a typical scan from the high fluence (HF) films. The force on the profilometer stylus was set at 25 mg so that the film would not be scratched. Profilometry of the two films deposited on silicon show that they are uniform in thickness over the entire cantilever. The high fluence (HF) PLD sample (Figure 4.6) is 400 nm thick while the low fluence (LF) PLD sample is 200 nm thick. With the small forces used on profilometers any obstruction causes the stylus to jump. The sharp peaks seen in the profilometer scans are from bumps in the film that result from splattering of droplets due to recoil pressure on the Knudsen layer during PLD and perhaps some dust on the surface. Scans across the top and the bottom were taken to check the uniformity of the deposited films.

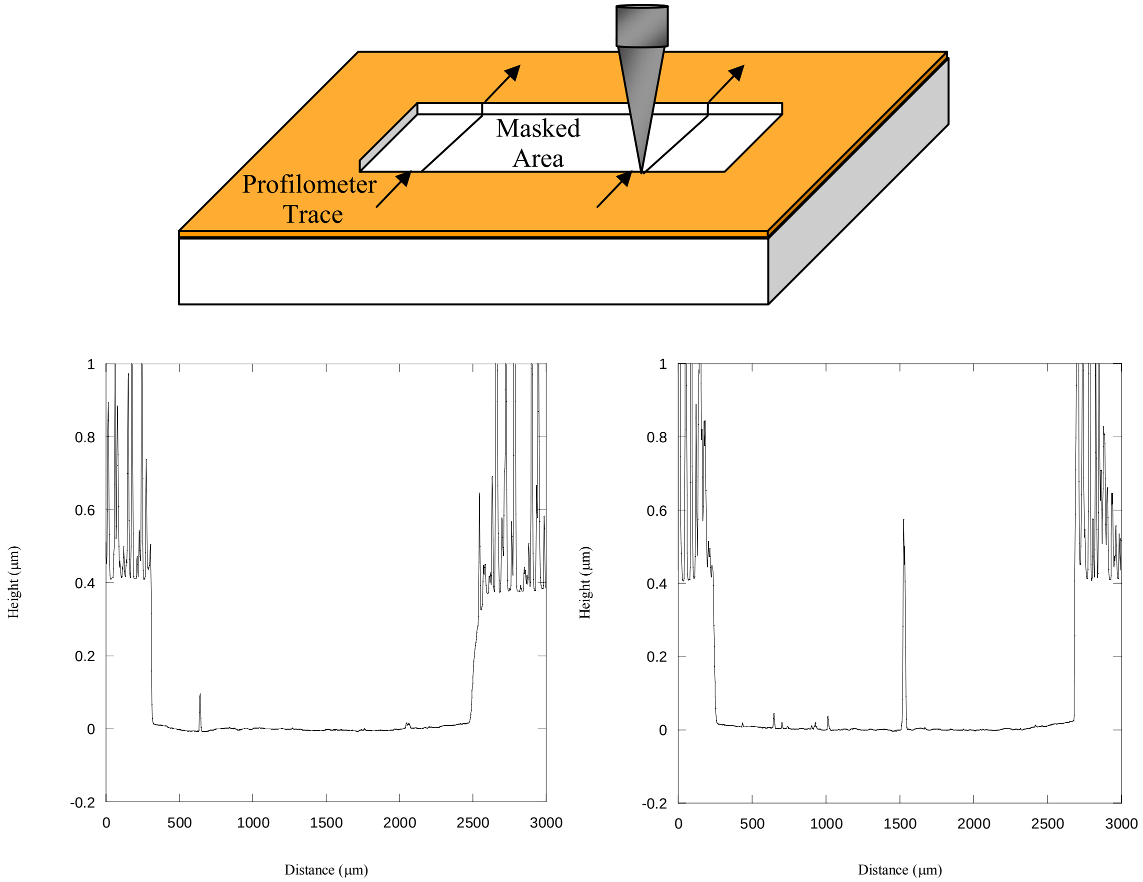

Figure 4.6: Profilometry scans for HF PLD films across area masked by the cantilever beam.

4.4.2 Optical Microscopy and SEM

Visually, both the HF and LF PLD films are mirror-like with a gold tinge. Under the optical microscope circular splatters are plainly seen on the film. Figure 4.7 shows that the bumps are more abundant and larger for the HF PLD sample. The larger bumps are expected for HF PLD because the higher fluence generates a larger recoil pressure on the Knudsen layer.[16] This recoil pressure is what pushes molten material from the target causing it to splatter onto the substrate.

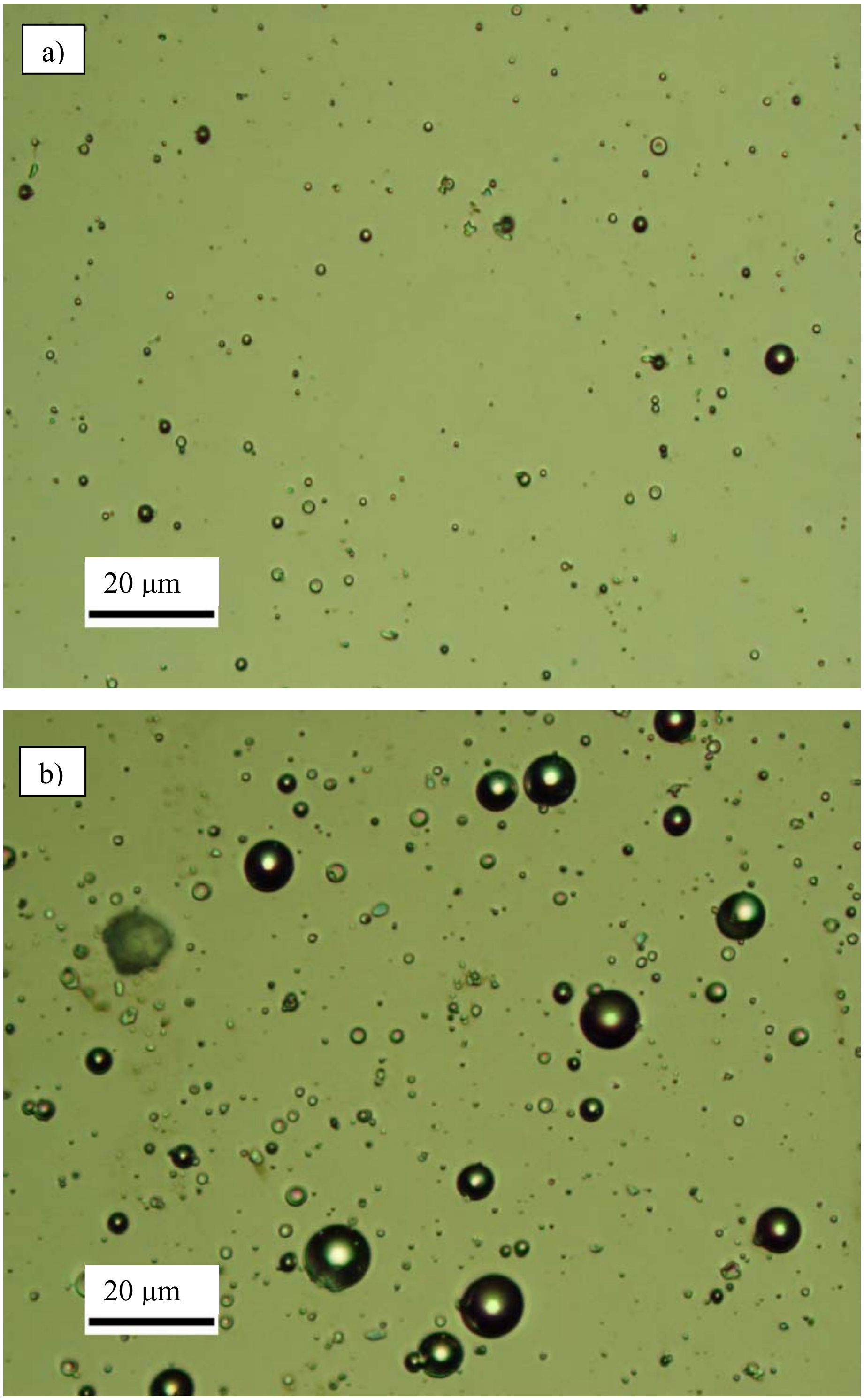

Figure 4.7: Optical images of a) LF PLD film and b) HF PLD film.

SEM images (examples are shown in Figures 4.8 and 4.9) show that the size of the splatter in the HF sample ranges from a tens-of-nanometers to 12 µm while the splatter in the LF sample ranges from a few nanometers to 8 µm. EDS mapping (Figure 4.10) of a smooth area and splatter show that there is no difference in composition between the smooth regions of the films and the spattered regions.

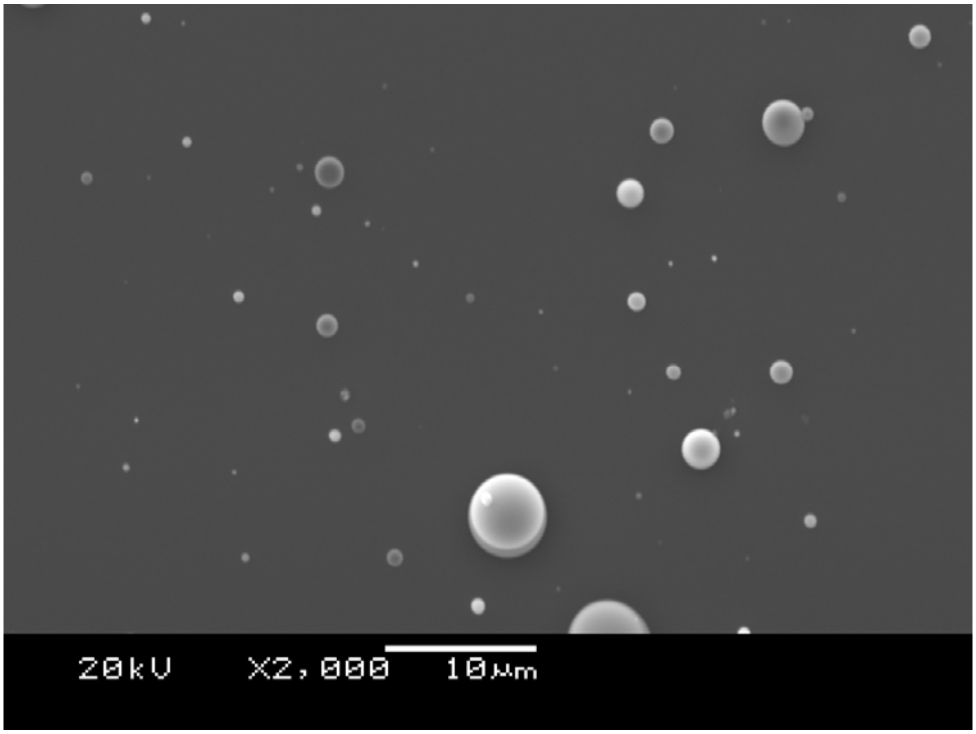

Figure 4.8: SEM micrograph of LF PLD film.

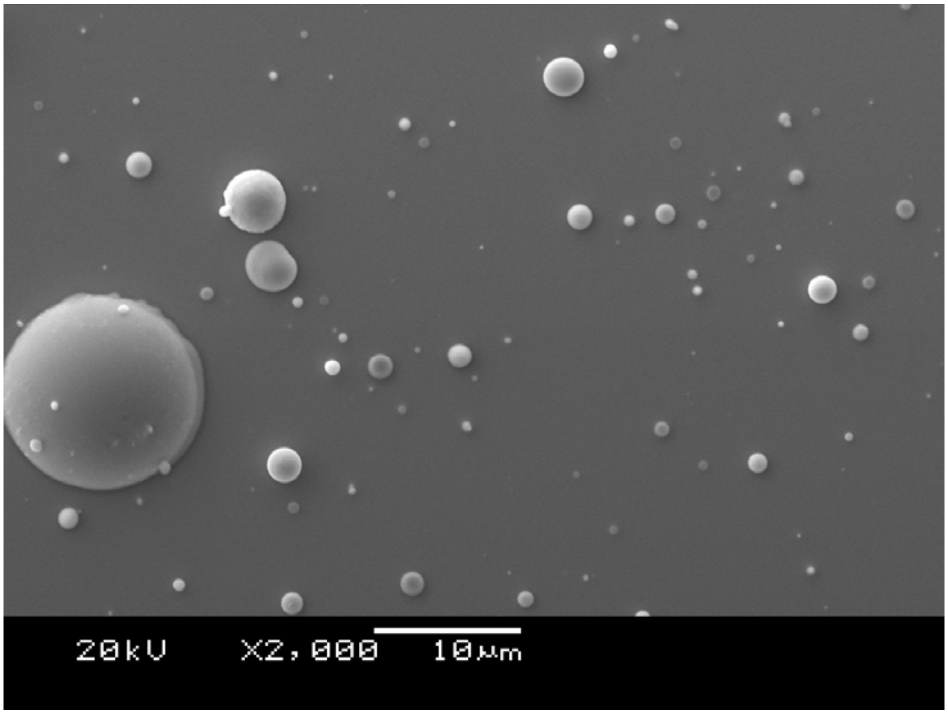

Figure 4.9: SEM micrograph of HF PLD film.

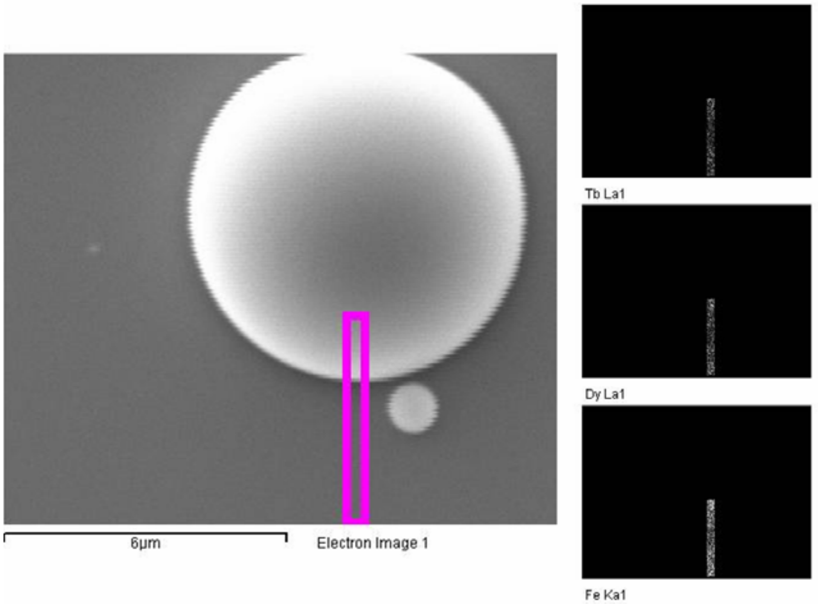

Figure 4.10: SEM map of splatter and smooth parts of film and corresponding EDS maps of the same areas of Tb, Dy and Fe. Vertical rectange is region analyzed using EDS.

4.4.3 XRD

XRD was performed on both the HF and LF PLD films. Figure 4.11 shows the stacked spectra of the films. XRD of the films verifies that both films are amorphous. The only peak on the spectra is from the (400) peak from the silicon substrate.

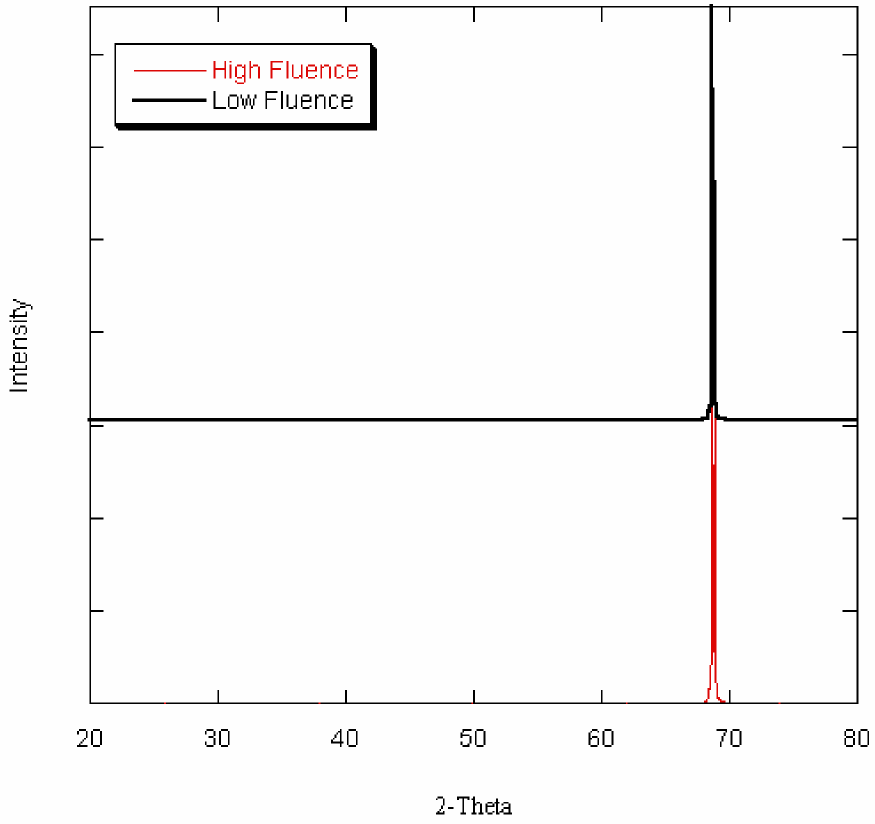

Figure 4.11: XRD of HF and LF PLD films.

4.5 Magnetic Properties

4.5.1 Magnetic Moment Measurements

Magnetization data from the two films was recorded using a SQUID magnetometer. The mass of the film was estimated from the volume with the assumption that the film density was the same as bulk density. SQUID measurements on microparticles show that the magnetization of bulk $Tb_{0.3}Dy_{0.7}Fe_{1.92}$ at a field of 10,000 Oe is 70 emu/g. In comparison, Figure 4.12 and 4.13 show the hysteresis loops for the HF and LF PLD specimens. The HF PLD sample have magnetization of 24 emu/g at the same applied field. The LF PLD sample had a lower magnetization (18 emu/g @ 10,000 Oe).

Previous work by Jenner et al. on PLD films using a CO_2 laser have shown no obvious correlation between magnetic quality and fluence.[37] If this is the case, then above the breakdown threshold there should be little difference between the HF and LF samples. The lower magnetization in the LF sample may be due to the greater surface area-to-volume ratio for the thinner LF films. The greater surface area-to-volume ratio means that a surface oxide of a particular thickness will degrade the magnetization of the thinner film more than the thicker film. As expected, the magnetization is lower than bulk $Tb_{0.3}Dy_{0.7}Fe_{1.92}$ because of the disorder in the amorphous structure reduces the exchange interaction. Both the LF and HF films exhibit soft magnetic properties. The LF film has a coercivity of 37 Oe and the HF film has a coercivity of 46 Oe. As expected, these values are much lower than the coercivity (~ 500 Oe) of bulk, microcrystalline $Tb_{0.3}Dy_{0.7}Fe_{1.92}$.

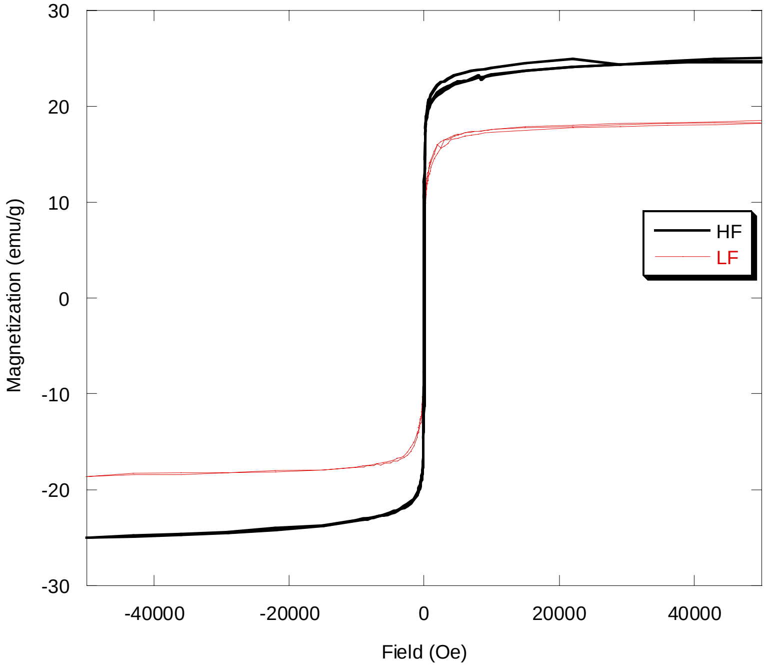

Figure 4.12: Hysteresis loops for HF and LF PLD films.

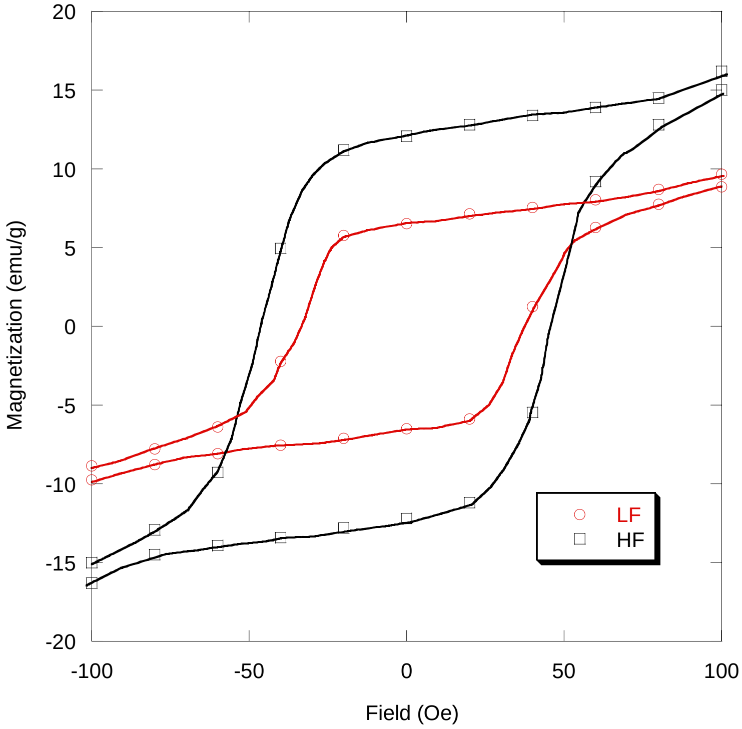

Figure 4.13: Low field portion of hysteresis curves for HF and LF PLD films.

4.5.2 Magnetostriction

The relationship between tip displacement and magnetic force was measured as function of applied field for the HF and LF PLD cantilever. This relationship was used to calculate the magnetostriction of the films. The optical cantilever method was used and the maximum applied field was 2300 Oe. This field is not sufficient to saturate $Tb_{0.3}Dy_{0.7}Fe_{1.92}$ films. Another complication in calculating magnetostriction from tip displacement is determination of Youngs modulus for thin films. Youngs modulus for bulk $Tb_{0.3}Dy_{0.7}Fe_{1.92}$ varies from 25- 35 GPa. Values used for amorphous thin films of Fe-Dy-Tb alloys have been reported from 30 - 120 GPa.[38-40] Here it is assumed to be 50 GPa. Poisson's ratio is also difficult to determine. However, magnetostriction is not a strong function of Poissons ratio and therefore there is little error associated with small errors in Poissons ratio. For the magnetostriction calculation, we assumed it is the same as silicon (0.27).

Figures 4.14 and 4.15 show the tip deflection and magnetostriction for a HF PLD film, respectively. The measured coercive field for magnetostriction is low (~80 Oe) and is in agreement with our SQUID measurements. Tip deflection is still increasing and magnetostriction is far from saturation at the maximum field that could be applied using our test setup. Thus, the values of magnetostriction that were calculated represent a lower bound. Tip deflection and magnetostriction for a LF PLD film is presented in Figure 4.16 and 4.17. Film data and magnetostriction results are shown in Table 4.3.

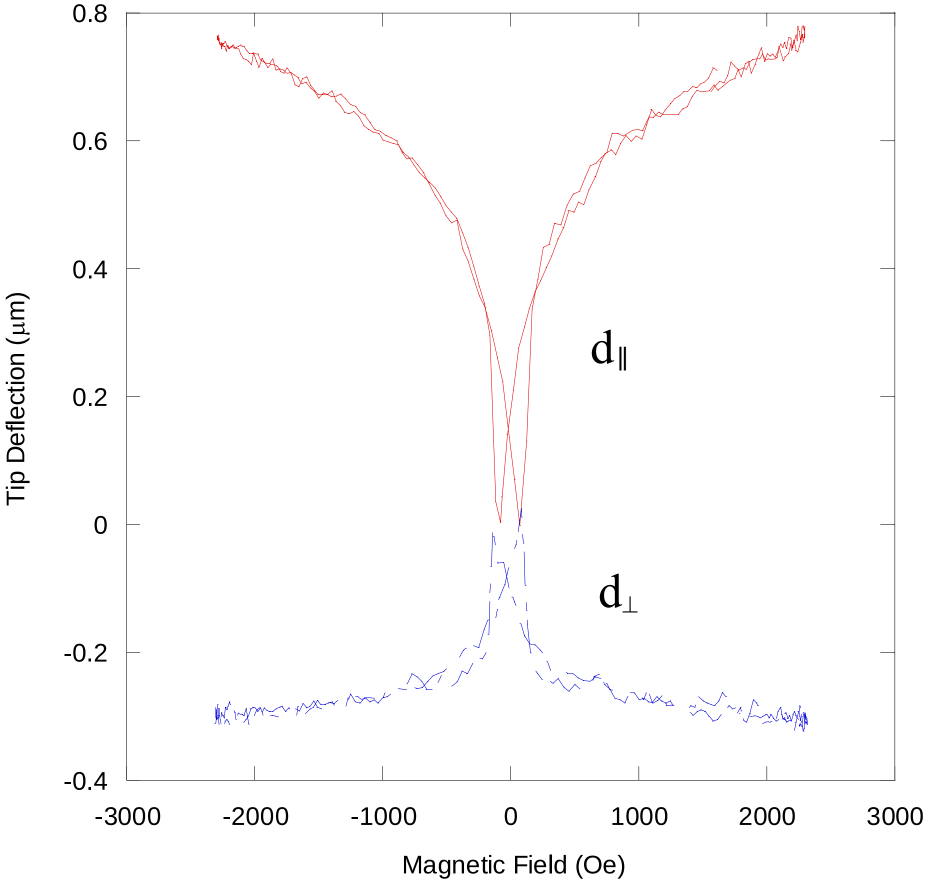

Figure 4.14: Parallel and perpendicular cantilever tip deflection for HF PLD film.

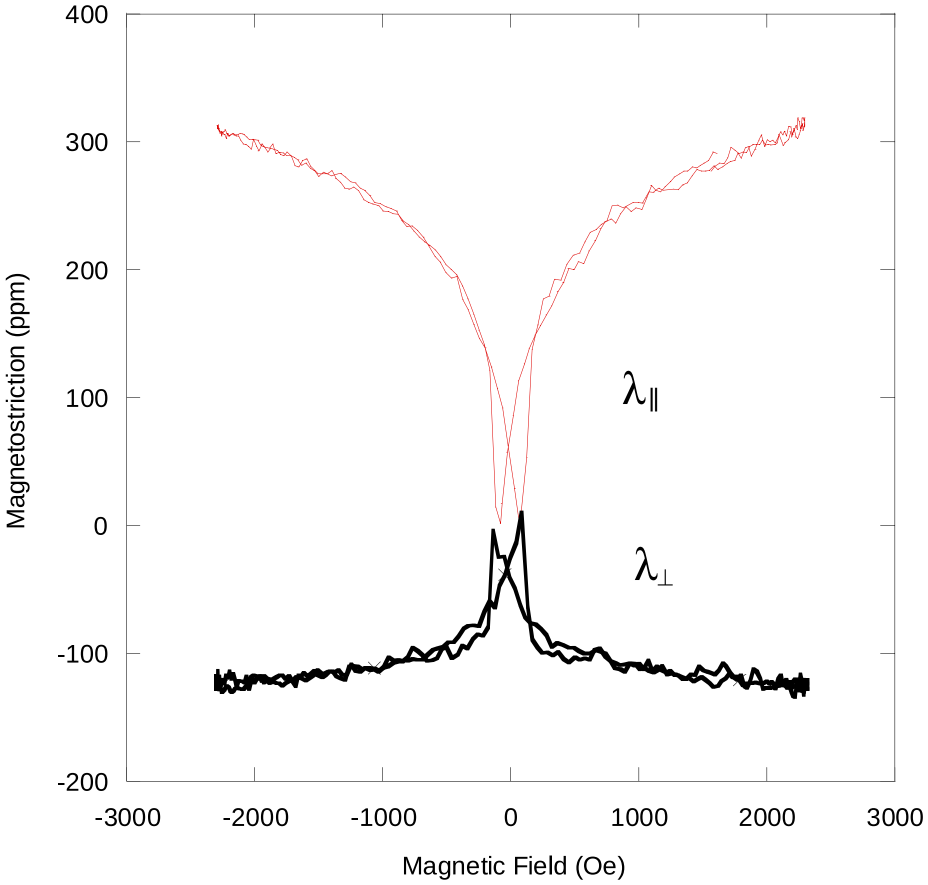

Figure 4.15: Parallel and perpendicular magnetostriction for HF PLD film.

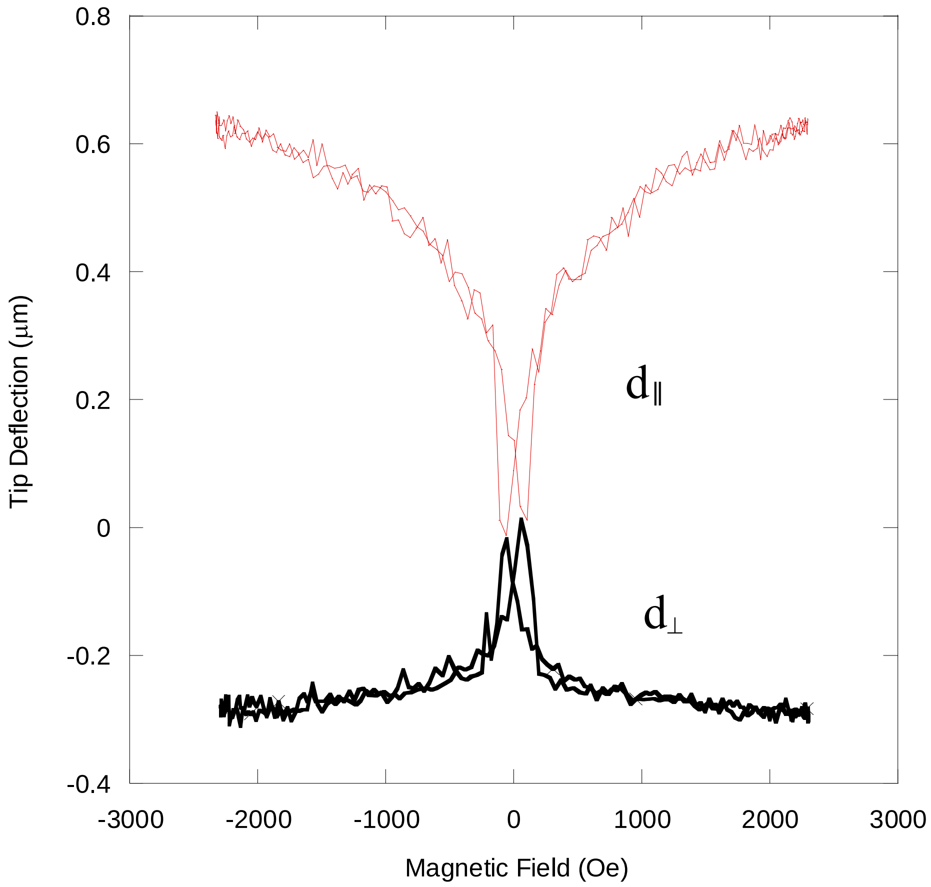

Figure 4.16: Parallel and perpendicular cantilever tip deflection for LF film.

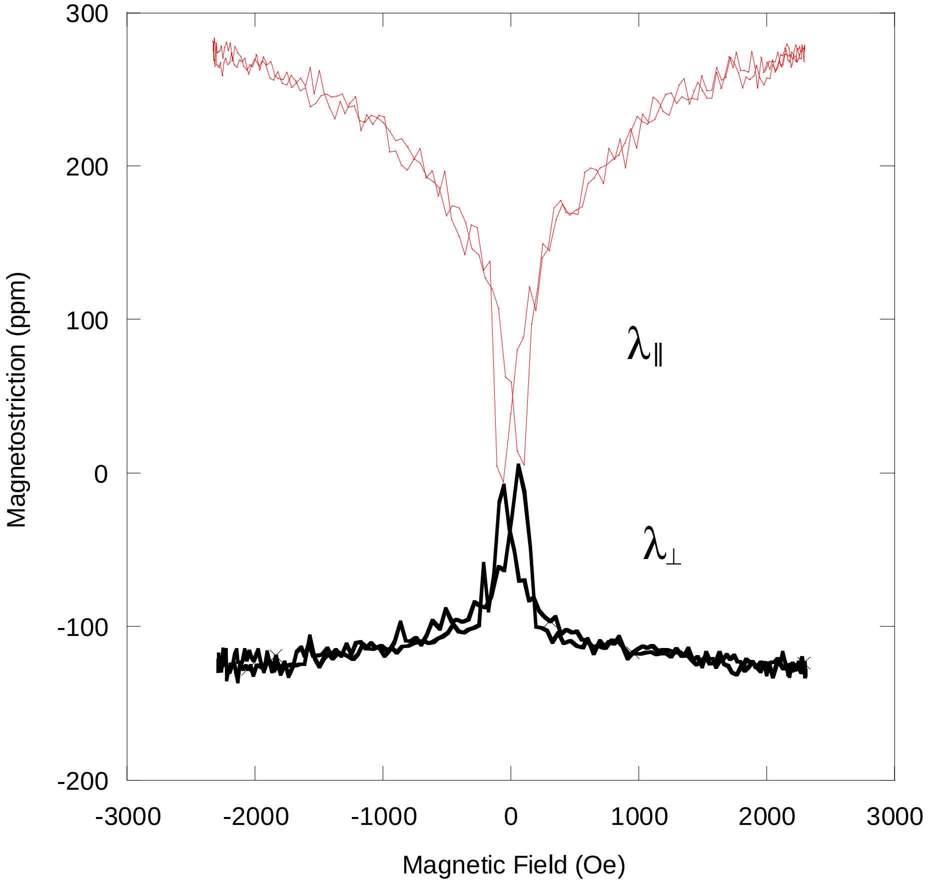

Figure 4.17: Parallel and perpendicular magnetostriction for LF PLD film.

		HF KrF PLD	**LF KrF PLD**
Substrate	**Thickness (µm)**	125	125
	Youngs Modulus (GPa)	107	107
	Poissons Ratio	0.27	0.27
Film	**Length (µm)**	8.25	11.3
	Thickness (µm)	400	200
	Youngs Modulus (GPa)	50	50
	Poissons Ratio	0.27	0.27
	Measured Tip Deflection (µm)	1.06	0.92
	Measured Magnetostriction (ppm)	285	268

Table 4.3: HF and LF PLD film data.

Table 4.4 compares the magnetic properties of the deposited $Tb_{0.3}Dy_{0.7}Fe_{1.92}$ PLD films with other film processing methods. The magnetostriction of the HF PLD films produced in this study is similar to films produced by other methods. However, the coercivity of our films were slightly higher. This may be due to the splatters in the film.

	KrF HF PLD	**ArF PLD**[37]	**MBE Sputtered**[40]	**Ion Beam Sputtered**[8]
Film Composition	$Tb_{0.3}Dy_{0.7}Fe_{1.92}$	$Tb_{0.3}Dy_{0.7}Fe_{1.95}$	$Tb_{0.3}Dy_{0.7}Fe_{1.56}$	$Tb_{0.3}Dy_{0.7}Fe_{2.0}$
As Deposited Crystallinity	Amorphous	Crystalline	Amorphous	Amorphous
Substrate Temperature (K)	300		575	330
Youngs Modulus (GPa)	50	45	50	
Poissons Ratio	0.27			
$\lambda_{\parallel}$(ppm) at 2300 Oe	305	250	250	310
Film Thickness (μm)	0.4	0.178	270-350	
Coercivity (Oe)	46	~10	~10	

Table 4.4: Comparison of magnetic properties of as deposited films.

4.6 Conclusions

Films of $Tb_{0.3}Dy_{0.7}Fe_{1.92}$ have been successfully deposited at two fluences. Both films are dense and amorphous as determined by TEM and XRD. The stoichiometry of the target has been preserved in the films which is critical to producing films with high magnetostriction. The films have a lower magnetization and lower coercivity compared to bulk crystalline material due to their amorphous structure and possibly due to some oxidation of the surface. Their magnetic properties and magnetostriction are similar to thin films of amorphous $Tb_{0.3}Dy_{0.7}Fe_{1.92}$ made by other methods. Splattering of the molten layer during deposition leaves large spheres of material embedded in an otherwise smooth film. The splatters may be the cause for the higher coercivity. However, they do not affect the magnetostriction of the $Tb_{0.3}Dy_{0.7}Fe_{1.92}$ film since composition of the splatters is similar to the rest of the film.

Chapter 5

Flat Plate Ablation: Results and Discussion

5.1 Introduction

Some of the first pulsed laser experiments to intentionally produce nanoparticles were by Smalley et al.[17] In these experiments, bulk material was locally vaporized using an intense laser and vapor was ejected into a gas at atmospheric pressure. The vapor cooled rapidly and condensed into nanoparticles.

Flat plate ablation (FPA) can be easily scaled up and produce a large number of nanoparticles quickly. Films of nanostructured magnetostrictive materials produced by FPA, however, have yet to be studied. In this study, FPA was used on $Tb_{0.3}Dy_{0.7}Fe_{1.92}$ to study the effects of processing conditions on nanoparticle structure, composition and magnetic properties.

5.2 Processing

Using FPA, nanoparticles were produced by ablating a solid $Tb_{0.3}Dy_{0.7}Fe_{1.92}$ target in 1 atm of flowing helium gas. Processing conditions for these experiments are listed in Table 5.1. Details and schematics are presented in Chapter 2. Ablation takes place in the ablation chamber above chamber 1 (C1). The nanoparticles were then accelerated through a 250 μm nozzle by the pressure differential between the ablation chamber (760 Torr) and the deposition vacuum chamber (~200 mTorr). The ablated particles reach velocities between 300-1000 m/sec, depending on particles size and gas type,[23] before impacting onto alumina substrates (CoorsTek, AD996). Micron thick films are deposited by translation of the substrate holder. A KrF laser is used at a fluence of 1.56 – 2.5 J/cm^2. Nanoparticle structure and composition is presented in this chapter along with film structure and magnetic properties.

Target…………………………………………………………	$Tb_{0.3}\,Dy_{0.7}\,Fe_{1.92}$
Laser………………………………………………………	KrF
Laser Wavelength…………………………………………	248 nm
Laser Pulse Length……………………………………...	12 ns
Laser Pulse Rate………………………………………...	10 Hz
Laser Fluence…………………………………………...	1.56 - 2.50 J/cm^2
Horncell Base Pressure……………………………………	2×10^{-7} Torr
Horncell Processing Pressure……………………………..	760 Torr
Carrier Gas………………………………………………..	He (99.999%)
Gas Flow Rate……………………………………………	3000 sccm
Nozzle Size………………………………………………..	250 μm
C1 Pressure During Depositon……………………………	0.15 – 0.20 Torr
Substrate…………………………………………………...	Al_2O_3
Substrate Temperature……………………………………	300 - 320 K
Nozzle-to-Substrate Distance……………………………....	2 mm

Table 5.1: Processing conditions for particles and films made by FPA.

The KrF laser was directed onto a solid target inside the ablation chamber in a similar manner to PLD. The ablation chamber was purged > 5 times with (99.999%) gas before it was pumped to high vacuum by the turbo pump in C1 though a 6.35 mm tube. Although, the ablation chamber was UHV compatible, the ultimate base pressure was limited to 2×10^{-7} Torr. Because of the complexity of the parts (i.e. the virtual impactor, quartz windows and feeding nozzle) there are a number of Viton rubber o-ring seals, which required careful baking using heating tapes and a heat gun. The temperature was monitored to prevent overheating and degradation of the seals which would cause a vacuum leak, contaminate C1 and force an emergency stop of the turbo pump. After the ablation chamber was baked and pumped, it was filled with clean (99.999% purity) helium gas. The target was then laser cleaned with 2000 laser pulses at 2 J/cm^2 before films of FPA nanoparticles were deposited onto the substrate.

5.2 Optical Emission Spectroscopy for FPA

OES was used to monitor the FPA process for contaminates from the carrier gas, target surface or leaks in the vacuum. After detailed cleaning and leak checking, we were able to remove most contaminates from the process. A typical optical emission spectrum during film deposition for FPA of a solid $Tb_{0.3}Dy_{0.7}Fe_{1.92}$ target is shown in Figure 5.1. There are no increases of intensity at the 778 nm and 845 nm wavelengths which would indicate low levels of oxygen present during the ablation process.

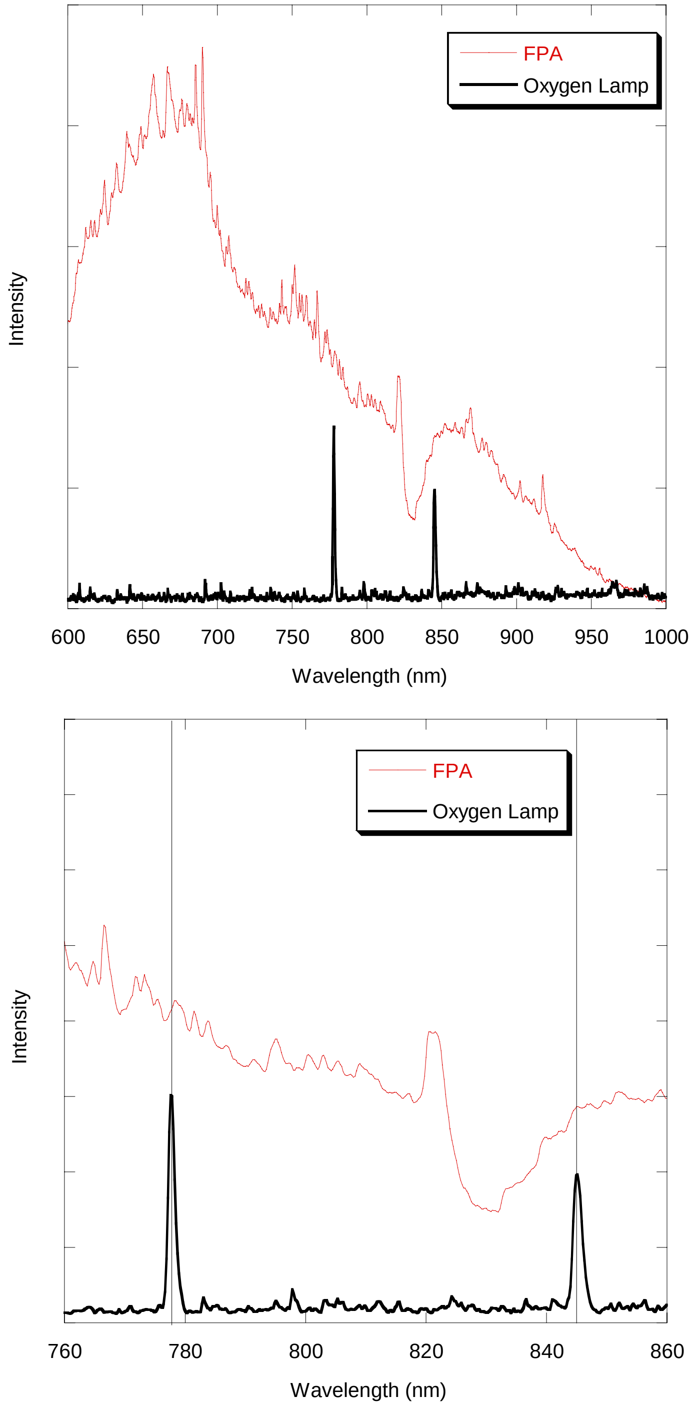

Figure 5.1: a) OES from FPA. b) Expanded view of OES highlighting the region containing the two major oxygen peaks.

5.3 Structure of Nanoparticles by FPA

Nanoparticles from the FPA process were jet deposited onto lacey carbon on copper grids (Electron Microscopy Sciences) for TEM analysis. The nozzle-to-substrate distance in C1 was raised to ~ 6 mm for these experiments to avoid blow out of the carbon film by the carrier gas and deposition of too many particles on the TEM grid. Figure 5.2 shows TEM images of particles produced by FPA.

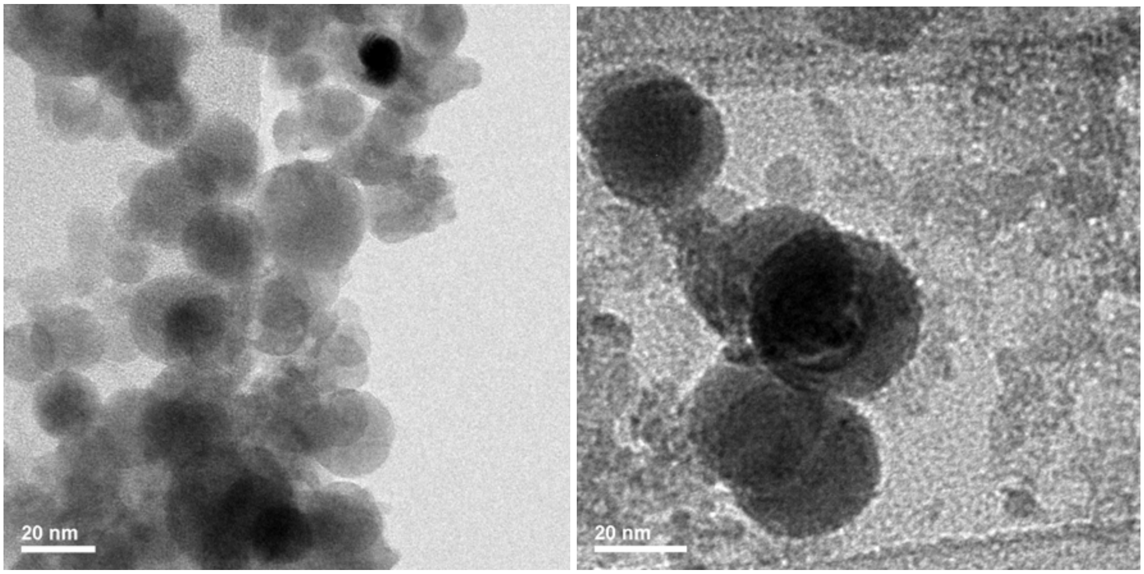

Figure 5.2: TEM micrographs of nanoparticles created by FPA.

The size distribution of nanoparticles is broad for the FPA process as expected. Size distributions could not be quantified due to the extensive agglomeration of the nanoparticles resulting in overlapping of particles. Visualization experiments of FPA by Koch et al. (Figure 5.3) by laser induced scattering on metals in helium in 1 atm of stagnant gas show that the expansion of the material plume is non-uniform and thus the collision frequency of vaporized material varies according to position.[41] In the plasma, the material reaches temperatures of 10,000 K. Upon cooling the coalescence also occurs non-uniformly leading to a broad size distribution of ablated material.

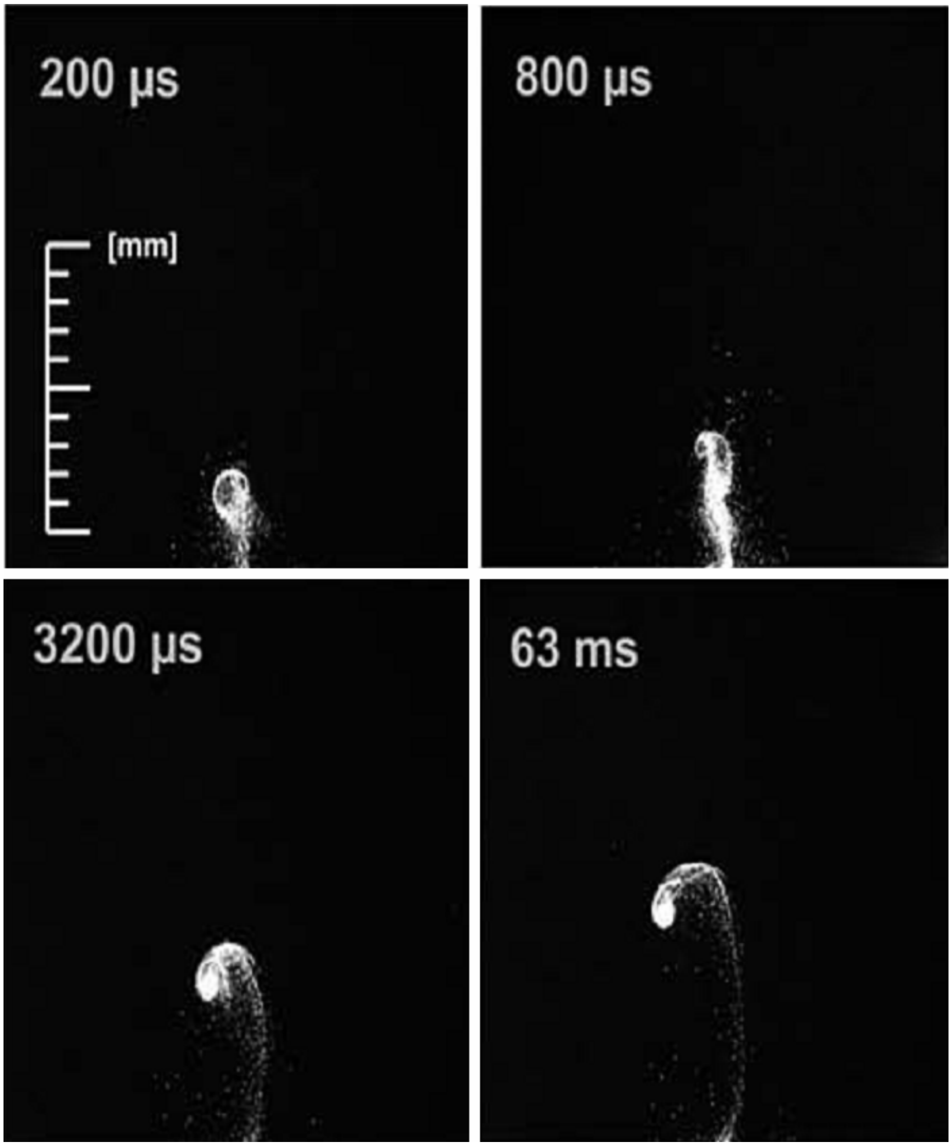

Figure 5.3: Visualization of FPA by Ti:sapphire laser in 1 atm of He gas.[41]

5.4 Properties of Nanostructured Films by FPA

5.4.1 Film Profile and Deposition Rate

Films of $Tb_{0.3}Dy_{0.7}Fe_{1.92}$ nanoparticles were deposited at different fluences on alumina substrates by rastering the x-y motor controlled substrate holder in C1. For all experiments, the laser was kept at a repetition rate of 10 Hz. Diagonal scans across the film were taken using a stylus profilometer. A profile for a typical film is showing in Figure 5.4. Film thickness ranged from 5 – 50 μm. Deposition rates were measured from the mass of the films for each laser fluence.

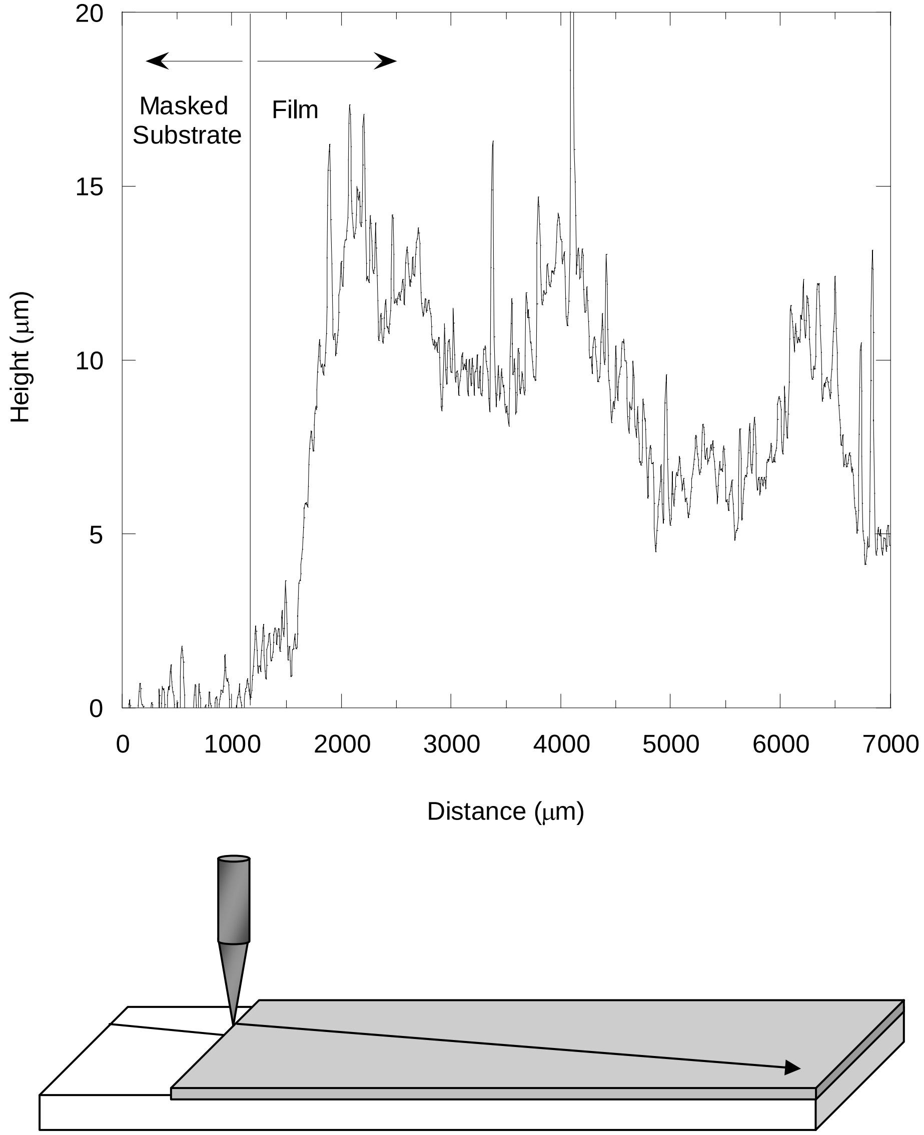

Figure 5.4: Stylus profilometry scan showing a typical film profile.

Figure 5.5 shows that the deposition rate increases with laser energy which is expected because more material is ejected as the laser energy per pulse is increased.

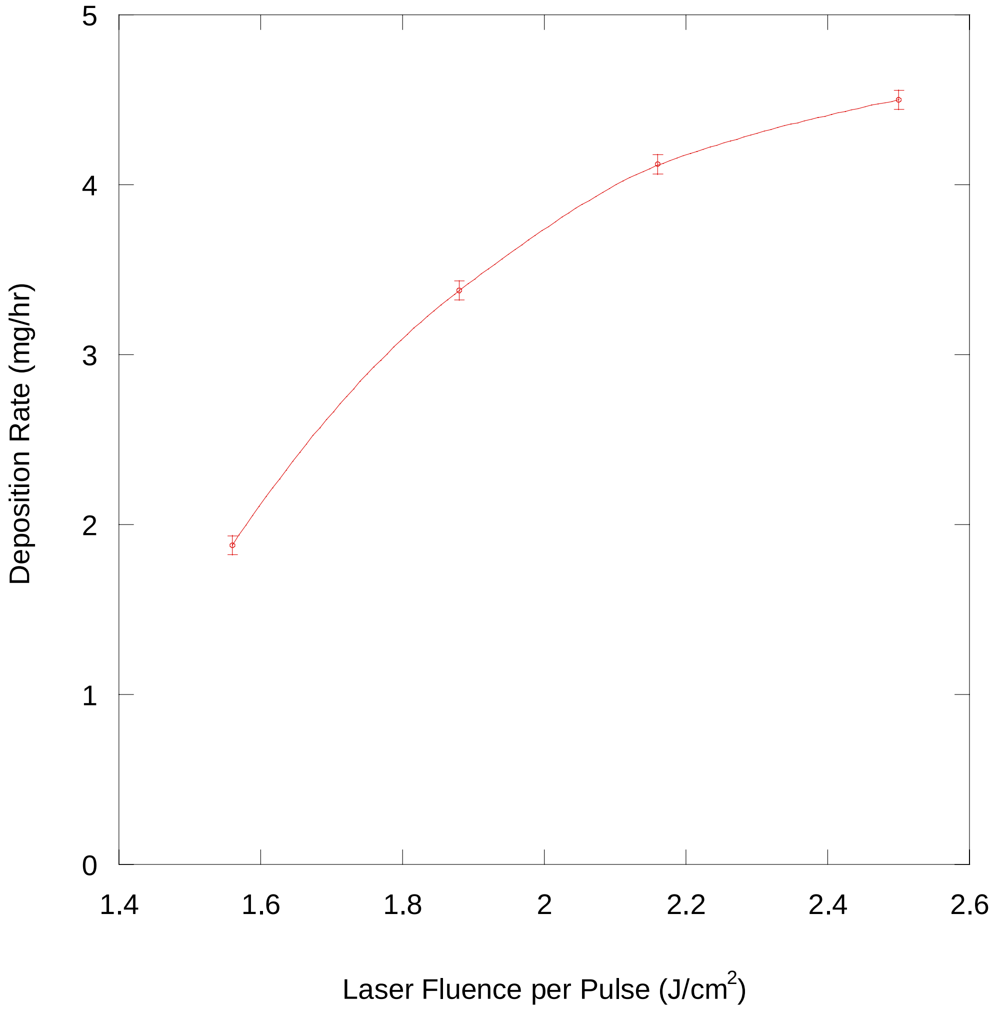

Figure 5.5: Deposition rate observed as a function of laser fluence per pulse.

5.4.2 Film Structure and Composition

Figures 5.6 – 5.9 are SEM micrographs of plan view and cross-sectional views of the films deposited at the various fluences. A typical SEM EDS spectrum of a FPA film is shown in Figure 5.10.

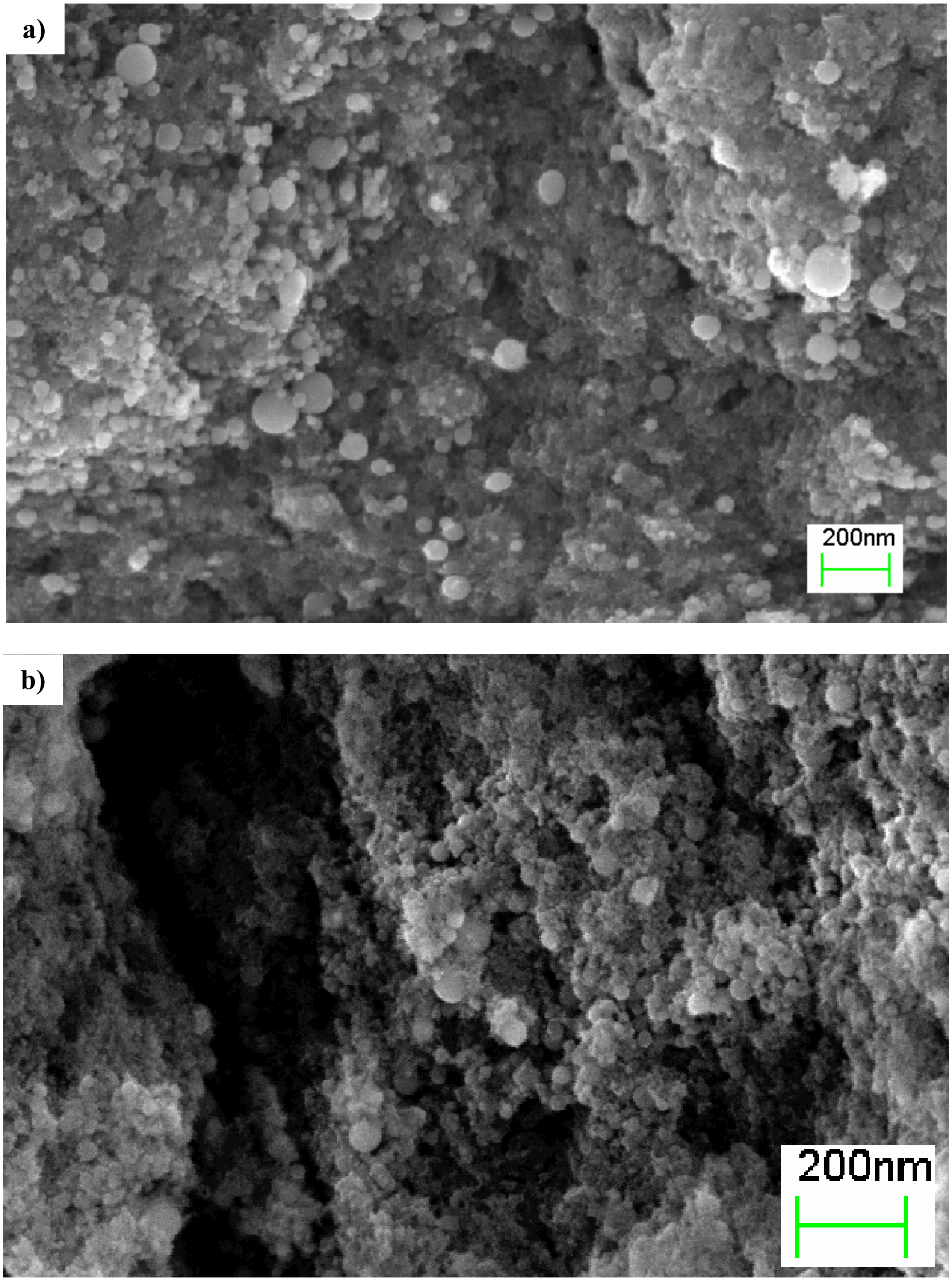

Figure 5.6: SEM micrographs of nanostructured film produced by FPA at 1.56 J/cm^2: a) plan view of film and b) cross-section of film.

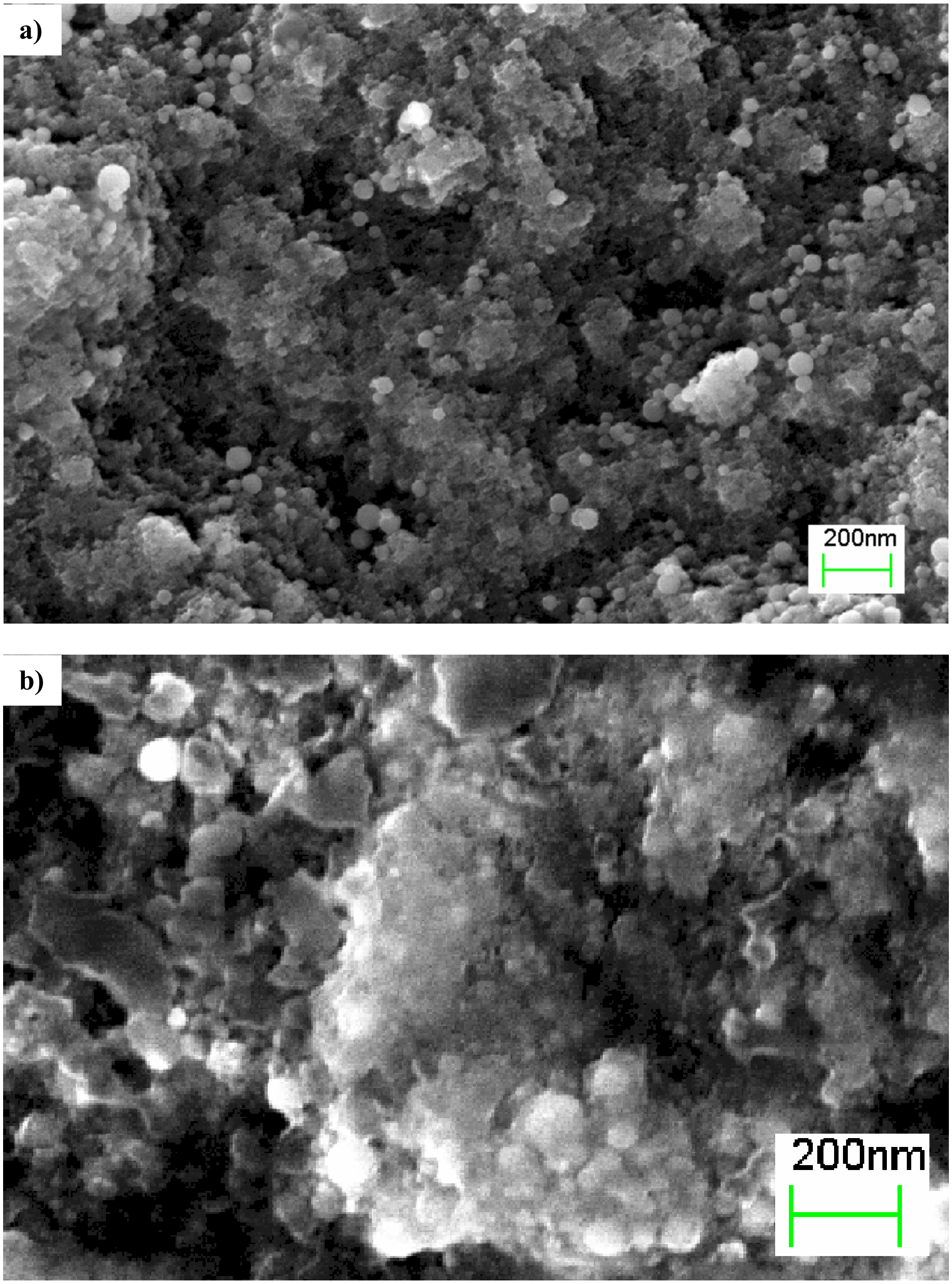

Figure 5.7: SEM micrographs of nanostructured film produced by FPA at 1.88 J/cm^2: a) plan view of film and b) cross-section of film.

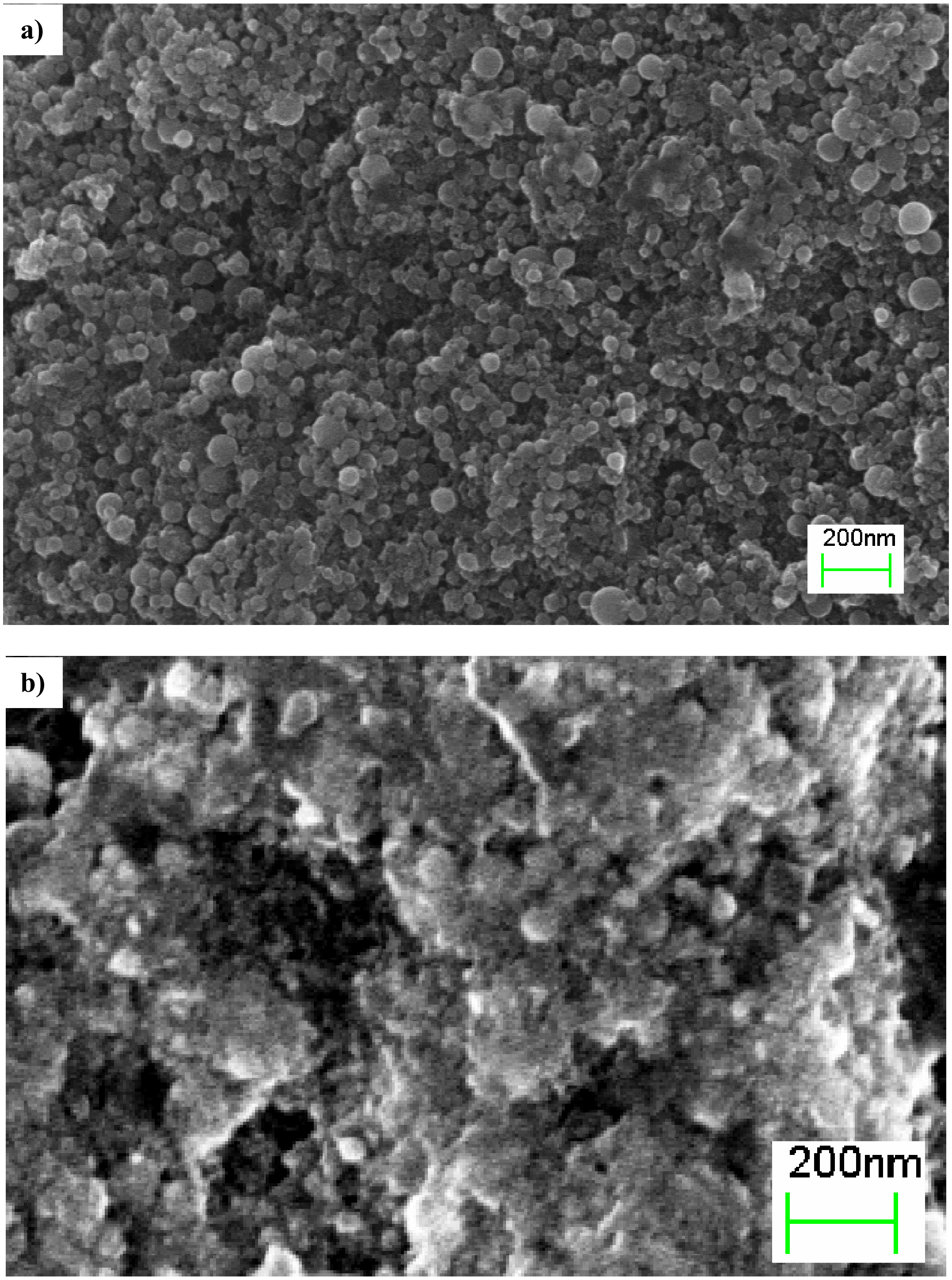

Figure 5.8: SEM micrographs of nanostructured film produced by FPA at 2.18 J/cm^2: a) plan view of film and b) cross-section of film.

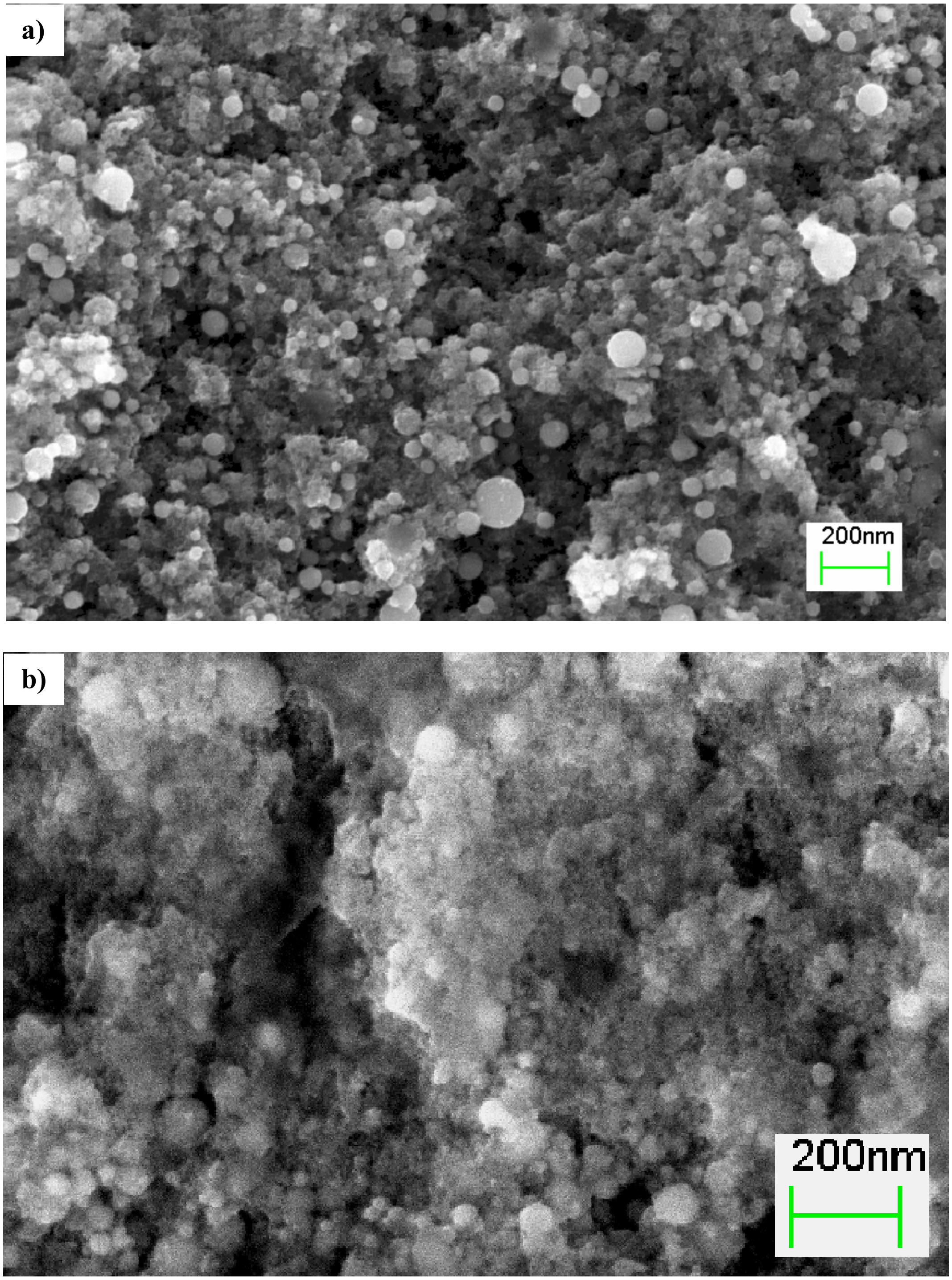

Figure 5.9: SEM micrographs of nanostructured film produced by FPA at 2.5 J/cm^2: a) plan view of film and b) cross-section of film.

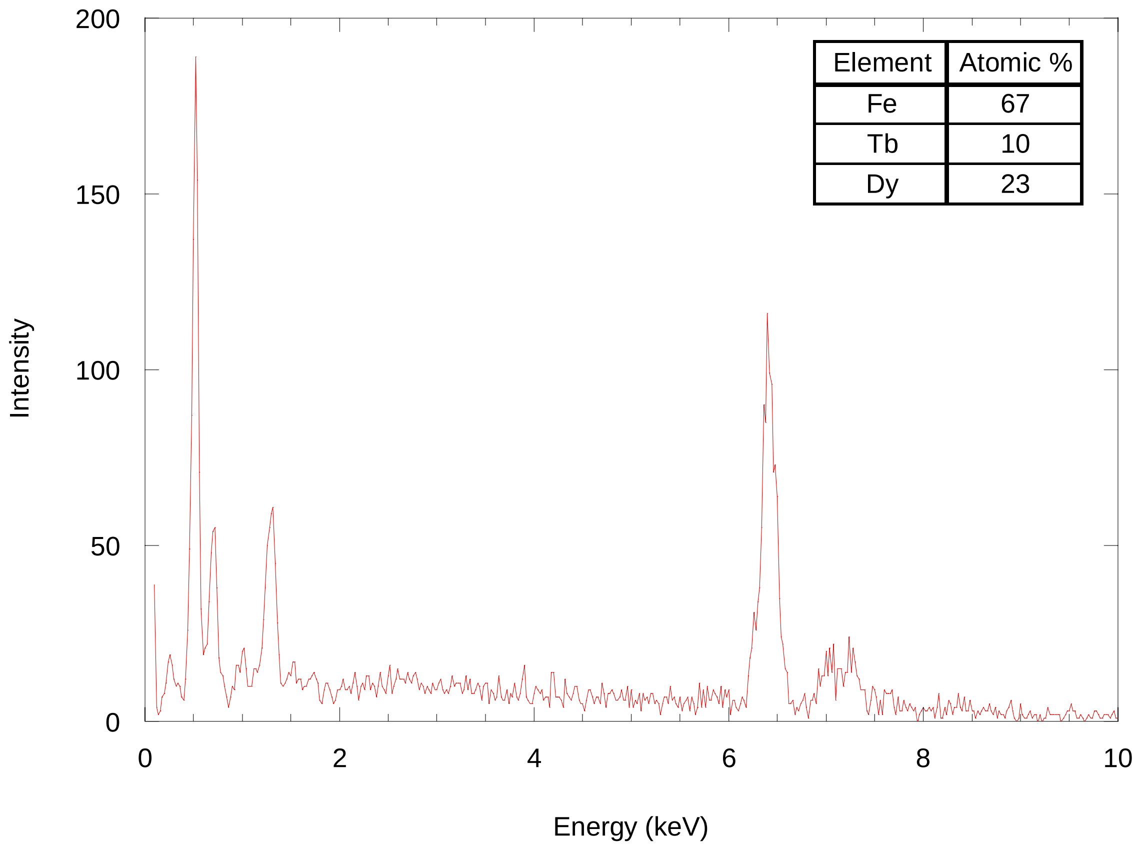

Element	Atomic %
Fe	67
Tb	10
Dy	23

Figure 5.10: SEM EDS scan of film produced by FPA.

It is clear from the SEM micrographs that the morphological features that are visible in the images increase in size with increasing fluence. The SEM EDS shows that the ratio of Fe to rare earth elements in the films is approximately 2:1 which is approximately the same as the $Tb_{0.3}Dy_{0.7}Fe_{1.92}$ target.

XRD scans of the FPA films are displayed in Figure 5.11. Other than some weak scattering between 2θ = 30°-35°, all peaks correspond to the alumina substrate which means the films are amorphous.

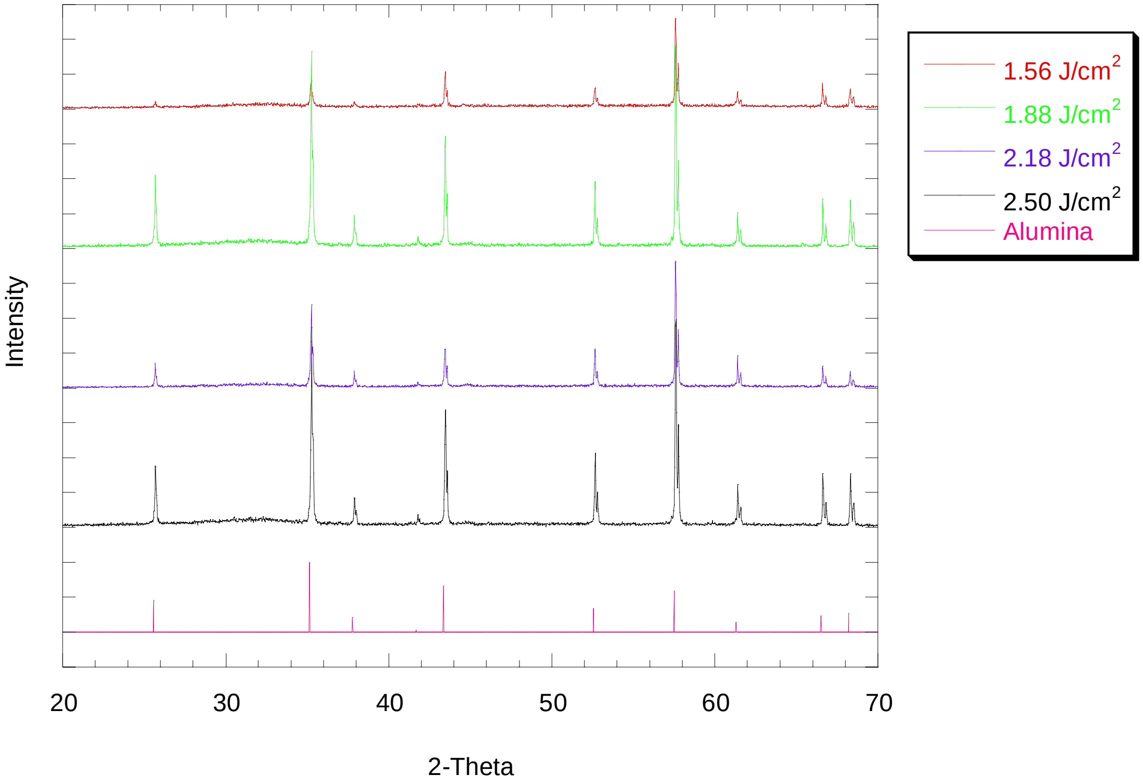

Figure 5.11: XRD scans of FPA films. All peaks in plot correspond to Al_2O_3.

5.4.3 Magnetic Properties

Magnetic measurements require that the mass of the films be measured. However, nanostructured films deposited by jet deposition are porous and thus it is difficult to determine the mass of the film by measuring the volume due to the unknown density of the deposited films. To overcome this problem, the mass of the film was directly measured on a thermal gravimetric analyzer (TGA) which had a measured accuracy of +/- 0.015 mg. Substrates were first weighed on the TGA. After deposition, the substrate and film were weighed together and the mass of the film determined by subtraction. Films made by FPA weighted between 0.55-0.91 mg.

Magnetic properties of the FPA films were measured using a SQUID magnetometer. Figures 5.12 – 5.15 show hysteresis loops for the film deposited at different laser fluences.

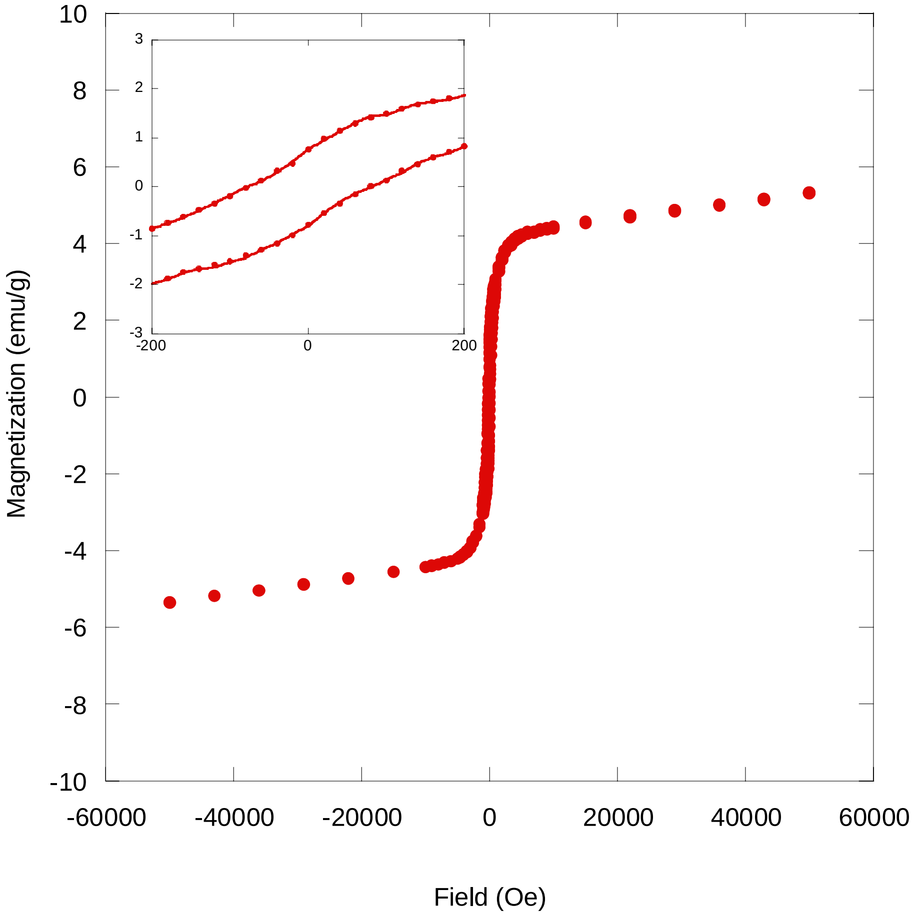

Figure 5.12: Hysteresis loop for film made by FPA at 1.56 J/cm^2. Inset shows low field region.

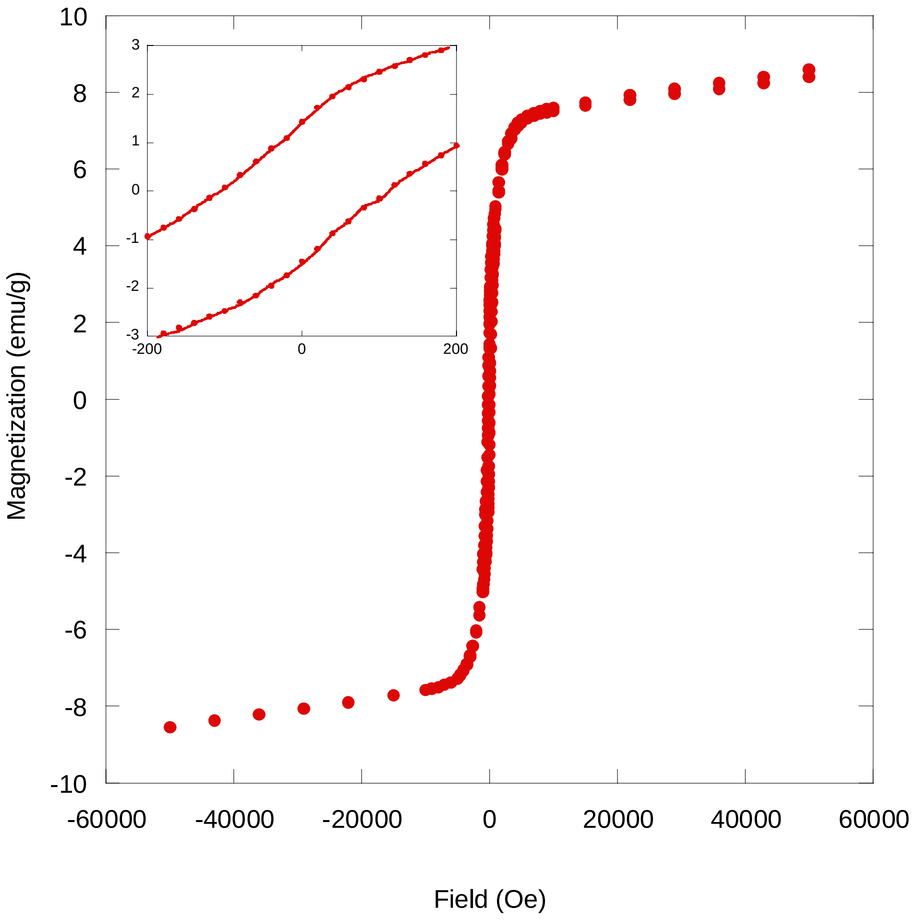

Figure 5.13: Hysteresis loop for film made by FPA at 1.88 J/cm^2. Inset shows low field region.

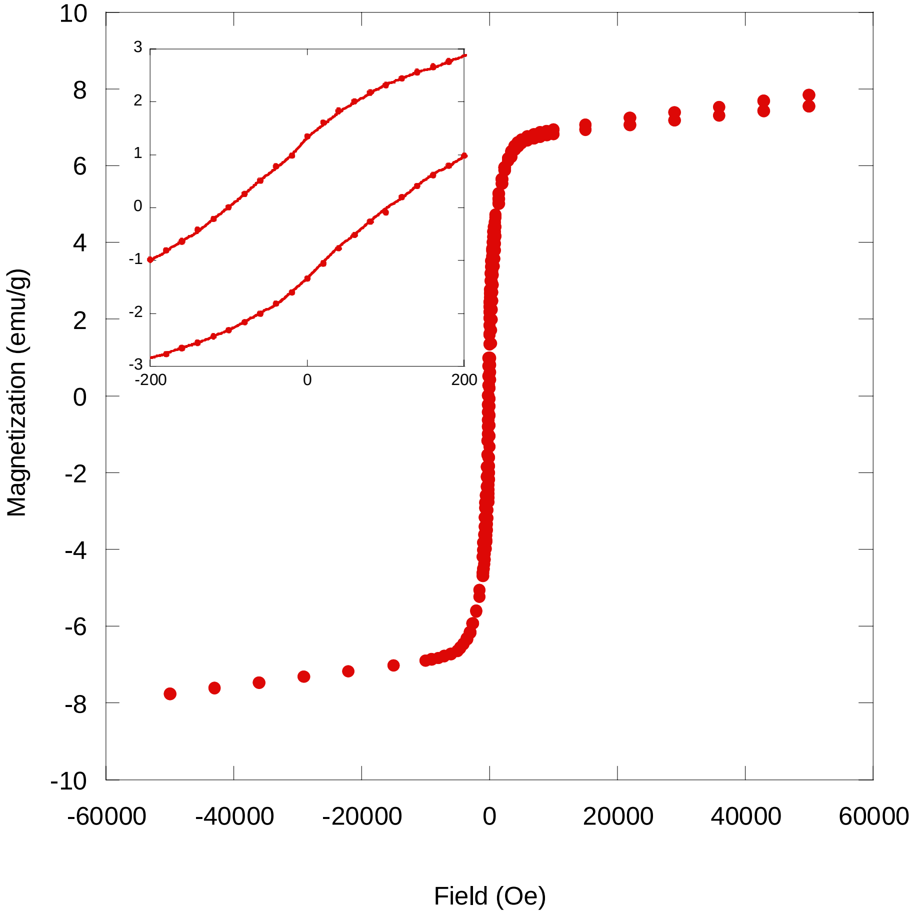

Figure 5.14: Hysteresis loop for film made by FPA at 2.18 J/cm^2. Inset shows low field region.

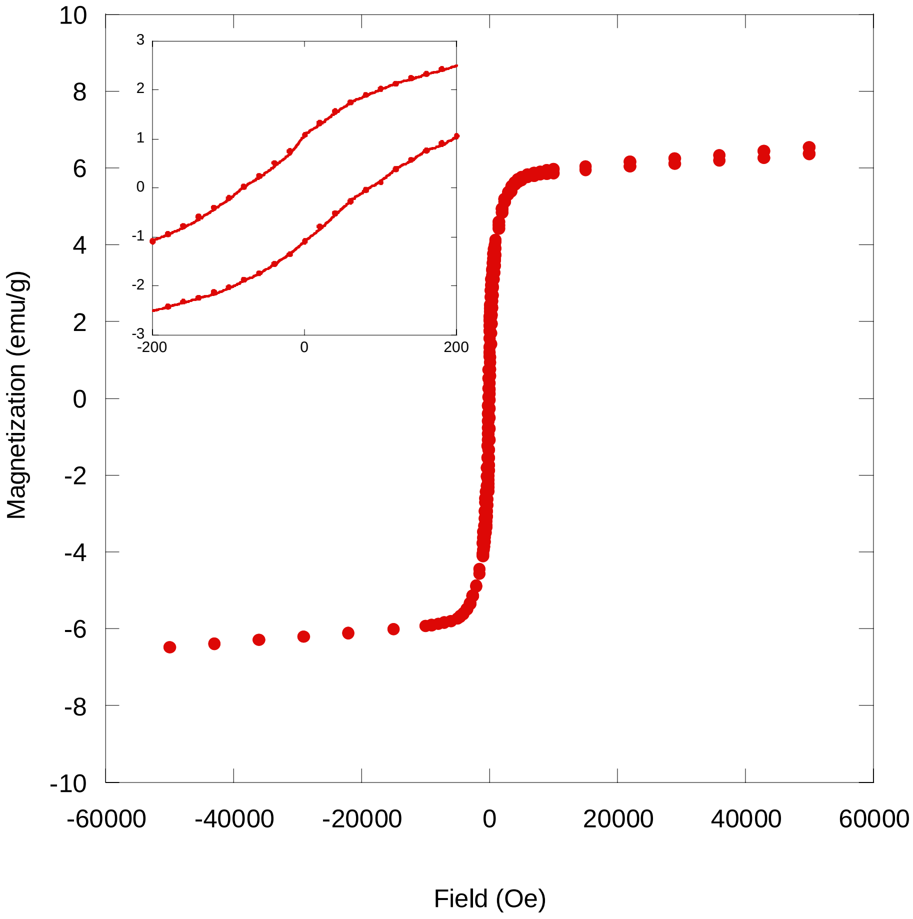

Figure 5.15: Hysteresis loop for film made by FPA at 2.50 J/cm^2. Inset shows low field region.

Saturation magnetization (M_s) is defined here as the magnetization at 10,000 Oe. SQUID measurements indicate no obvious correlation between fluence and saturation magnetization for the range of fluence studied, with the exception of the film produced at 1.58 J/cm^2. At this fluence the energy was probably less than the breakdown threshold for $Tb_{0.3}Dy_{0.7}Fe_{1.92}$, which explains the lower saturation magnetization for this film. For the films produced at the higher fluences, the saturation magnetization varied from 6.0 to

7.6 emu/g for films made with laser energies between 1.88 - 2.50 J/cm^2. The coercivities were lower than for bulk $Tb_{0.3}Dy_{0.7}Fe_{1.92}$ for all FPA films and ranged from 87 - 116 Oe.

Figure 5.16 presents the saturation magnetization and the coercivity of the FPA films. From this plot, it seems that there is a maximum in saturation magnetization at a fluence of 1.88 J/cm^2. However, this is not consistent with the microstructures presented earlier and thus an alternative method of plotting the data was investigated. In Figure 5.17, M_s is plotted in the chronological order of sample production and laser shots.

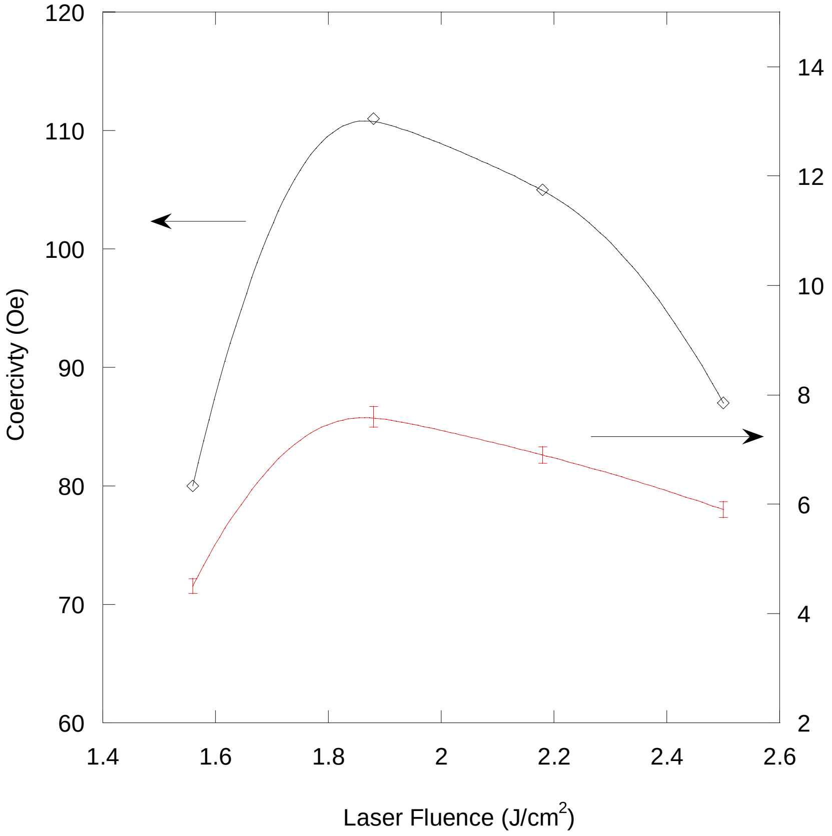

Figure 5.16: Saturation magnetization and coercivity for FPA films produced at laser fluences of 1.58-2.50 J/cm^2.

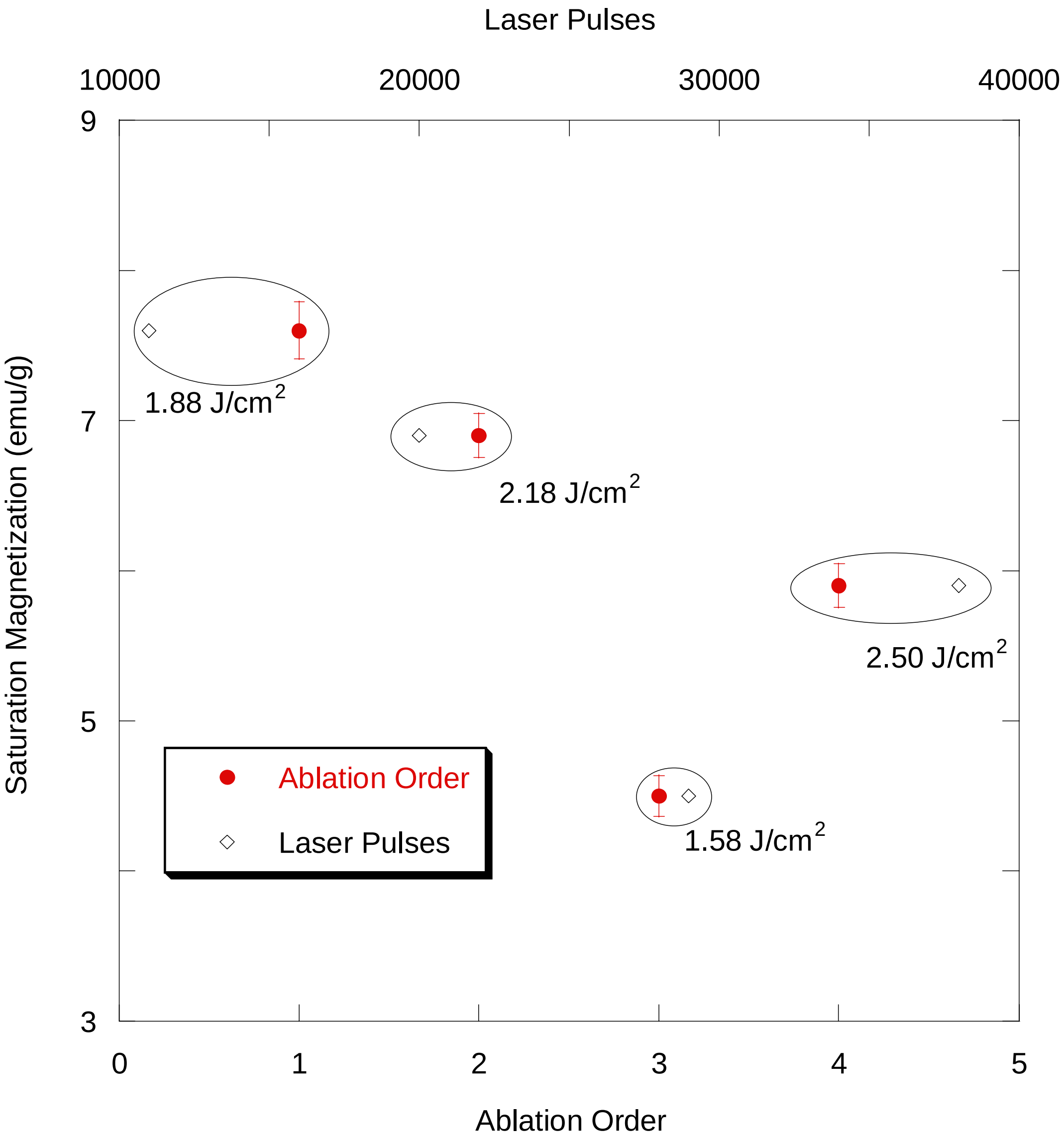

Figure 5.17: Influence of the chronological order of sample production and number of laser pulses in the FPA process on the saturation magnetization of films.

This figure shows that the M_s correlates well with the chronological order in which the samples were deposited. In other words, there is a general decrease in M_s as a function of the number of shots. The exception is the sample made with a fluence of 1.56 J/cm^2 which was explained previously.

To investigate the cause of this phenomenon, target microstructure and modification by laser ablation was studied. Figure 5.18 shows SEM images of a) an unablated region of the $Tb_{0.3}Dy_{0.7}Fe_{1.92}$ target and b) a region after ~ 10,000 laser pulses at 1.88 J/cm^2.

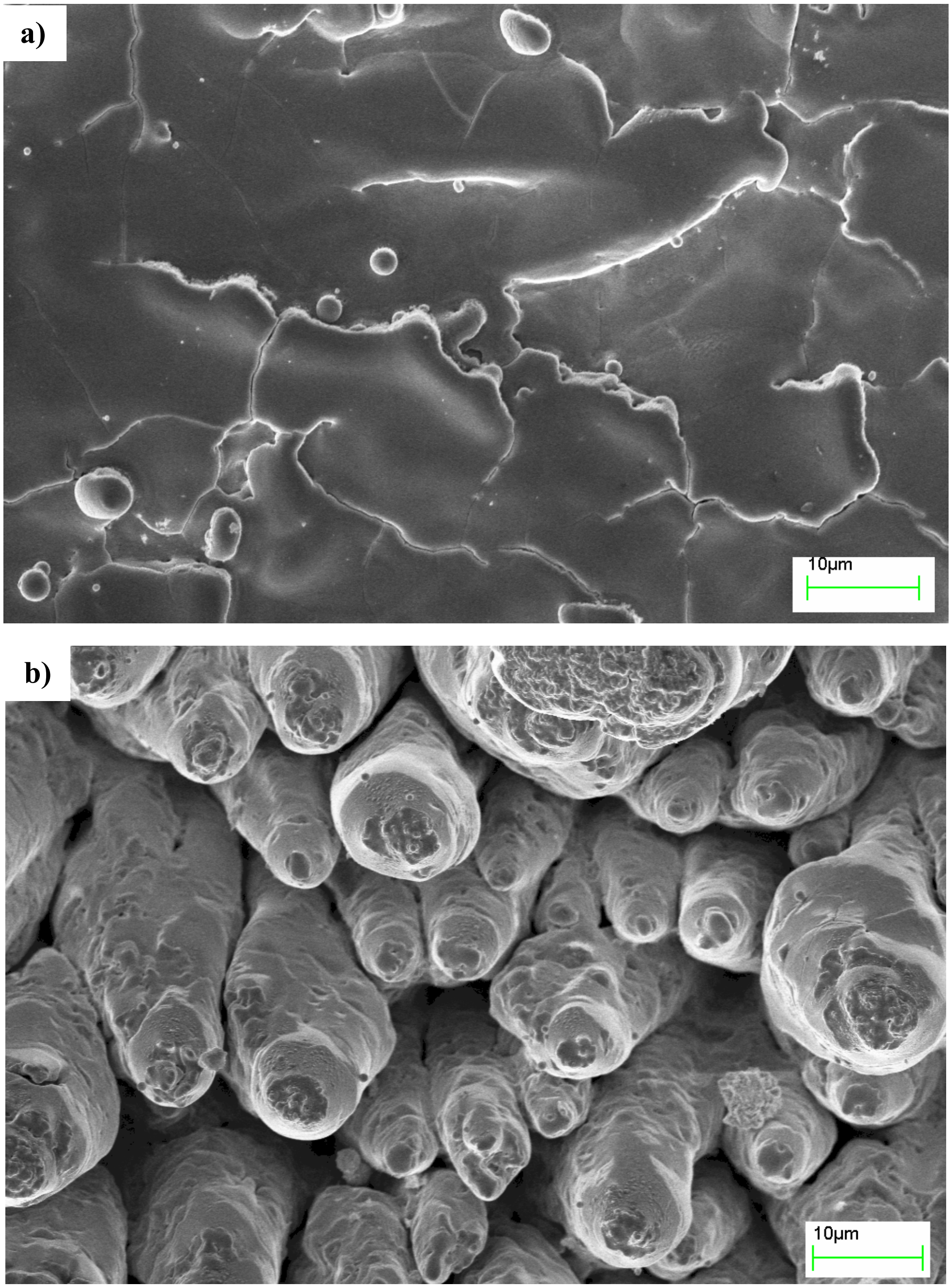

Figure 5.18: SEM micrographs of $Tb_{0.3}Dy_{0.7}Fe_{1.92}$ solid target: a) before ablation and b) after 10,000 laser pulses.

The unablated surface is fairly smooth whereas, after ~ 10,000 laser shots, a hole has been dug into the target at the focal spot and columnar-type structures are apparent. The columns point in the direction of the incoming laser. The hole and columnar structures alter the absorption dynamics, plume expansion and laser fluence which all can lead to phase segregation.[16, 42] Since the laser focal spot was not moved for the samples measured, our results show that the surface condition of the target is a more dominate factor in determining nanoparticle and film properties than laser fluence for films produced above the breakdown threshold.

5.5 Particle Composition

With the target condition being such a significant factor in film properties, further analysis was done using the TEM to analyze composition. SEM EDS presented earlier showed that the composition of the film was not significantly different from the starting material. However, the area probed by the SEM is large and therefore is not sensitive to micron scale variations in composition. To probe smaller areas, the x-rays emitted from nanoparticles in the TEM were analyzed. The electron beam was reduced in size to 10 – 50 nm to probe small regions. A small condenser aperture (20 µm) was used to reduce the intensity of the electron beam and prevent particle alteration. Figure 5.19 shows a TEM image of nanoparticles made by FPA.

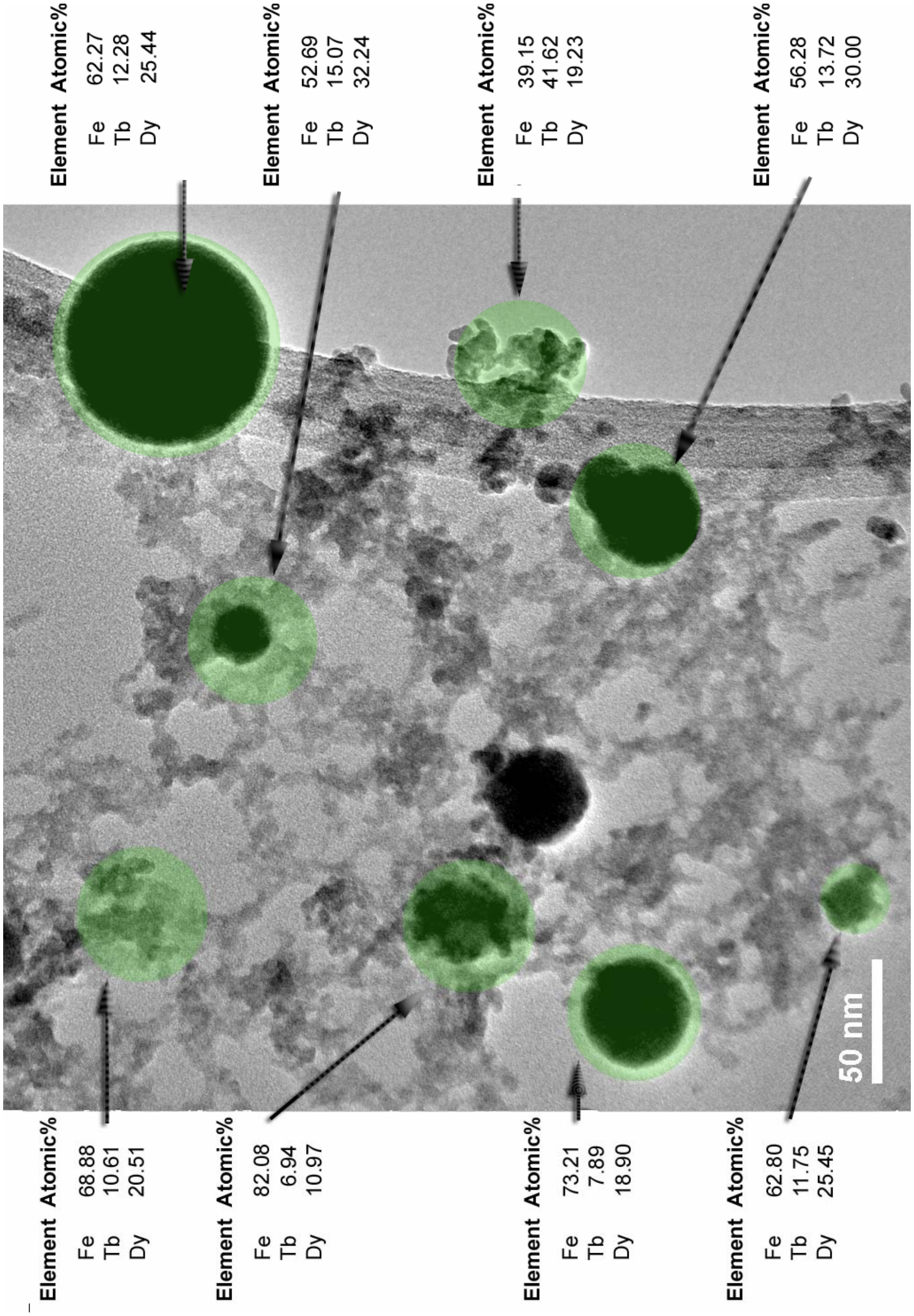

Figure 5.19: TEM image of nanoparticles made by FPA. Circles indicate area where EDS spectra were taken.

The circles highlight areas that were probed using the nanoarea EDS. Quantification of each EDS spectrum showed that the Fe, Tb and Dy are segregated. Some areas (thus nanoparticles) are very Fe rich, while others have an excess of rare earth elements, still others had the composition of the starting material. Segregation is detrimental to the TbDyFe system because experimental results by Clark et al. have shown that the magnetostriction is greatly reduced with Fe rich or rare earth rich compositions (see Figure 1.3). In addition, the anisotropy compensation is greatest at $Tb_{0.3}Dy_{0.7}Fe_{1.92}$ and thus the fields required to saturate increase with other compositions.[2]

5.6 Conclusions

Nanostructured primarily amorphous $Tb_{0.3}Dy_{0.7}Fe_{1.92}$ films were made at various fluences from 1.56 – 2.5 J/cm^2. It was found that the condition of the target had a greater effect on particles and film properties than laser fluence. The FPA films had a reduced M_s that was ~ 1/10 of the starting material. Although SEM EDS showed that the stoichiometry of the starting material was preserved, TEM nanoarea EDS revealed that the Fe, Tb and Dy had become segregated at the nano-scale in the FPA process. The composition is very important for $Tb_{0.3}Dy_{0.7}Fe_{1.92}$ because magnetostriction is greatly reduced with either rare earth rich or iron rich compositions.[43] The segregation from particle to particle is due to several factors, 1) extended, non-uniform plume expansion, 2) target surface modification and 3) segregation by repeated laser ionization. Although FPA is capable of making nanostructured thick films quickly, it is difficult to make multi-component films that require homogeneous mixing using this method.

Chapter 6

Laser Ablation of Microparticles: Results and Discussion

6.1 Introduction

The laser ablation of microparticles (LAM) process was investigated as a means to produce magnetostrictive thick patterned films. In this method, microparticles were aerosolized in an inert gas and then ablated using a KrF laser. This is in contrast to the PLD and FPA techniques where a solid target was vaporized by an intense laser pulse. This chapter presents the results of the influence of carrier gas, *in-situ* annealing temperature and post-process reduction-sintering temperature on LAM produced films of $Tb_{0.3}Dy_{0.7}Fe_{1.92}$.

6.2 LAM Processing

Table 6.1 shows the processing parameters used for LAM. The target material was $Tb_{0.3}Dy_{0.7}Fe_{1.92}$ microparticles. Microparticles were aerosolized and fed into the ablation cell (AC) using helium or argon gas. The inner flow rate which contains the microparticles was set at 157.7 sccm so that each microparticle was ablated once with the KrF laser operating at the maximum repetition rate, 200 Hz. The outer flow was set at 4343 sccm so that the linear velocity of the inner and outer flows was equal, keeping the inner flow laminar through the ablation region. Ablation took place in the ablation cell, where the laser irradiated the microparticles. This resulted in breakdown on the particle surface which in turn resulted in a shock wave that vaporized the microparticle. The vaporized material coalesced into nanoparticles in the low pressure region behind the shock wave. The nanoparticles were then accelerated through a supersonic nozzle by the pressure differential between the ablation chamber and deposition chamber (C1) and then impacted to produce films on alumina substrates using a motorized x-y stage.

Target…………………………………………………………	$Tb_{0.3}\ Dy_{0.7}\ Fe_{1.92}$
Laser…………………………………………………………	KrF
Laser Wavelength……………………………………………	248 nm
Laser Pulse Length…………………………………………...	12 ns
Laser Pulse Rate……………………………………………...	10 Hz
Laser Fluence………………………………………………...	$> 2\ J/cm^2$
Horncell Base Pressure………………………………………	2×10^{-7} Torr
Horncell Processing Pressure………………………………..	760 Torr
Carrier Gas…………………………………………………..	Ar & He (99.999%)
Gas Flow Rate (outer)…………………………………….	157.7 sccm
Gas Flow Rate (inner)…………………………………….	4343 sccm
Deposition Nozzle Size………………………………………	250 µm
C1 Pressure During Depositon……………………………….	0.15 – 0.20 Torr
Substrate……………………………………………………...	Al_2O_3
Substrate Temperature………………………………………	300 – 320 K
Nozzle to Substrate Distance…………………………….....	2 mm

Table 6.1: Processing conditions for particles and films made by LAM.

Since $Tb_{0.3}Dy_{0.7}Fe_{1.92}$ is a brittle intermetallic, it can be milled or ground to make smaller particles. Microparticles for LAM were made by two methods. 1) 0-300 μm sized powder (Etrema, Ames, IA) was purchased. Tungsten carbide milling media was then used to ball-mill the powder for 24 hours in a polyethylene bottle to further reduce the particle size. Figure 6.1 shows a micrograph of ball milled powder. The particles are non-spherical and lateral dimensions ranged from 0.1-10.0 μm with an aspect ratio < 2.5. 2) Solid rods were ground using a mortar and pestle. Figure 6.2 shows a micrograph of particles made with this technique. The resulting particles have a broader size distribution than those produced by ball milling with lateral dimensions from 0.1 to 75 μm. In addition, the aspect ratio of the particles is much larger than powders made by ball milling.

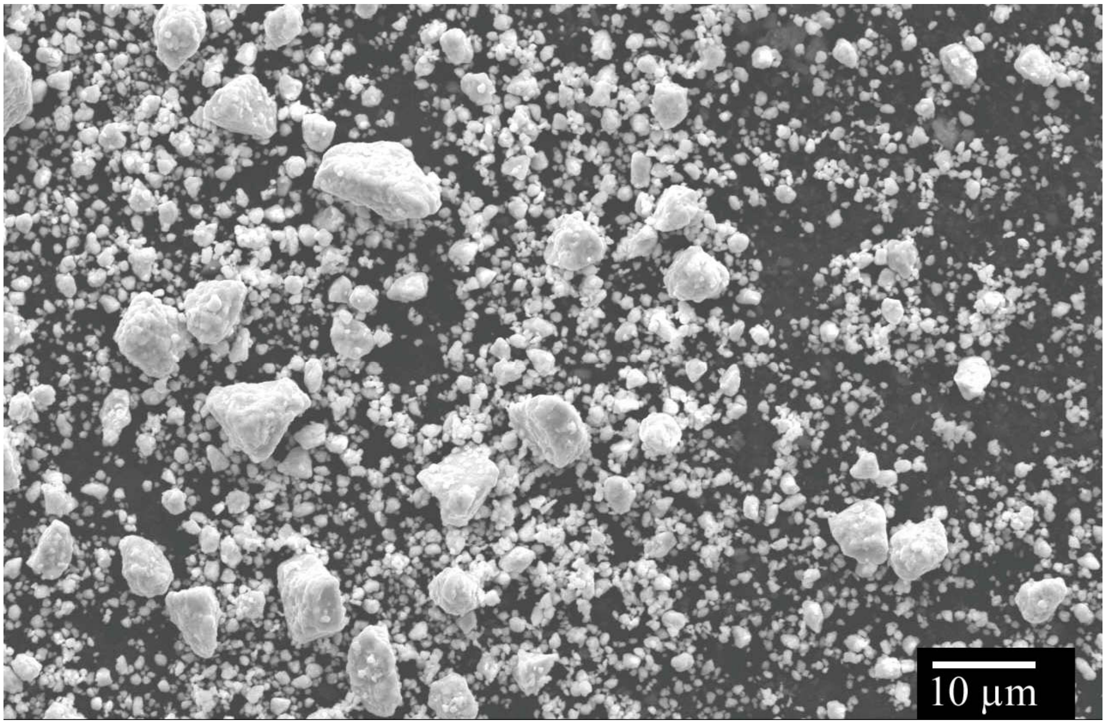

Figure 6.1: SEM micrograph of $Tb_{0.3}Dy_{0.7}Fe_{1.92}$ microparticles after 24 hours of ball milling.

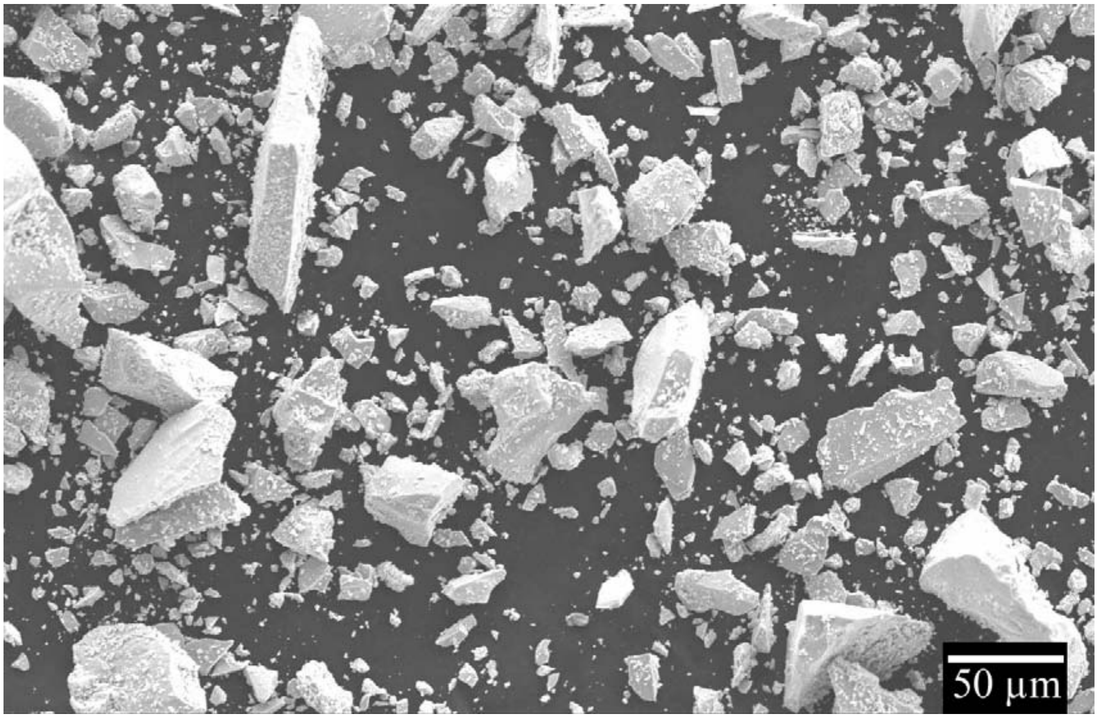

Figure 6.2: SEM micrograph of $Tb_{0.3}Dy_{0.7}Fe_{1.92}$ microparticles after grinding using a mortar and pestle.

The advantage of using powders made by mortar and pestle is that the powder can be ground just before ablation, thus reducing the degree of oxidation of the starting material. Both methods were performed in an argon (99.999%) gas-filled glovebox. SEM EDS confirms that the atomic ratios of the elements are approximately that specified ($Tb_{0.3}Dy_{0.7}Fe_{1.92}$) by Etrema. Figure 6.3 shows the powder XRD. All diffraction peaks correspond to the cubic laves phase Fe_2R.

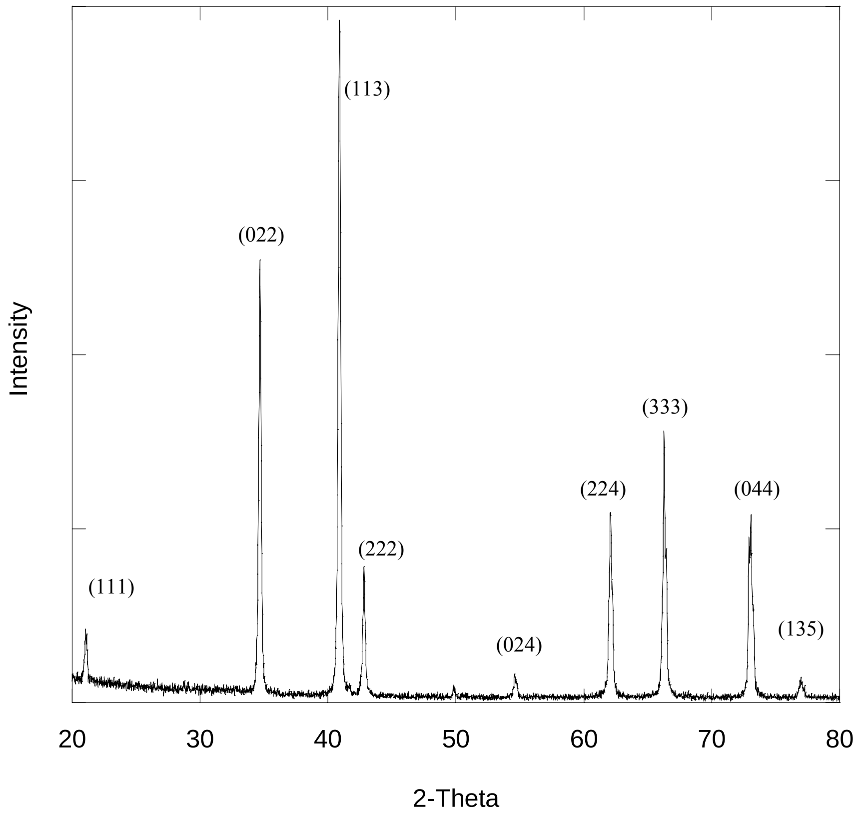

Figure 6.3: XRD of $Tb_{0.3}Dy_{0.7}Fe_{1.92}$ powder ground using mortar and pestle.

In the LAM process, spheres with narrow size distribution are the ideal target material for uniform breakdown and shockwave propagation. Thus, microparticles made by ball milling were a closer approximation to ideal spheres than powders made by mortar and pestle. However, early magnetic results on nanostructured films made with ball milled powder showed very poor magnetization. Investigation of the LAM process using OES showed that there was oxygen in system during ablation which resulted in oxidation of the particles and poor magnetization. Figure 6.4 shows the OES spectra for the original setup showing the presence of oxygen in the ablation process. Multiple changes were made in an all-encompassing effort to reduce or eliminate the source or sources of oxygen. 1) The carrier gas was changed from 99.995% to 99.999% purity. 2) The ablation chamber was leak checked, baked and pumped down to 2×10^{-7} Torr prior to all experiments. 3) The starting material was changed to powders ground by mortar and pestle. Grinding was performed 30 min prior to film deposition. An OES spectrum for the modified setup is shown in Figure 6.5. The spectrum shows a reduction in both the 778 nm and 845 nm emission peaks of oxygen, confirming that the modified setup succeeded in reducing the oxygen present in the system. This spectrum is typical of all the specimens presented in the rest of the chapter.

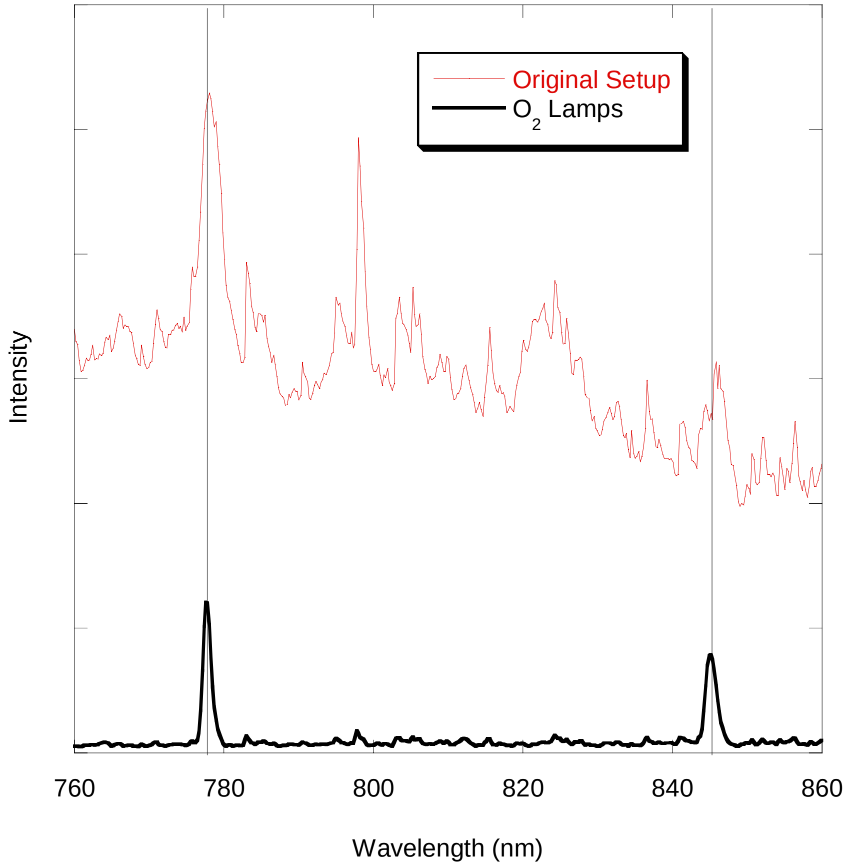

Figure 6.4: OES of early experiments.

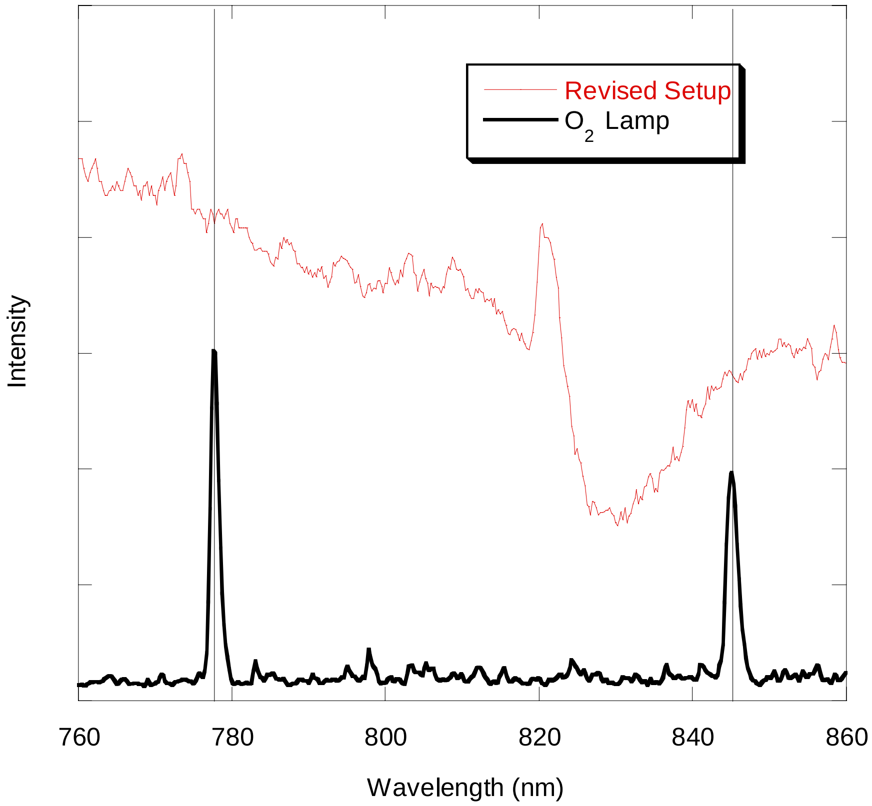

Figure 6.5: OES of revised setup.

6.3 Nanoparticle Structure and Composition

TEM grids of nanoparticles by LAM were made by increasing the nozzle-to-substrate distance to 6 mm to prevent blowout of the lacey carbon TEM grid and to reduce the density of nanoparticles deposited. Particles were made using argon and helium carrier gases to investigate the effects of gas type on nanoparticle size. Figure 6.6 shows TEM micrographs of particles made using LAM in argon and Figure 6.7 displays the distribution of particle size measured for the nanoparticles ablated in argon gas.

Figure 6.7 shows TEM micrographs and Figure 6.8 displays the histogram for LAM particles made in helium gas.

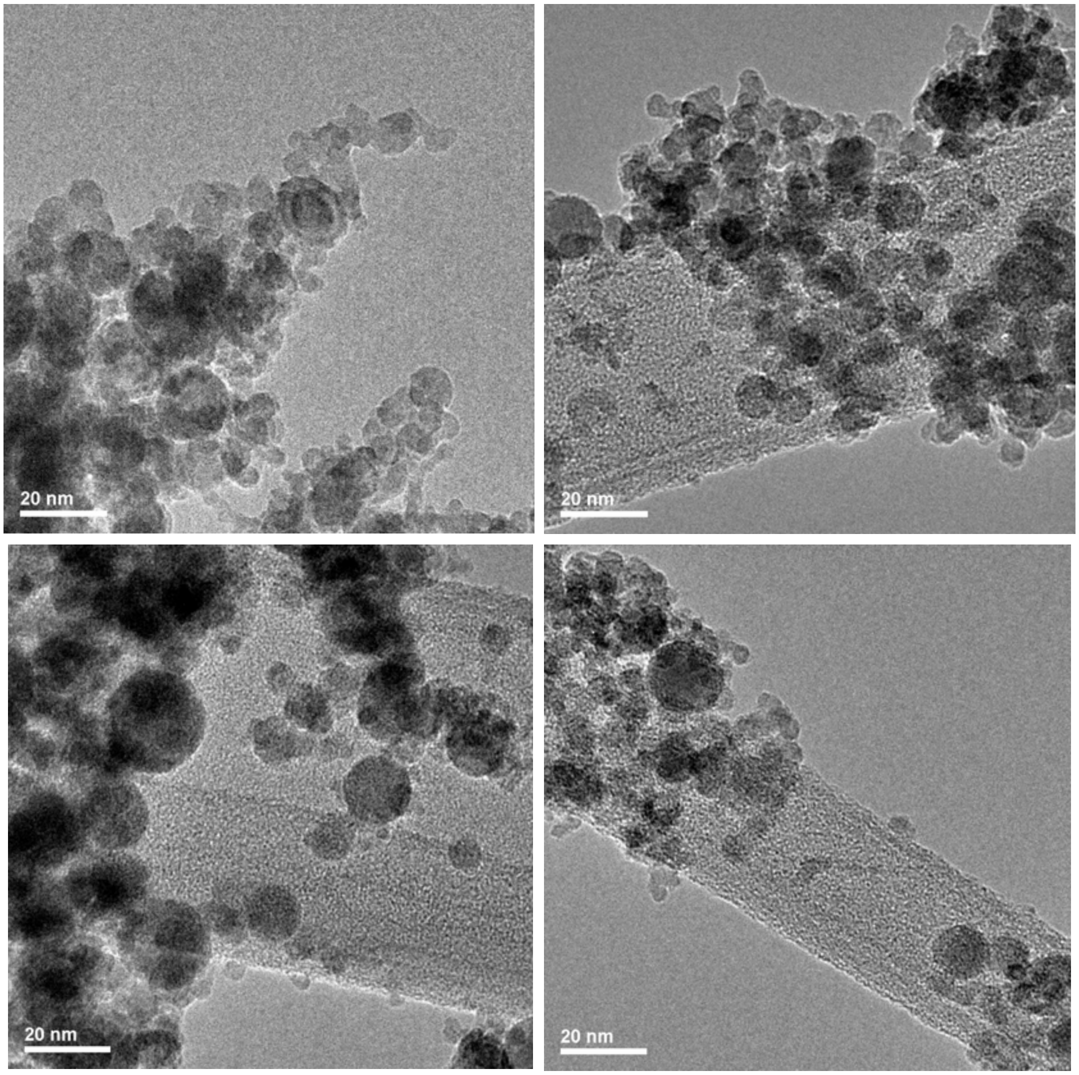

Figure 6.6: TEM images of LAM created nanoparticles in argon gas.

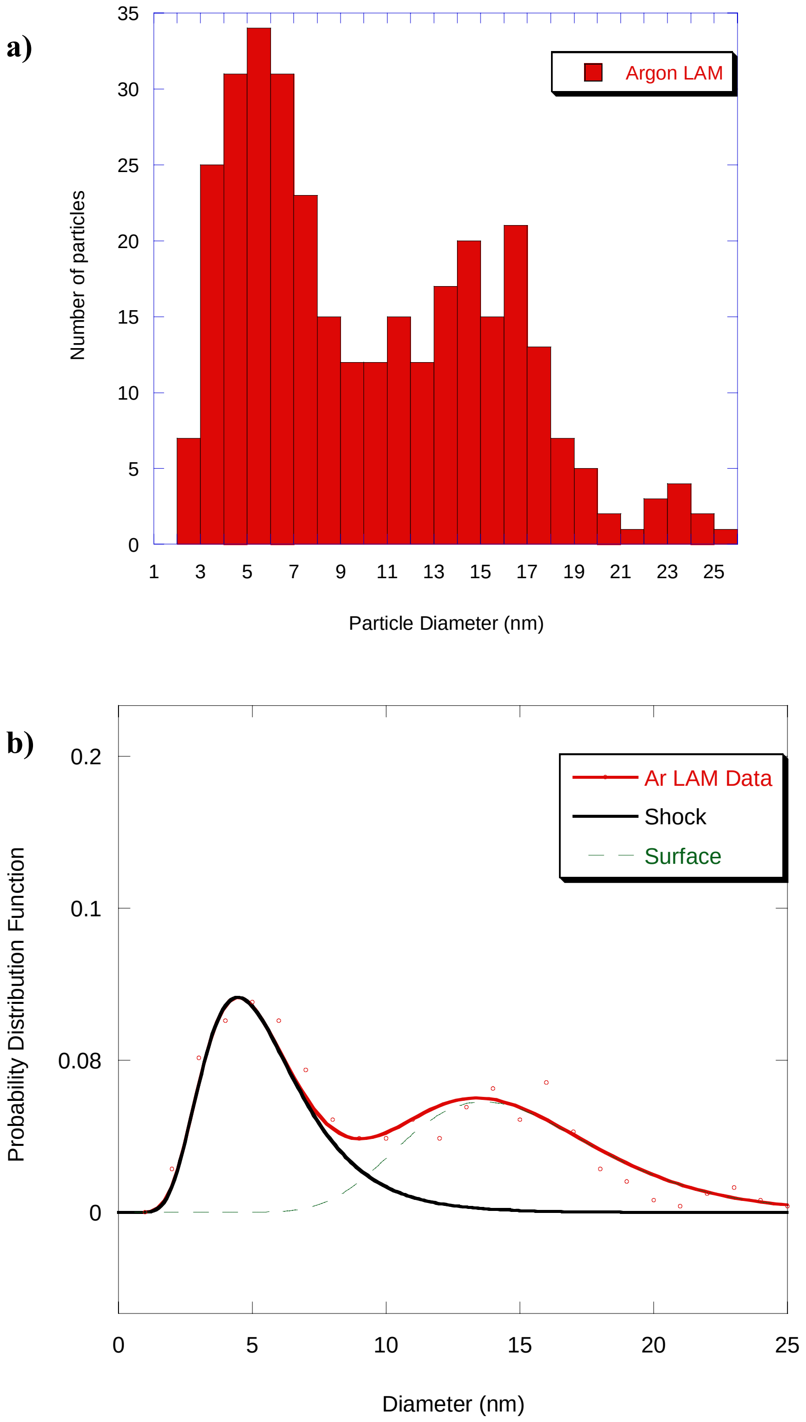

Figure 6.7: Size distribution and probability distribution for nanoparticles produced by LAM in argon.

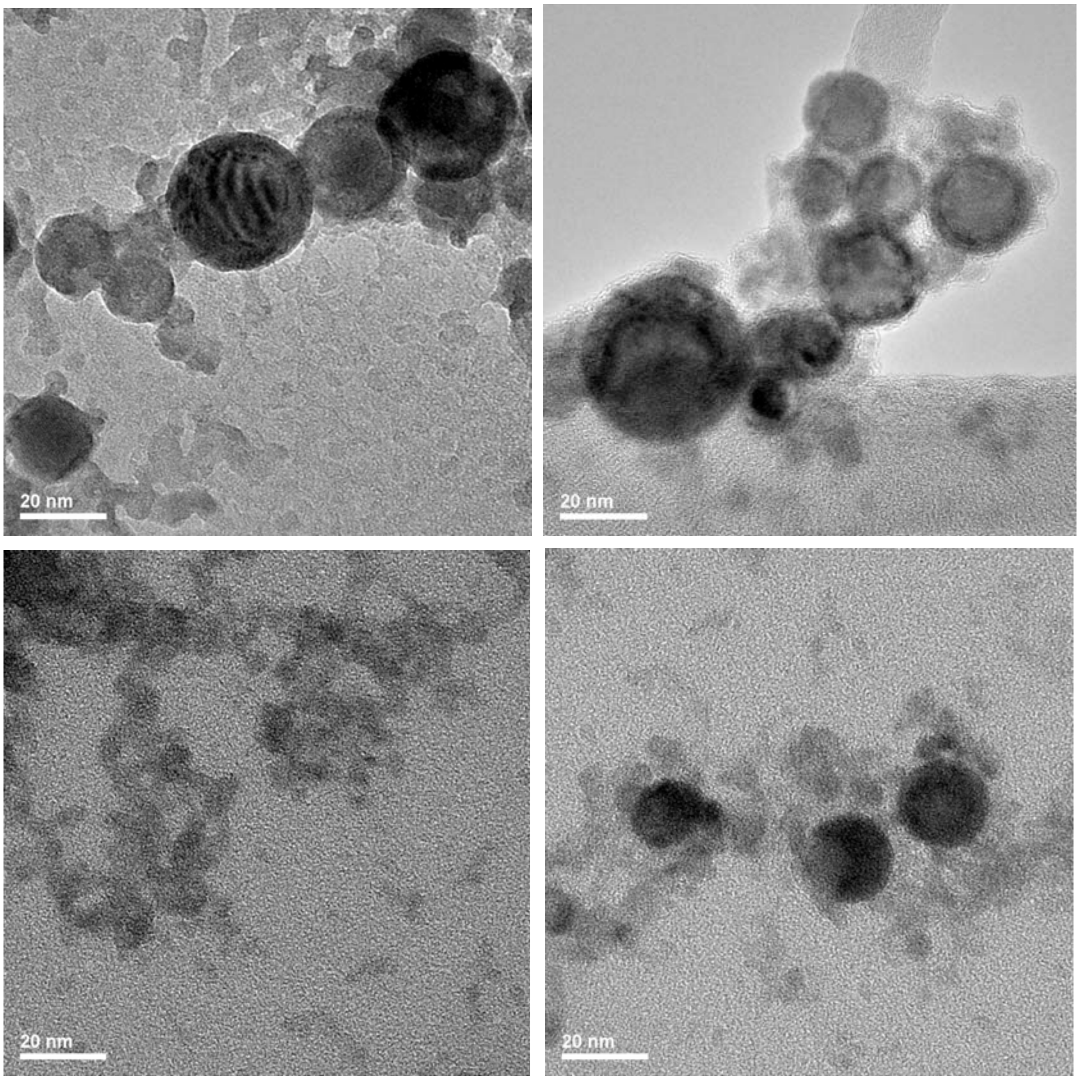

Figure 6.8: TEM image of LAM created nanoparticles in helium gas

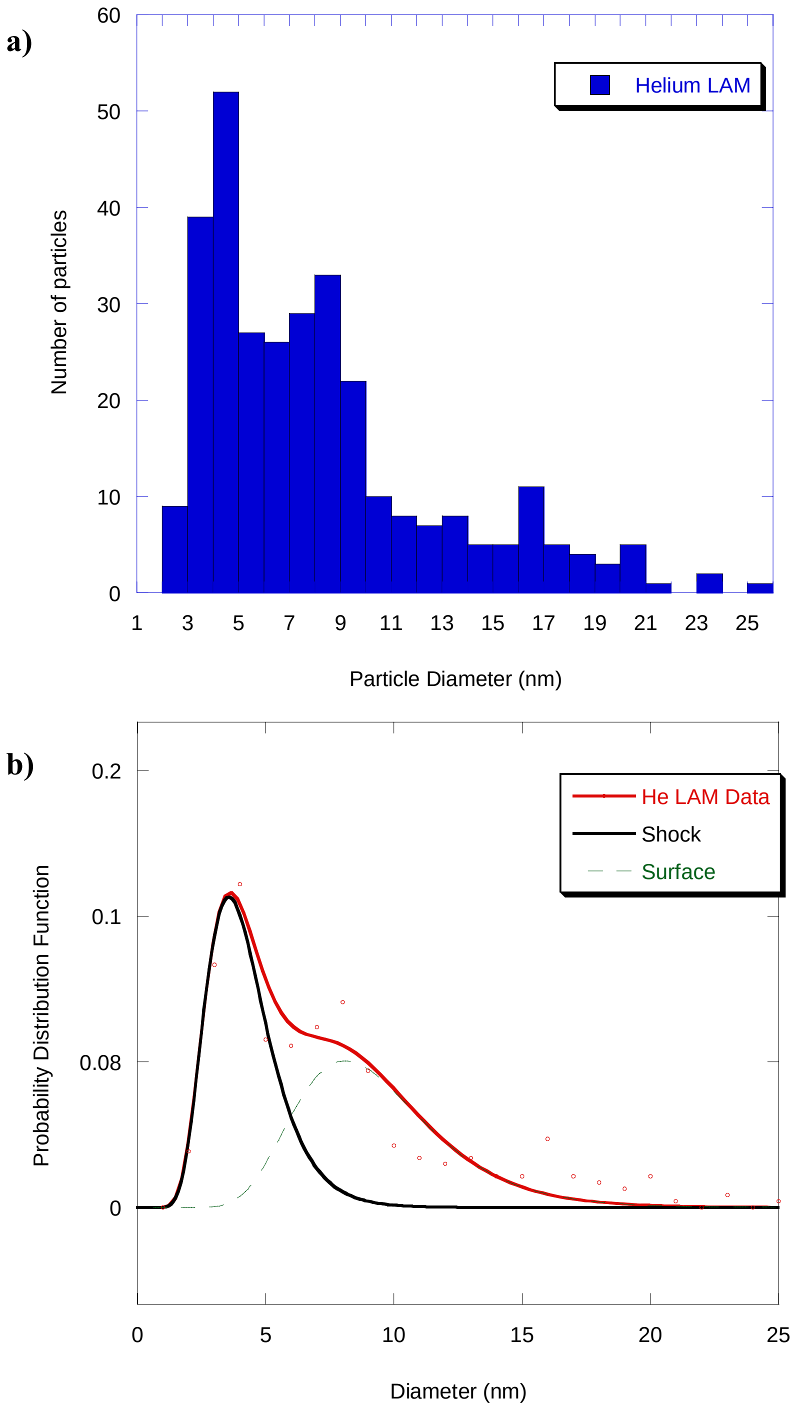

Figure 6.9: Size distribution and probability distribution for nanoparticles produced by LAM in helium.

Nanoparticles produced using LAM in argon have a mean size of 10.2 nm and a relatively broad size distribution (stdev = 5.4). Particles fabricated in helium have a mean size of 8.2 nm and a narrower size distribution (stdev = 4.7). The average sizes are similar to previous work on silver nanoparticles produced using LAM. However, the particles here have a broader distribution. Nichols et al. attributed the larger particles (>10 nm) to surface evaporation on the microparticle before breakdown conditions were reached.[26] Since the starting powder, $Tb_{0.3}Dy_{0.7}Fe_{1.92}$ ground using mortar and pestle, used in this study had a broad size distribution and irregular shape, our results are consistent with Nichols findings that suggest this should result in a broader size distribution with more large nanoparticles. Using a bimodal lognormal distribution, LAM nanoparticles made in argon show a mean particle size of 5.6 nm for the shock mode (stdev = 2.3) and a mean particle size of 15.1 nm for the surface evaporation mode (stdev = 4.0). Compared to LAM in Ar, the particles fabricated by LAM in helium, as expected, had a smaller mean and narrower distribution from the shock mode (mean = 4.2 nm, stdev = 1.43) as well as from the surface mode (mean = 9.4 nm, stdev = 3.0).

Figure 6.10 is a high resolution TEM image of particles made by LAM in helium.

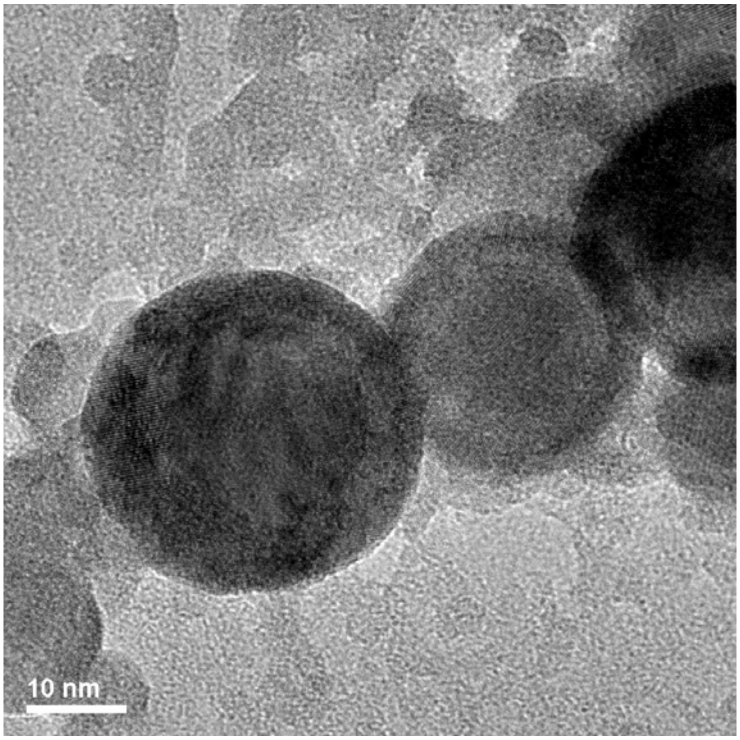

Figure 6.10: High resolution TEM images of LAM particles made in helium.

Lattice fringes are clearly visible in the large particles (>10 nm) indicating that they are crystalline. In addition, there appears to be a core-shell structure which will be discussed later. TEM diffraction and image FFT were also used to verify particle crystallinity. Particles in the smaller distribution sizes (< 10 nm) are amorphous. No diffraction is observed in the smaller particles and bright field images of these particles show no diffraction contrast.

TEM composition studies were performed using EDS for particles made in argon and helium gas. Figure 6.11 shows a typical EDS spectrum. The average TEM EDS spectra using a beam diameter of ~ 60 nm show that the average composition of nanoparticles for samples produced in both gases is similar to the original composition of the starting powder.

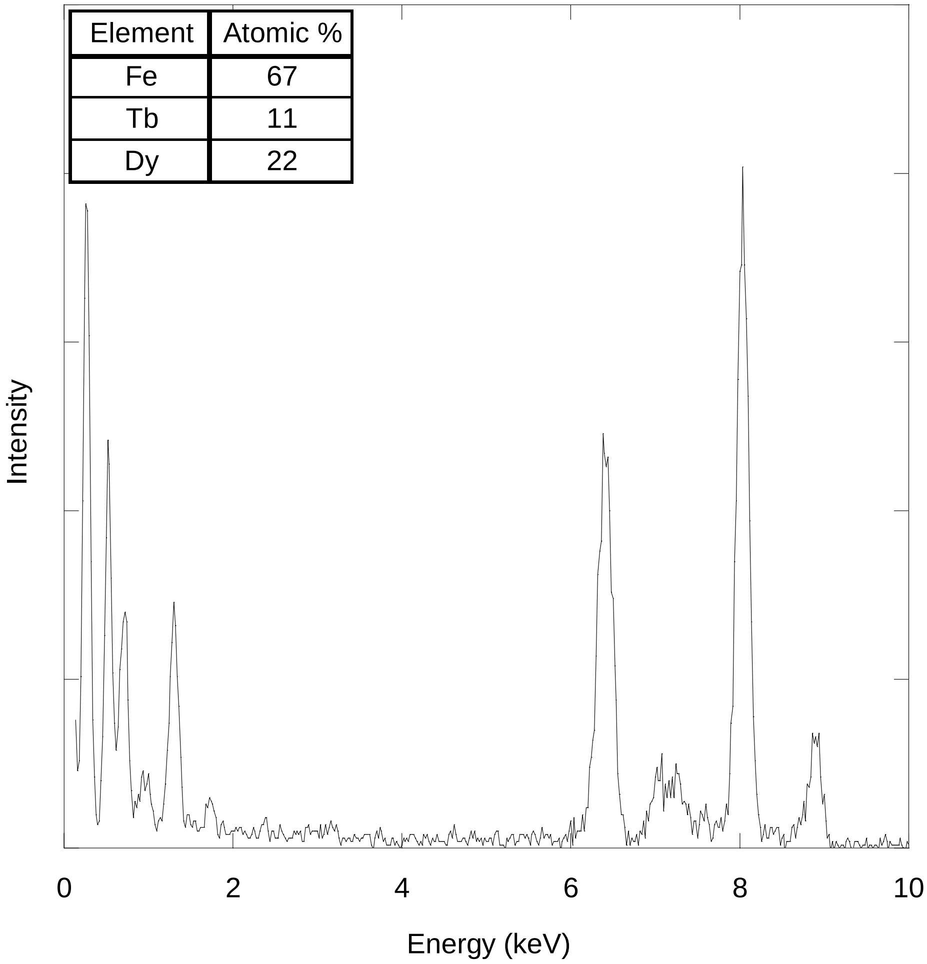

Element	Atomic %
Fe	67
Tb	11
Dy	22

Figure 6.11: Large area TEM EDS of LAM nanoparticles.

6.4 Film Structure

Thick films of nanoparticles produced using LAM in Ar and He were jet-deposited on alumina substrates. Calculations performed previously show that 5 nm particles can be accelerated to 1000 m/s in helium and to 370 m/s in argon using a 250 μm diameter flat-plate-nozzle.[23] Thus particles made with helium should have substantially higher impaction energies. Previous studies on silver films showed that

LAM films deposited with helium have a relative density of 65–75 % of bulk and films deposited with argon have a relative density of 55-65 % of bulk. Figure 6.12 a) and b) are SEM cross-section images of LAM films made using argon and helium gas. Figure 6.13 shows a plan view SEM image of a helium deposited film.

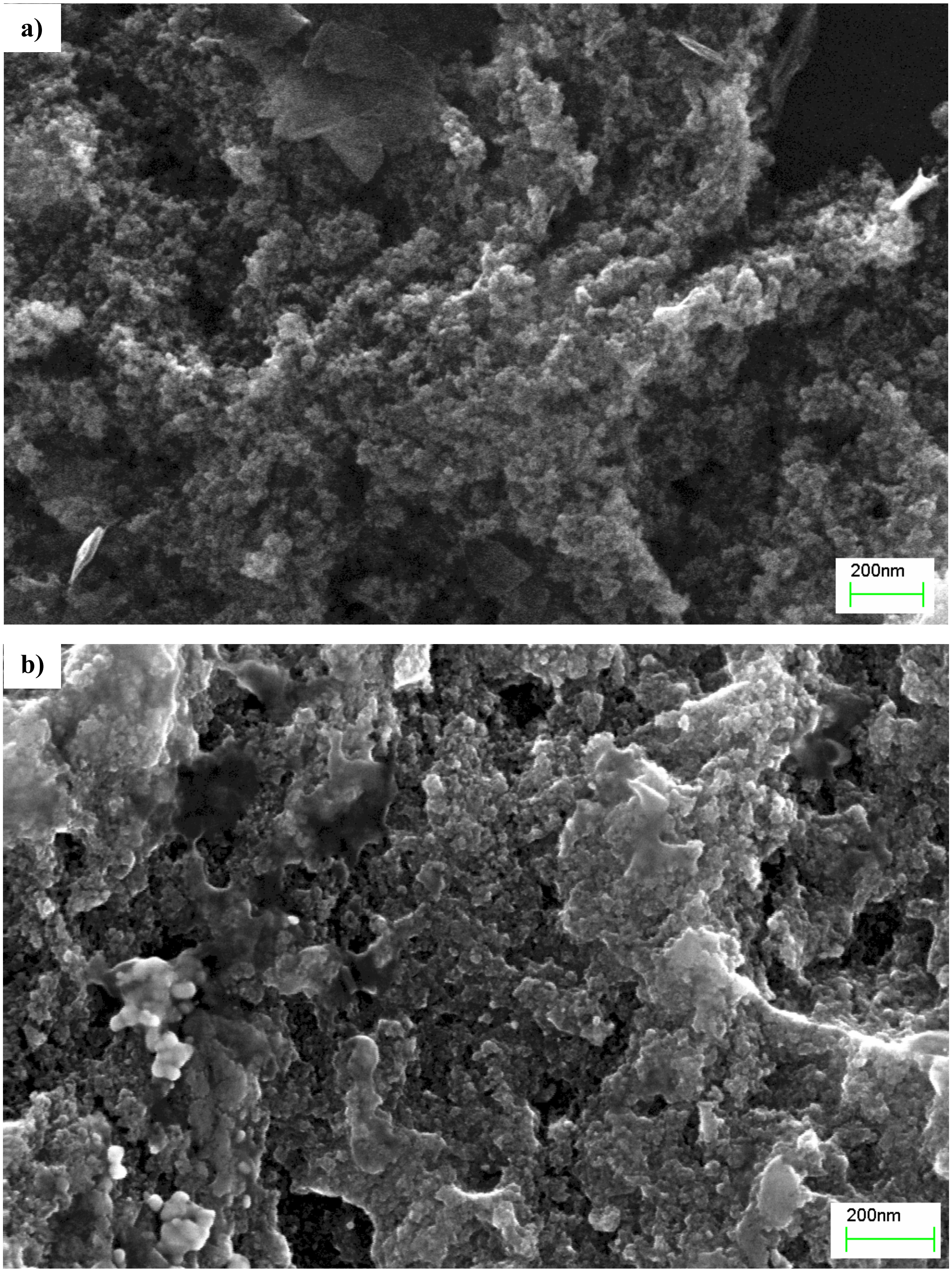

Figure 6.12: Cross-sectional SEM micrographs of nanostructured films made using LAM in a) argon and b) helium.

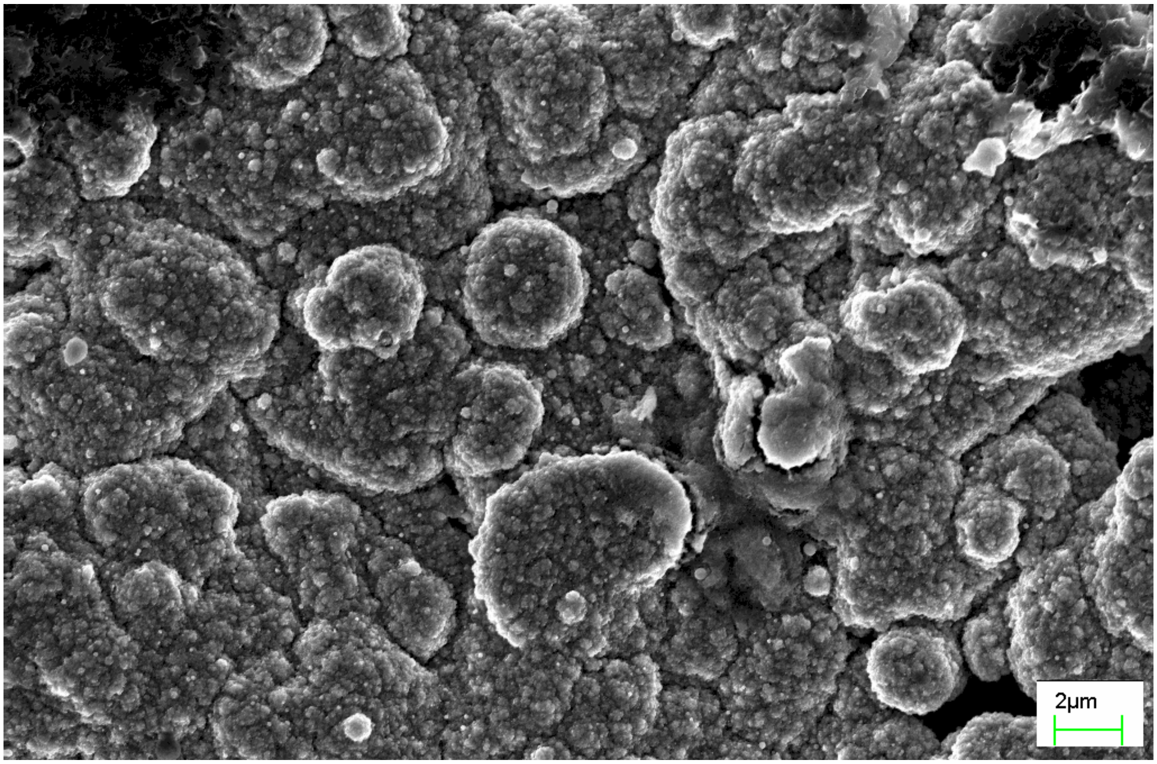

Figure 6.13: Plan view SEM micrograph of nanostructured film made by LAM in helium.

Cross-sectional images of $Tb_{0.3}Dy_{0.7}Fe_{1.92}$ films show that films made with helium as the carrier gas are visually denser than films made with argon. Low magnification, plan view SEM images show that there are micron sized agglomerates of nanoparticles.

Figure 6.14 shows a typical SEM EDS spectrum for LAM produced films using argon and helium. Compositional studies by SEM EDS verify the large area TEM EDS results which showed that the composition of the original microparticles is preserved in the films.

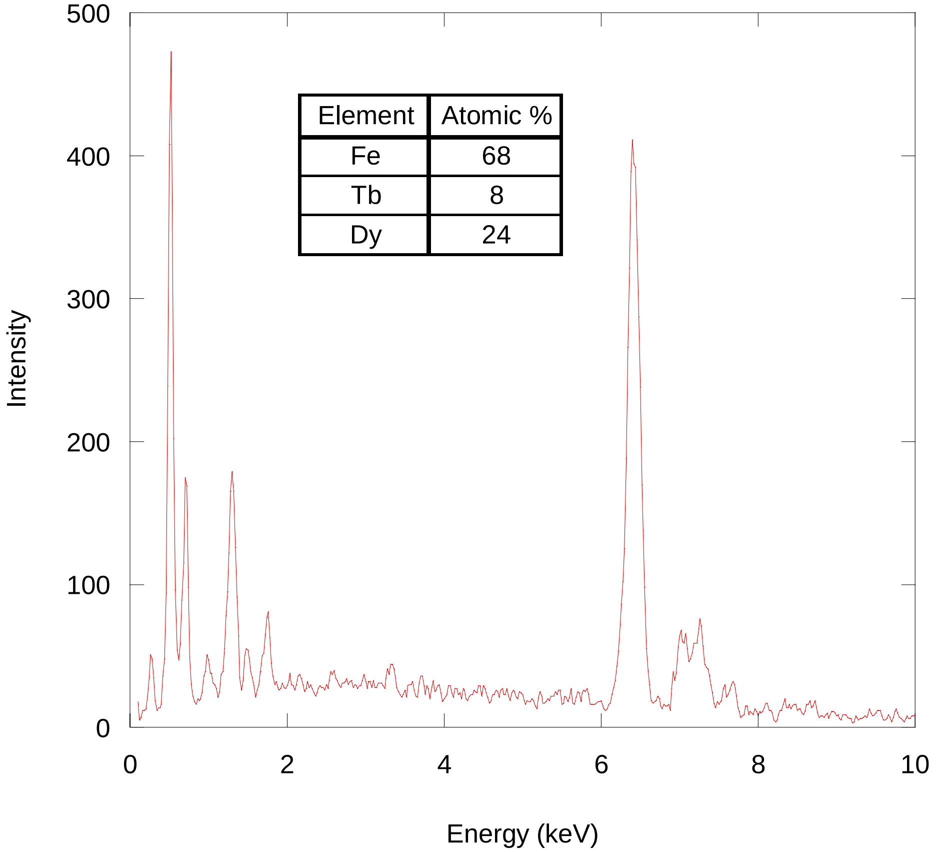

Element	Atomic %
Fe	68
Tb	8
Dy	24

Figure 6.14: SEM EDS spectrum typical of films produced using LAM.

XRD spectra for thick films produced using LAM in argon and helium are displayed in Figure 6.15. All visible peaks in the spectra correspond to the alumina substrate. This indicates that most of the film consists of amorphous $Tb_{0.3}Dy_{0.7}Fe_{1.92}$.

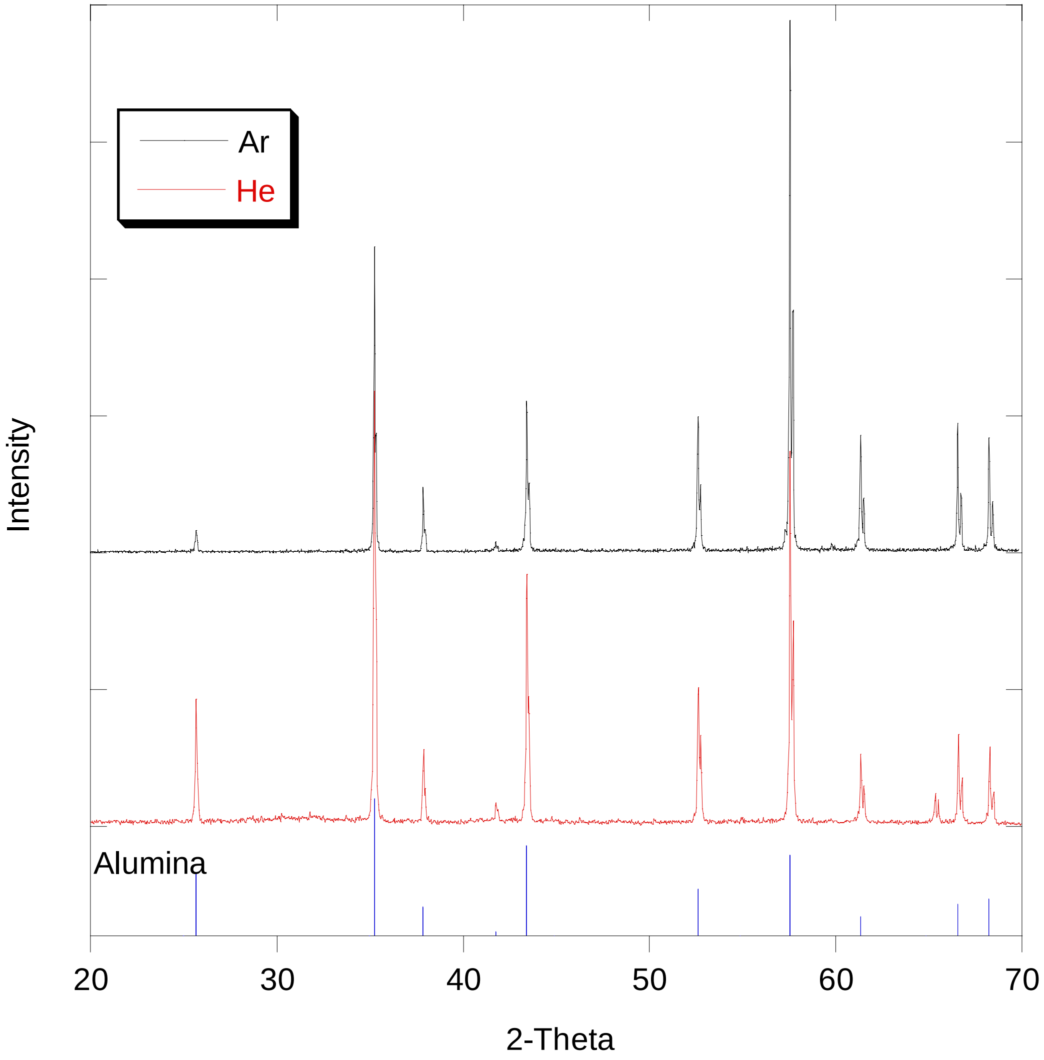

Figure 6.15: XRD of thick films made by LAM in argon and helium.

6.5 Magnetic Properties

The Figures 6.16 and 6.17 show hysteresis loops for LAM produced films made in argon and helium. Both films were exposed to air after deposition and thus have a reduced magnetization as compared to bulk due to some surface oxidation. LAM films produced in helium exhibit a slightly larger M_s than the films made in argon, 13.8 emu/g versus 11.5 emu/g. The coercivities of the films are 59 Oe for films produced using argon and 41 Oe for films produced in helium.

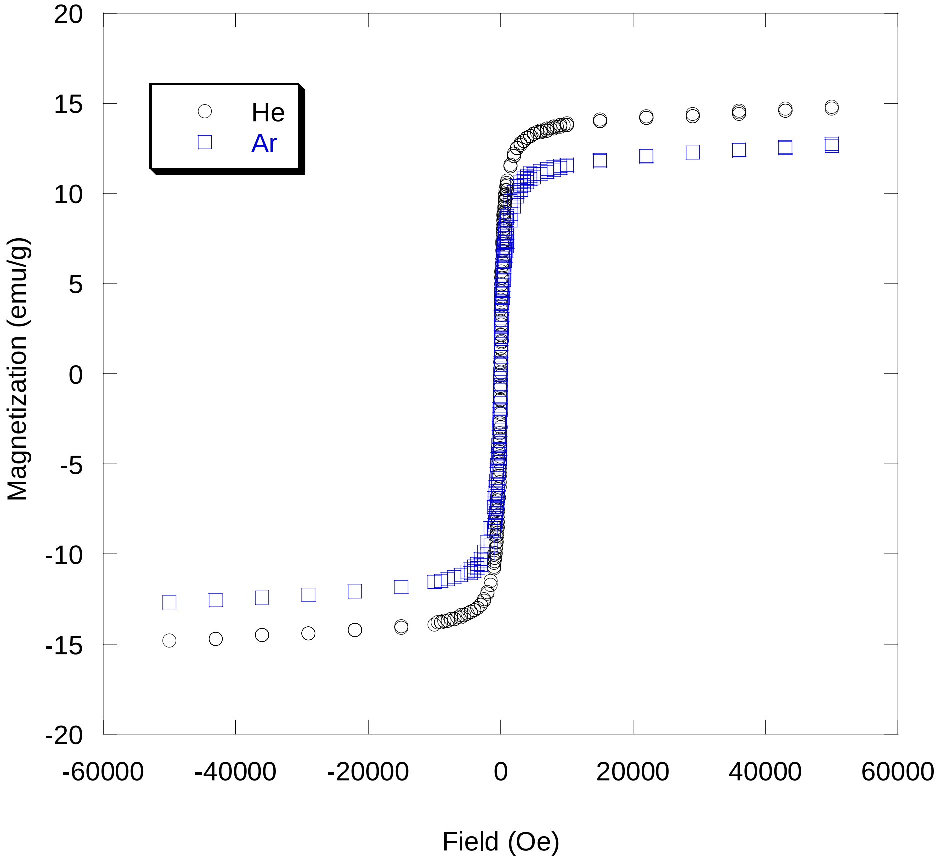

Figure 6.16: Hysteresis loops for LAM films made in argon and helium gas.

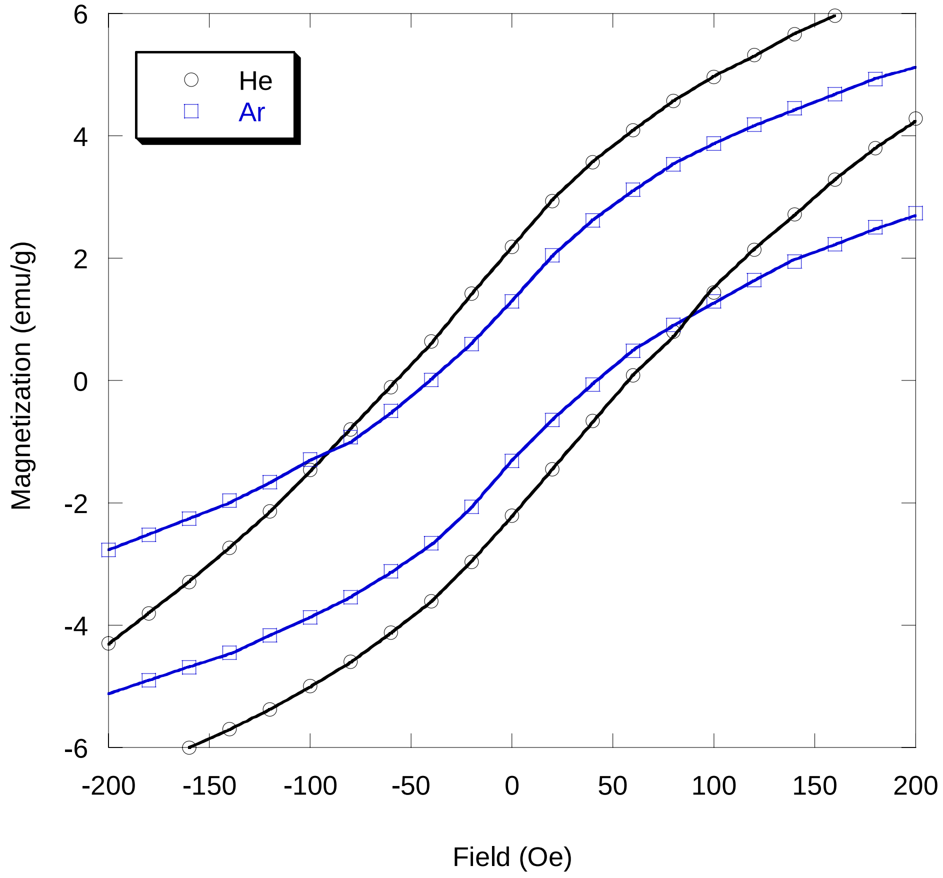

Figure 6.17: Low field region of hysteresis loops for LAM films made in argon and helium gas.

The magnetostriction results for films produced in argon and helium are consistent with expected results. For example, films produced in argon are should have a larger M_s due to the larger particles sizes which results in less surface area available for oxidation when the films are exposed to air. However, the argon produced LAM films are also less dense that the helium produced films and thus contain more open porosity. The increased porosity results in greater surface area for oxidation than that for the more dense helium produced LAM films. The lower coercivity and higher magnetization for helium produced LAM films over argon produce LAM films further supports this conclusion.

Comparing our results for LAM produced films with our PLD films and films produced by others; the M_s is lower which is likely due to some oxidation that results from open porosity in the LAM produced films.

6.6 The Effect of *In-situ* Annealing of LAM Films

6.6.1 Introduction to *In-situ* Annealing

Deposition and *in-situ* annealing of the films in vacuum without exposure to air was attempted in an effort to sinter the films. This would have the advantage of closing pores, thus preventing oxidation of the films. In addition, higher density films would also result in a greater Youngs modulus which is advantageous for magnetostrictive actuators.

Studies on amorphous, $Tb_{0.3}Dy_{0.7}Fe_{1.92}$, thin films show that if the substrates are heated during deposition or the films are annealed after deposition, then there is an increase in both magnetostriction and magnetization due to increases in homogeneity of the elements in the film at low temperatures and crystallization of the Fe_2R laves phase at higher temperatures.[44-49] Crystallization temperatures for amorphous films have been reported to be from 425˚ to 600˚C, depending on fabrication technique, composition and whether the films were annealed or the substrate was heated during deposition.

For our *in-situ* annealing study, the films were produced using the same LAM conditions presented earlier. The nanoparticles were jet deposited from atmosphere to ~200 mTorr in C1. The substrate used was 127 µm thick alumina. Helium gas was used in the LAM process to make smaller, more uniform size distribution of nanoparticles and to have a higher initial film density.

After deposition, the chambers were pumped to < 5×10^{-8} Torr and the film was transferred to the heating stage in C2 with a magnetic sample manipulator. Annealing occurred under vacuum that ranged from $2\text{-}8\times10^{-8}$ Torr. Annealing temperatures were varied from 300˚-700˚C and the hold time for each sample at the target temperature was 1 hr. Heating rates were manually controlled and the heating coil response was nonlinear; thus, there was some variation from sample to sample. The heating rate was approximately 50˚ C/min for up to 400˚C but was reduced to approximately 25˚ C/min for temperatures greater than 400˚C to prevent failure of the heater.

6.6.2 Structure of Films Annealed *In-situ*

Figure 6.18 shows a typical profilometry scan from an *in-situ* annealed film. Average thickness of the films ranged from 4 - 10 µm.

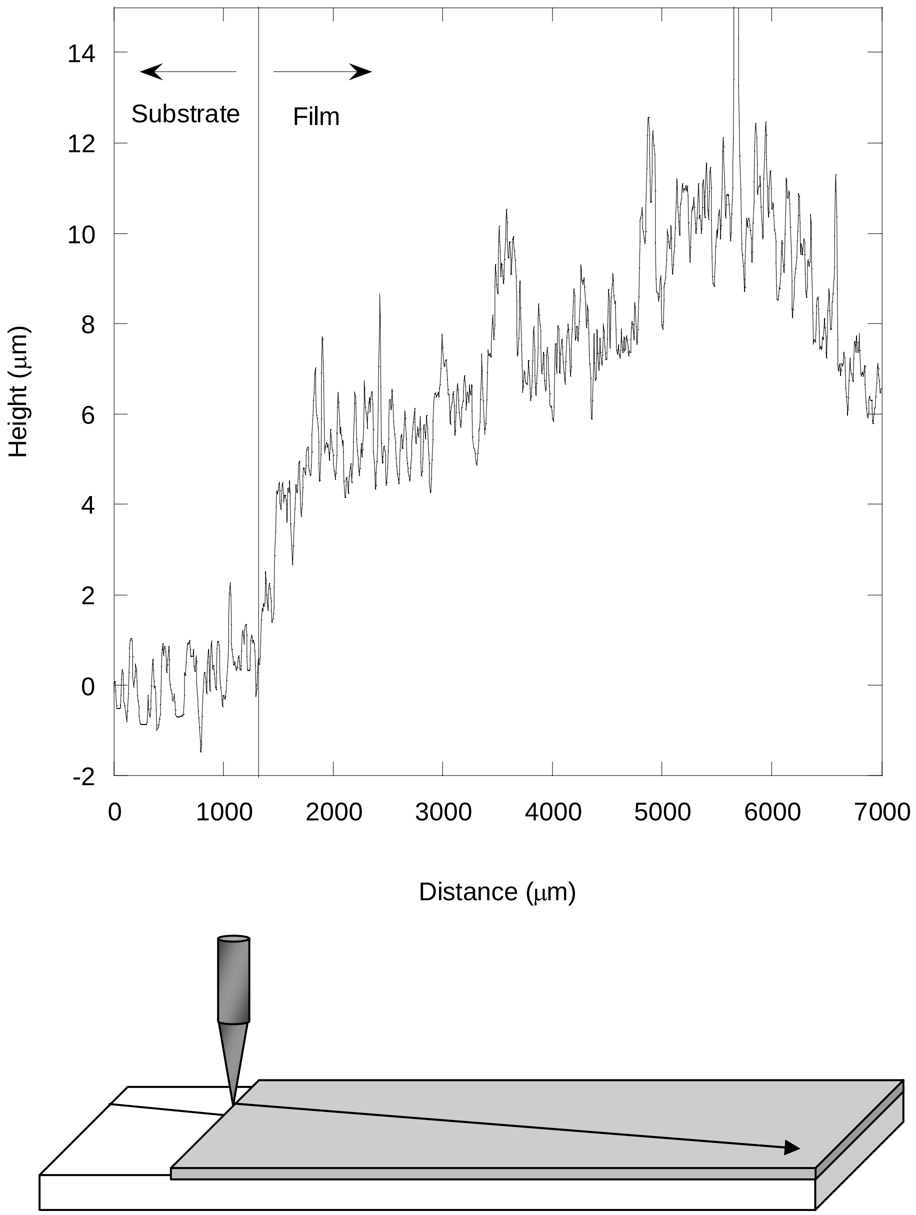

Figure 6.18: A typical profile from films annealed *in-situ*.

Figure 6.19 is a stacked view of the XRD spectra from films annealed *in-situ*. Variations in the intensity of the alumina peaks are due to differences in film thicknesses.

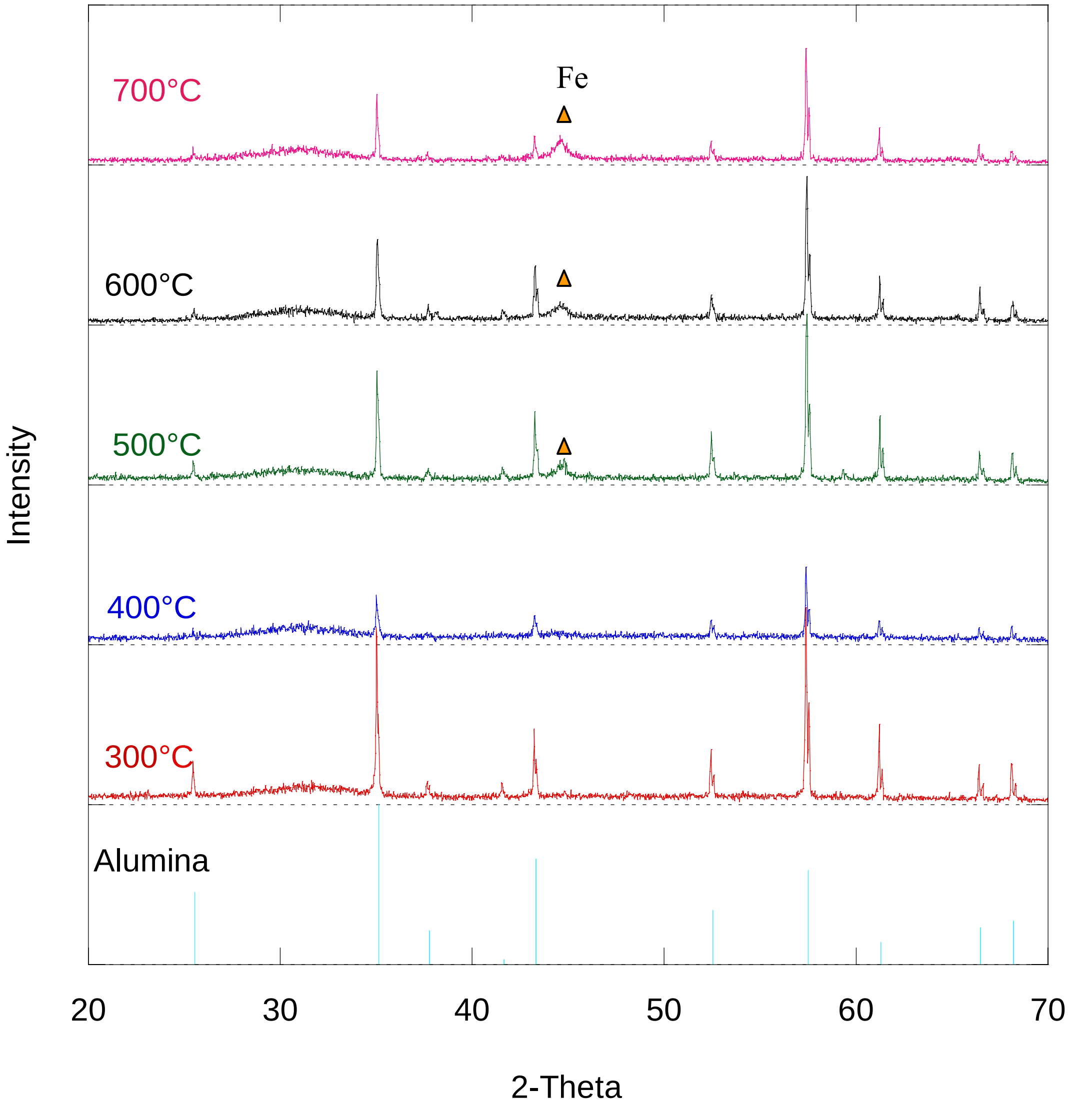

Figure 6.19: XRD spectra of LAM films annealed *in-situ*.

The spectra show no change from the as-deposited condition films up to an annealing temperature of 400˚C. For films annealed at 500˚C, a small peak corresponding to α-Fe is visible. From 500˚ - 700˚C there is not much change in the breadth of the Fe (100) peak, which indicates that the size of α-Fe crystallites. The broadness of the peak indicates that the grain size is nanocrystalline and remains nearly constant. Even at annealing temperatures as high as 700˚C, there are no diffraction peaks present that correspond to the Fe_2R laves phase. There is a broad diffuse peak $2\theta = 30˚$-35˚ which likely corresponds to rare earth oxides and/or nitrides (There are several compounds with similar diffraction peaks in this range making it impossible to unambiguously identify which phase or phases are present.).

6.6.3 Magnetic Properties of Films Annealed *In-situ*

Figures 6.20 and 6.21 show the hysteresis curves for the films annealed *in-situ*. Figure 6.23 shows the magnetization at a field = 10,000 Oe and coercivity of the films as a function of annealing temperature.

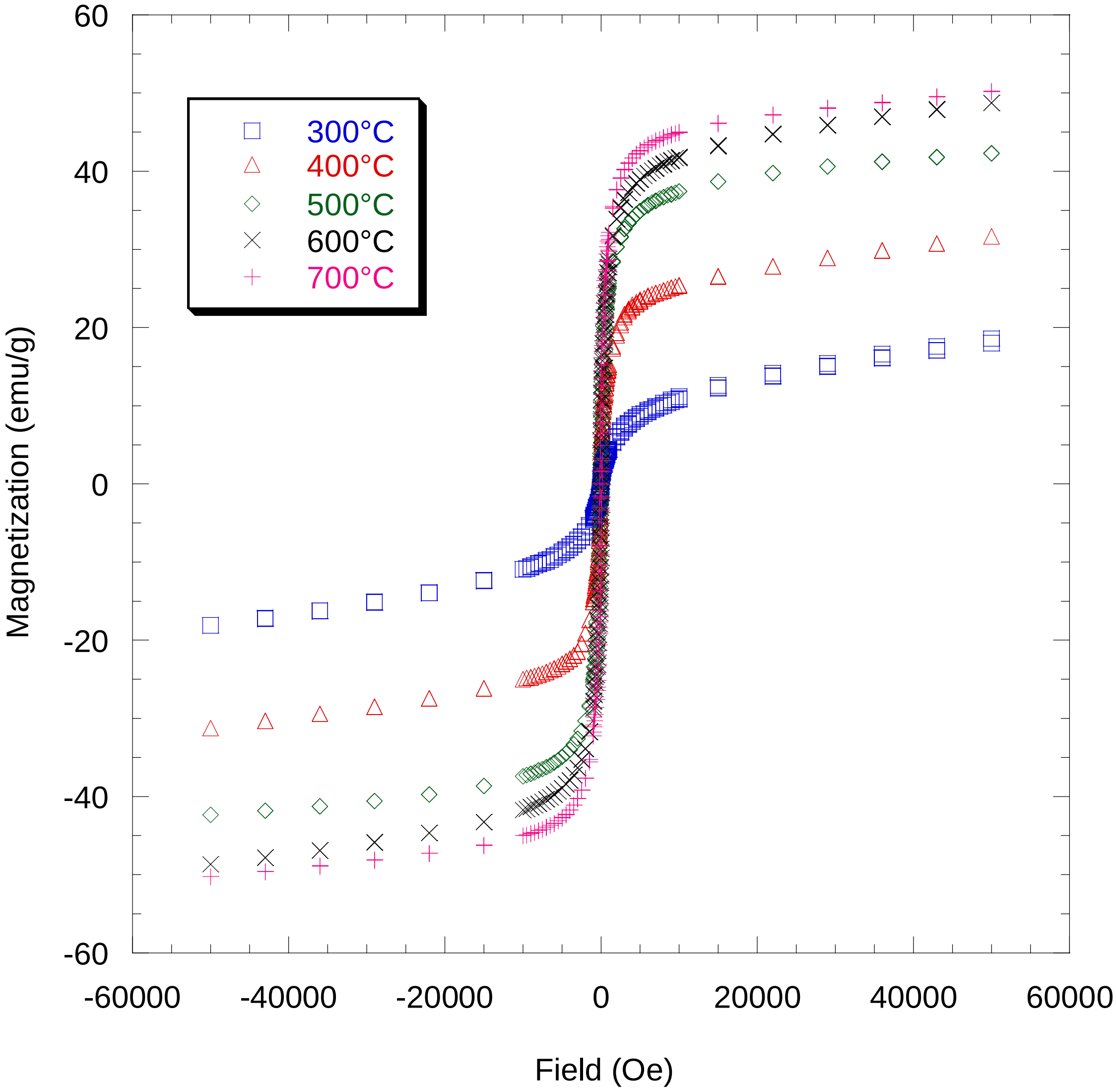

Figure 6.20: Hysteresis curves for LAM films annealed *in-situ*.

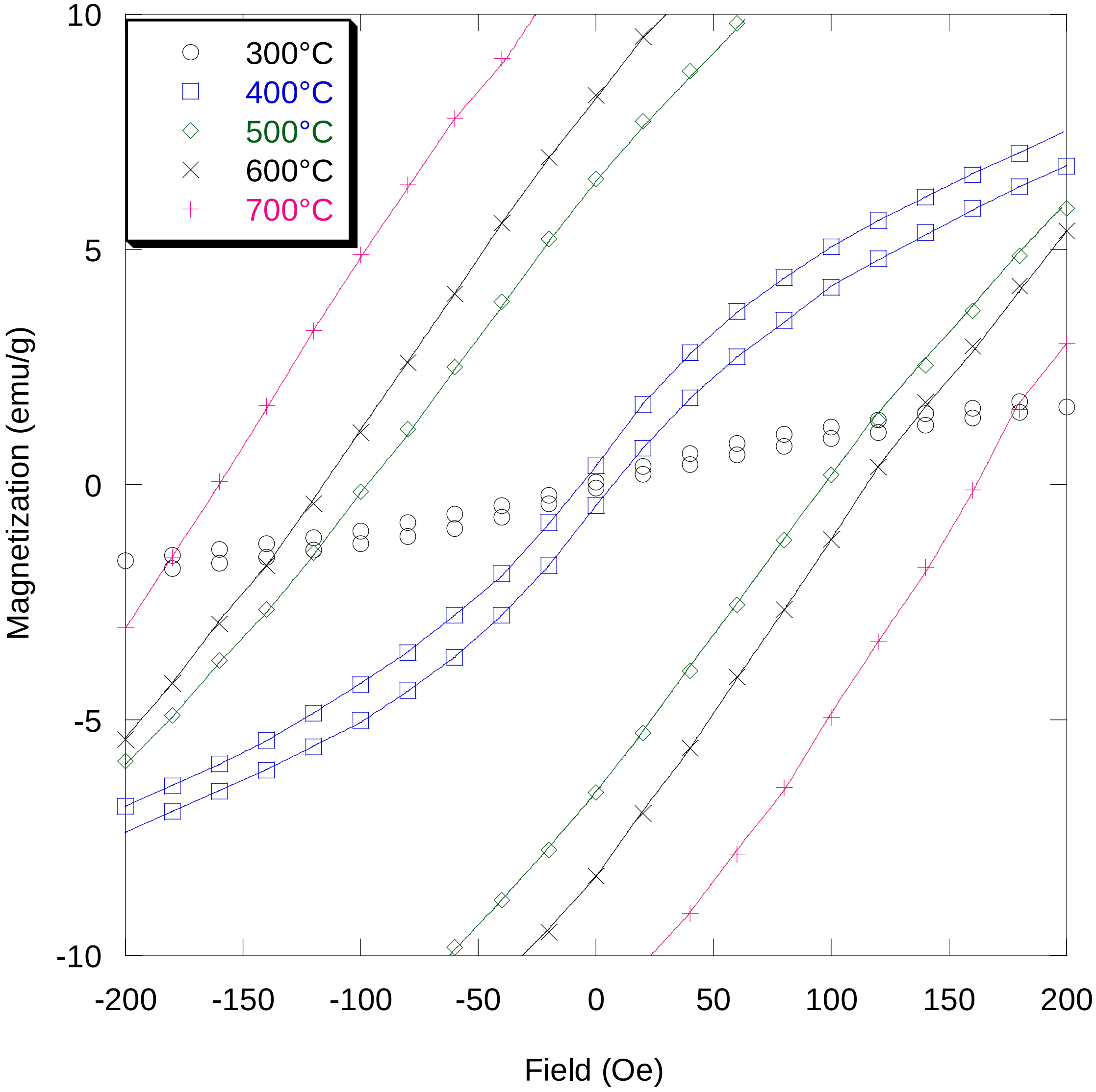

Figure 6.21: Low field hysteresis curves for LAM film annealed *in-situ*.

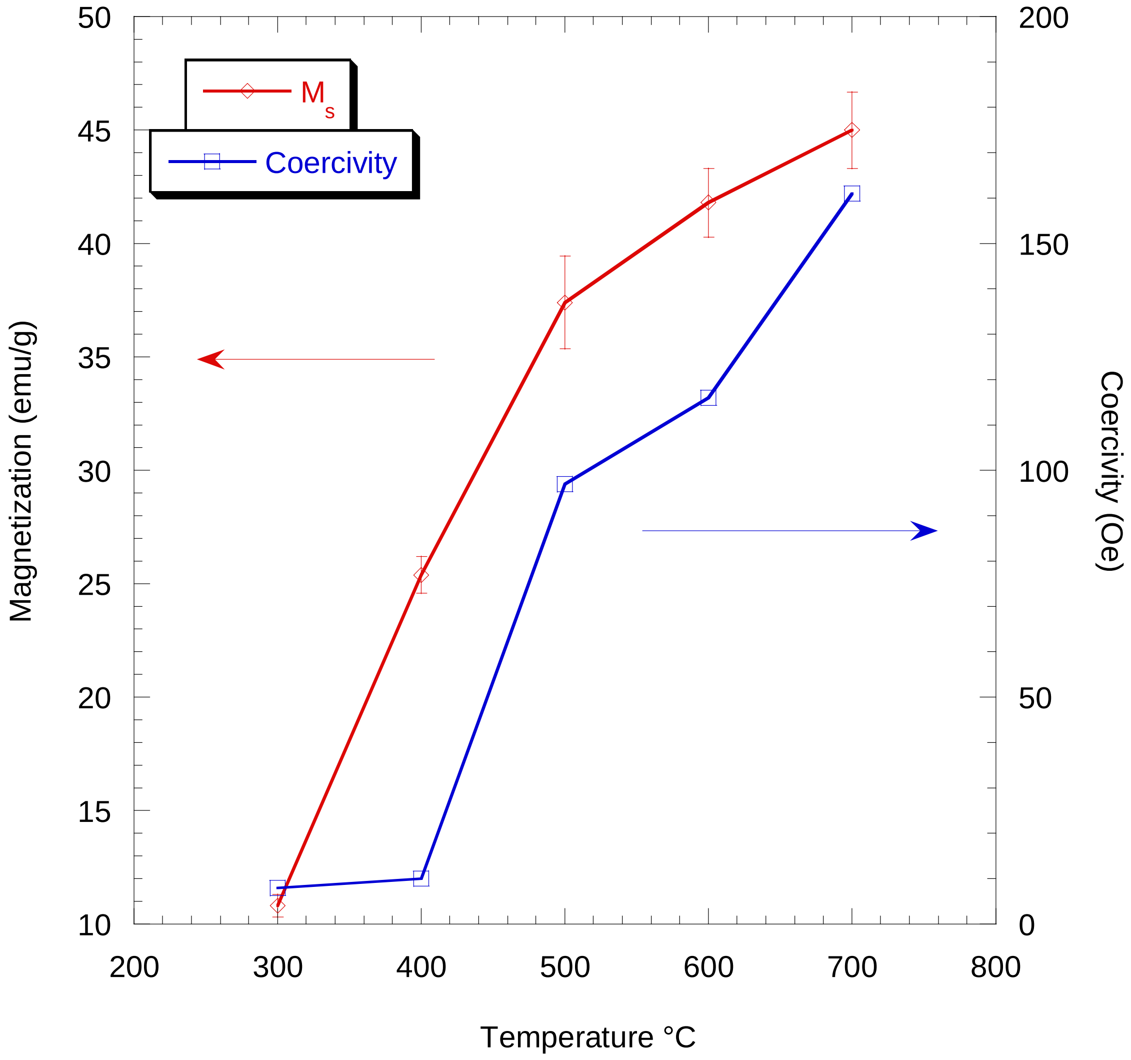

Figure 6.22: Saturation magnetization and coercivity as a function of annealing temperature for films annealed *in-situ*.

The magnetization of film annealed at 300˚C is low due to oxidation that resulted from moisture that was evaporated off of the first stage of the cryopump. The gate valve between the cryopump and the chamber was partially closed to prevent this from occurring for the other films. The magnetization of the films increases as the annealing temperature increases as it does with annealing of amorphous thin films due to formation of small crystallites.[48] From 500˚-700˚C there is only a small additional increase of the M_s. The additional increase is likely due to coarsening of the α-Fe crystallites.

The coercivity of the films does not change much from as deposited films up to 400˚C. Between 400˚ and 500˚C, there is a jump in coercivity of the films that is probably due to nucleation of the α-Fe crystallites. The coercivity of the films continues to increase for temperatures above 500˚C. Herzer et al. have shown that in ferromagnetic alloys, the coercivity increases with particle size when the particles are small.[7] There is a peak in coercivity which then decreases for micron sized particles. This is because when particles/grains are smaller than

$$L_o \sim \sqrt{\frac{A}{K_1}}, \tag{6.1}$$

where A is the exchange stiffness constant and K_1 is the anisotropy constant, the exchange energy balances the anisotropy. Particles/grains below this size are not randomly oriented according to easy direction of each particle/grain but align by exchange interaction.[50] The *in-situ* annealed LAM films produced here observe this trend.

6.6.4 Magnetostriction of *In-situ* Annealed Films

Figure 6.23 show the best deflections from the *in-situ* annealed films. From the plots, it is clear that none of the LAM-produced film exhibited significant deflection. At first, this result may seem surprising. Our XRD results showed that the films were amorphous and our SEM EDS results indicated that the overall composition of the films was close to the target composition. These results suggest that our films should be strongly magnetostrictive. The lack of measurable deflection can be explained by observing the film topography after annealing. Figure 6.24 and 6.25 show SEM micrographs of the films which show that they are extensively cracked.

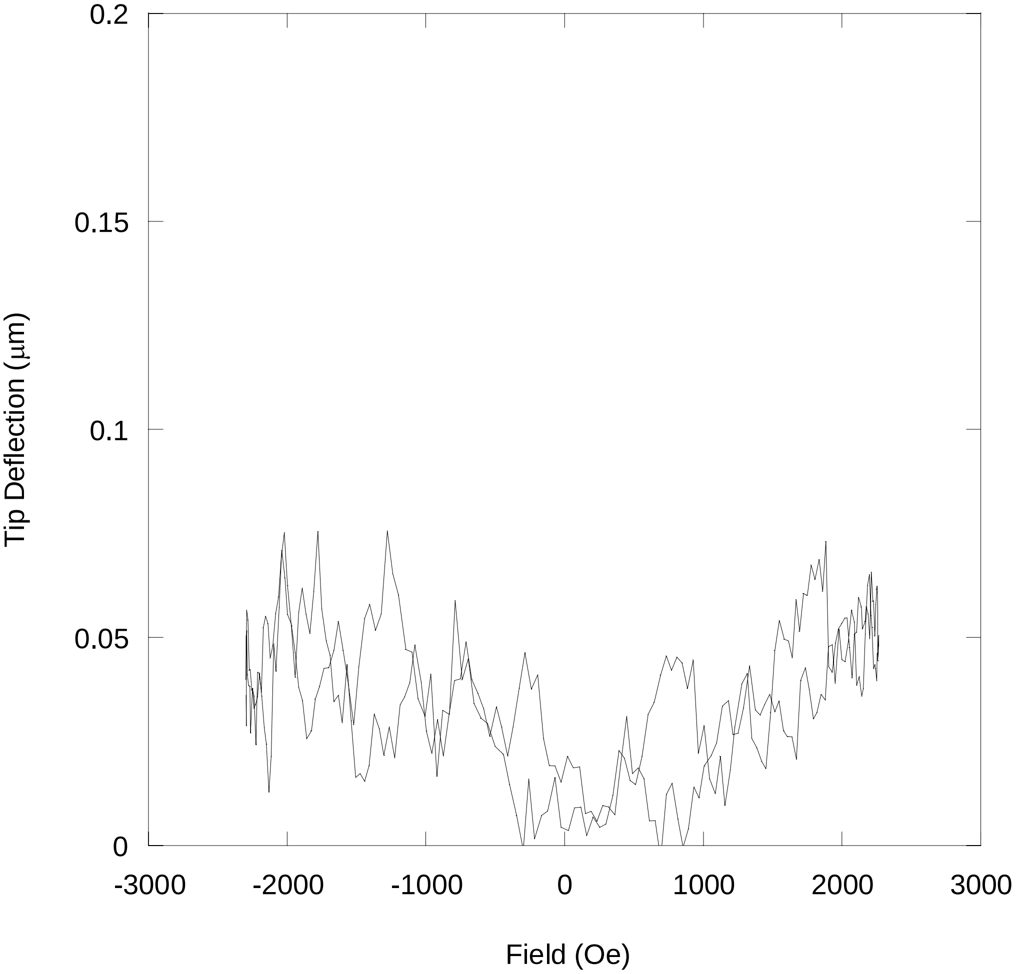

Figure 6.23: Tip deflection of LAM cantilever annealed at 700°C. Thickness of the film is 6.5 μm.

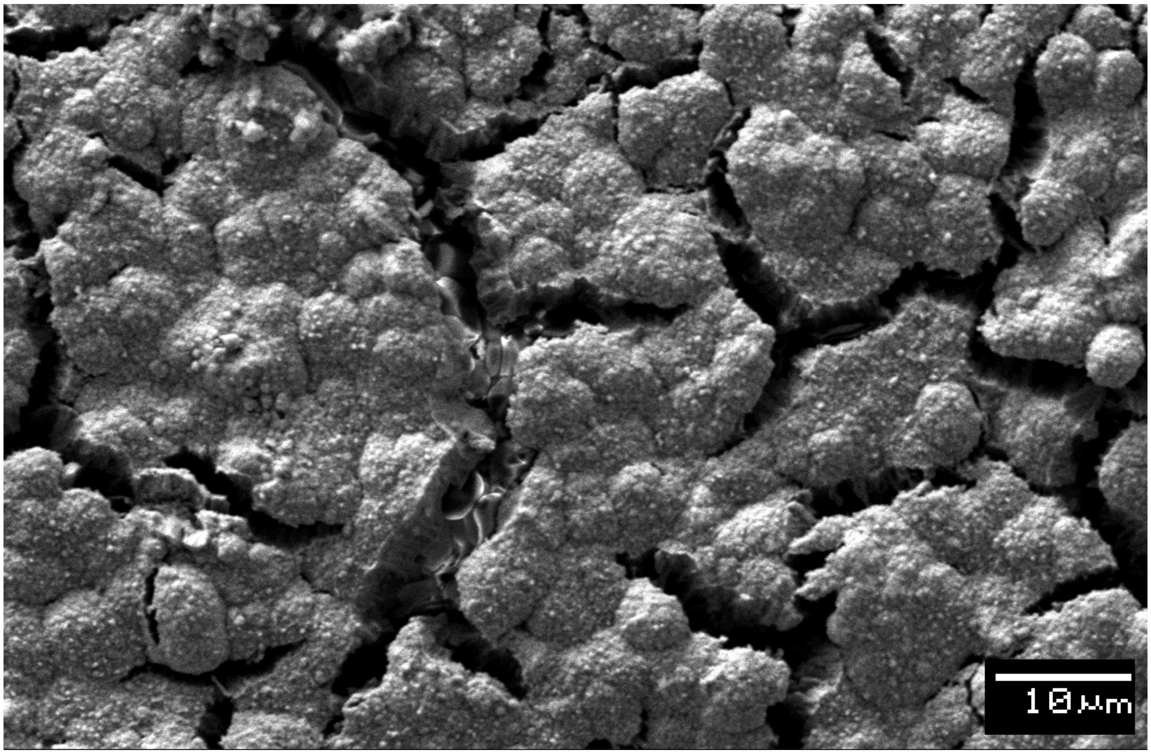

Figure 6.24: Plan view SEM micrograph of film after annealing showing extensive cracking.

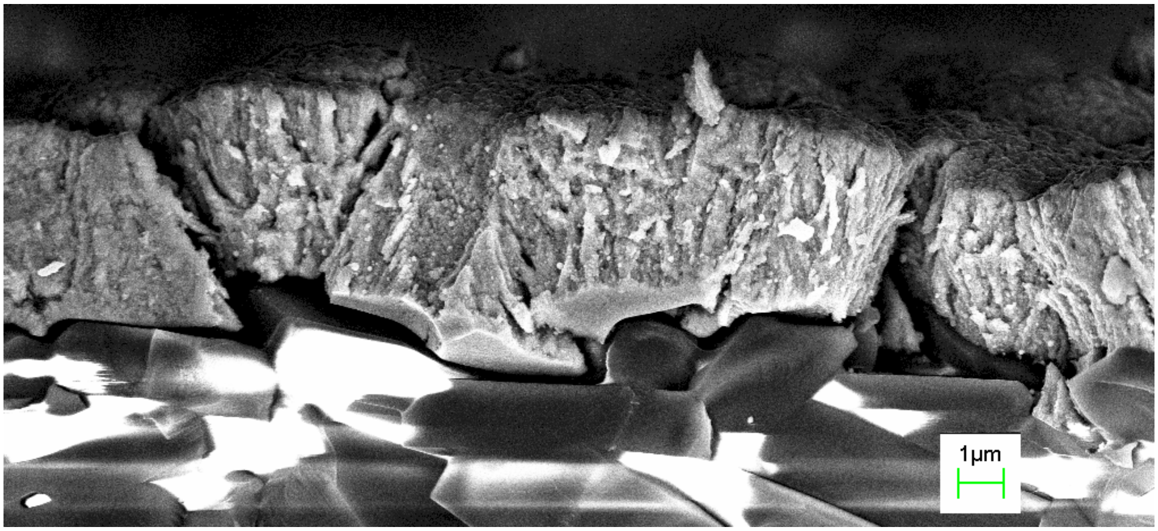

Figure 6.25: Cross-sectional SEM micrograph of film after annealing showing cracking and delamination of the film.

The cause of the cracking is the thermal expansion mismatch between the film and substrate. The thermal expansion coefficient is 8×10^{-6} /°C for alumina. It is assumed that the thermal expansion coefficient for the LAM films is the same as bulk $Tb_{0.3}Dy_{0.7}Fe_{1.92}$, 12×10^{-6} /°C. This mismatch puts the films annealed *in-situ* in tension upon cooling from the annealing temperature and explains the fracture morphologies of the films. Thus, the small measured deflections are primarily due to cracking in the films and the concomitant reduction in Youngs modulus because of thermal expansion mismatch between the substrate. It may also be low because of oxide and nitride contaminants in the film that are evident in the XRD pattern in Figure 6.19.

6.7 The Effect of Reduction-sintering

6.7.1 Introduction to Reduction-sintering Experiments

In another set of experiments, LAM produced $Tb_{0.3}Dy_{0.7}Fe_{1.92}$ films made using helium were annealed in a reducing atmosphere. The XRD of *in-situ* annealed films had shown that there was some amount of oxide and nitrides in the film. Reduction-annealing should remove any oxygen present in the films regardless of when oxides were formed in the process or when the films were exposed to air. Films were deposited according to the procedures and conditions described previously. Helium gas was used to allow for direct comparison with *in-situ* annealed films. After deposition, the films were removed from the vacuum chamber and annealed in a tube furnace. UHP hydrogen (99.999%) was used and annealing temperatures ranged from 250°-950°C. A plot of a heating profile during annealing in hydrogen is shown in Figure 6.26. The temperature of the furnace was increased to 100°C at 5° C/min and held for 1 hour to remove water vapor and for normalization of the gas environment. The furnace was then brought up to the target reduction temperature at 5°C/min. The hold time at the specified temperatures was 1 hour.

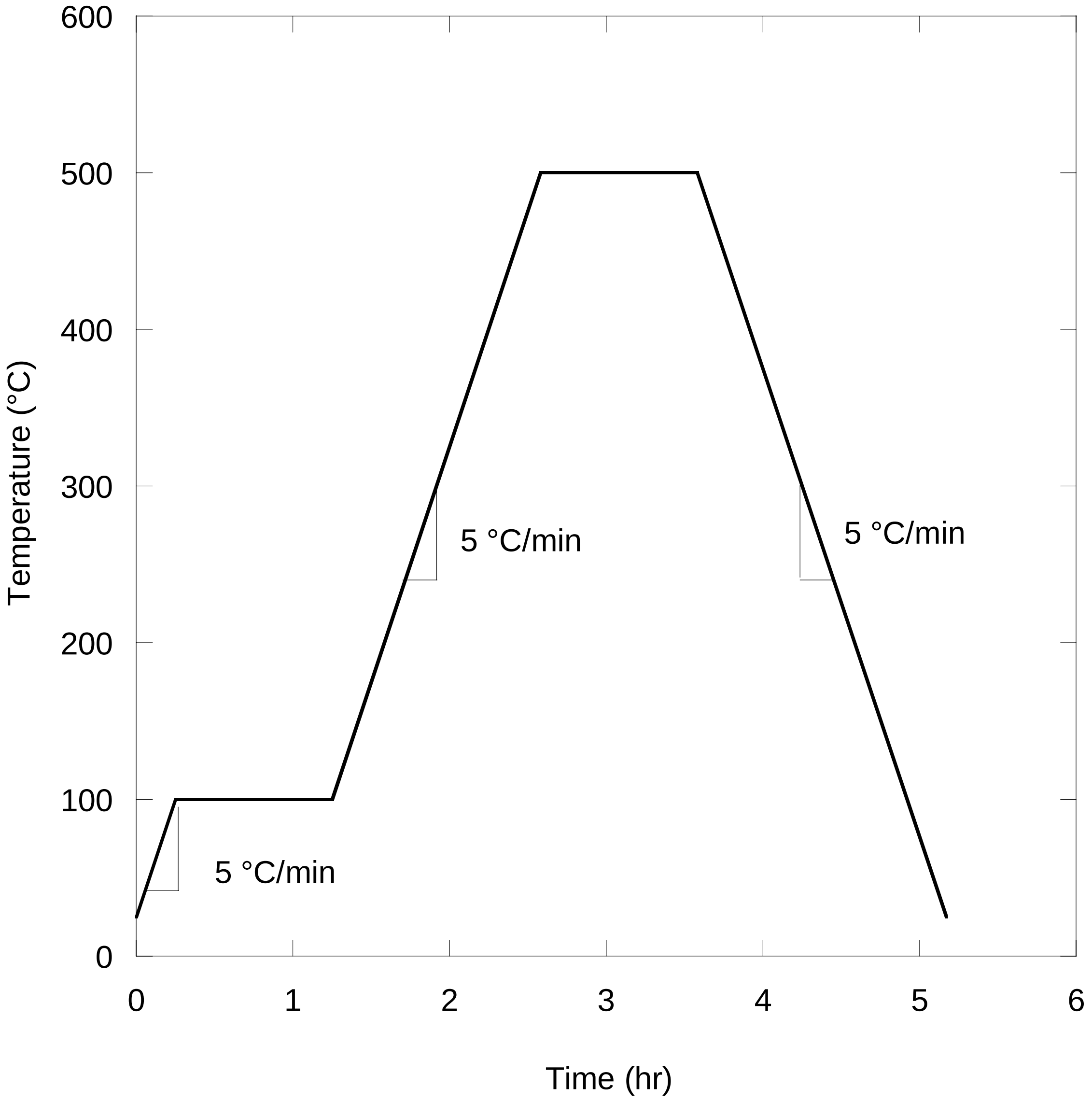

Figure 6.26: Heating profile for reduction-annealing at 500°C. Heating and cooling rates were the same for all reduction-annealed samples.

6.7.2 Structure of Reduction-annealed Films

The profile of reduction-annealed LAM film is similar to those used *in-situ* annealed samples (see Figure 6.18 for a typical profilometry scan). Films that were reduction-annealed had thicknesses that ranged from 4–20 μm. XRD for reduction-annealed films are shown in Figure 6.27.

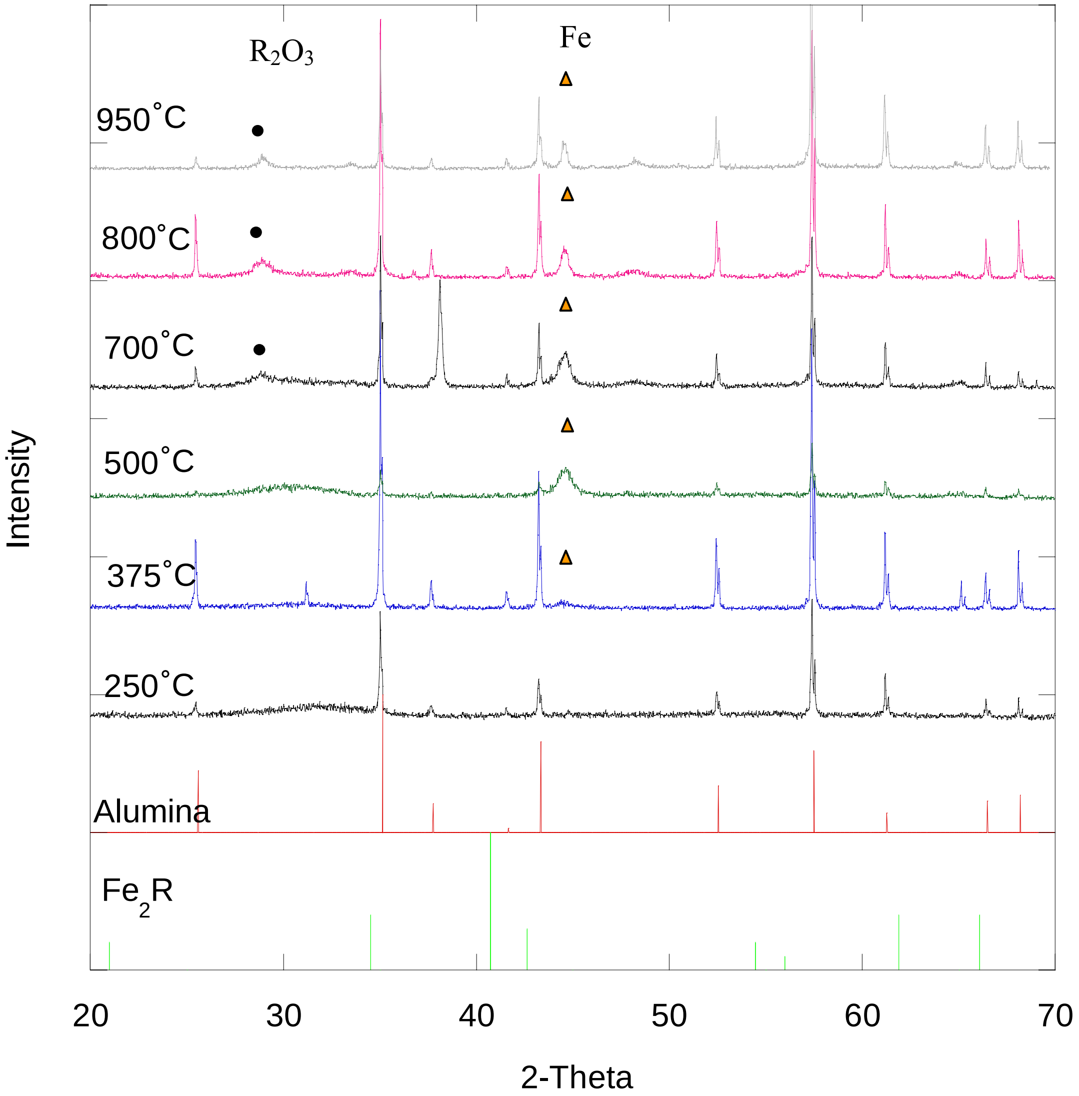

Figure 6.27: XRD spectra of reduction-annealed $Tb_{0.3}Dy_{0.7}Fe_{1.92}$ films.

XRD of the reduction-annealed LAM films shows that the films are amorphous until they are reduced at 375˚C when α-Fe nucleates. As the reduction-annealing temperature is increased, α-Fe coarsens. At 700˚C, crystalline R_2O_3 (R = Tb or Dy) is present and coarsens at higher temperatures. It is somewhat surprising given previous reports, that even at annealing temperatures of 950°C, no R_2Fe was formed. The reasons for this and the reasons for the formation of R_2O_3 are explored in section 6.8.

Figure 6.28 is a plan view SEM micrograph of a typical reduction-annealed film. Cracking of the films due to thermal expansion coefficient mismatches and thick films with low density, thus low strength, is observed here as it was for the *in-situ* annealed films. Figures 6.29 – 6.34 are SEM cross-sectional images of reduction-annealed films.

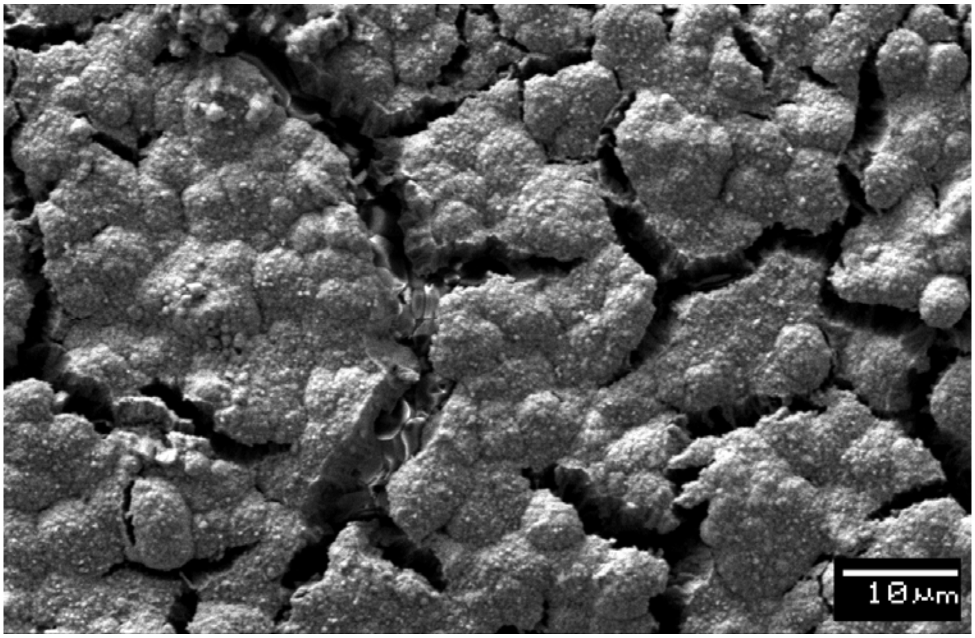

Figure 6.28: Plan view SEM micrograph of $Tb_{0.3}Dy_{0.7}Fe_{1.92}$ reduction-annealed at 500˚C on alumina.

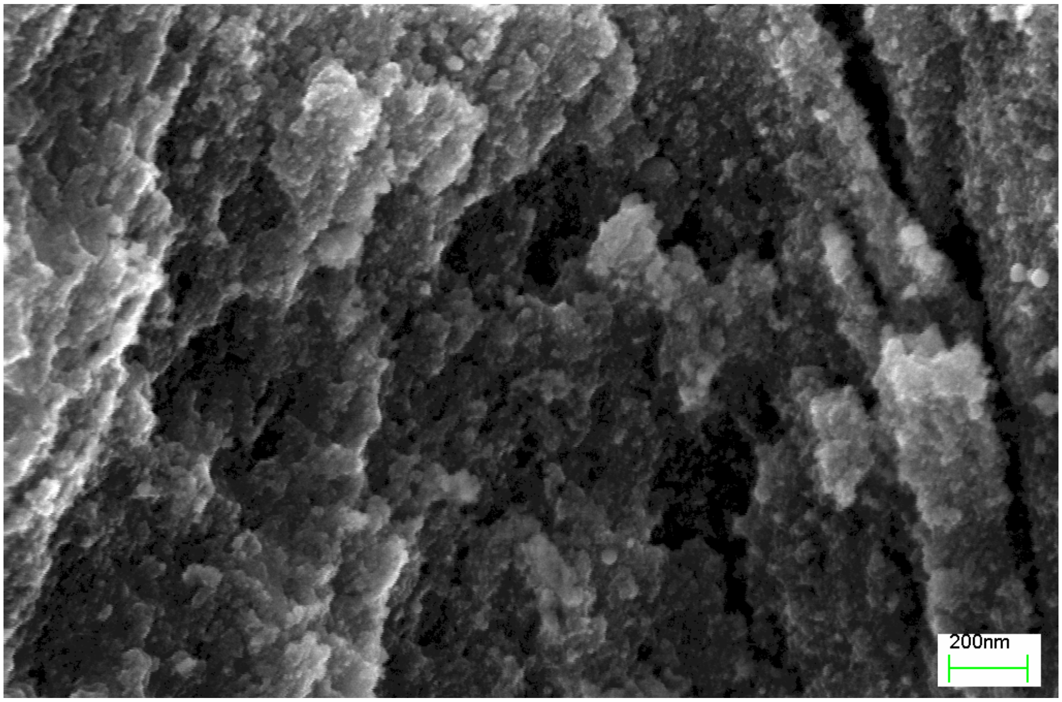

Figure 6.29: SEM cross-section of film reduction-annealed at 250˚C.

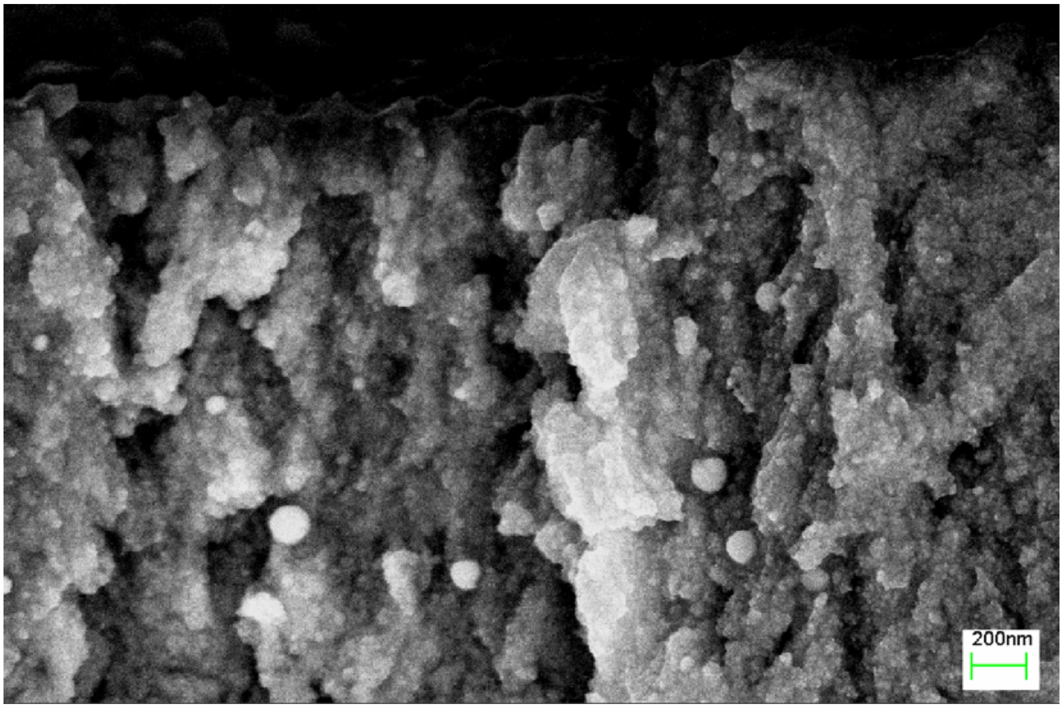

Figure 6.30: SEM cross-section of film reduction-annealed at 375˚C.

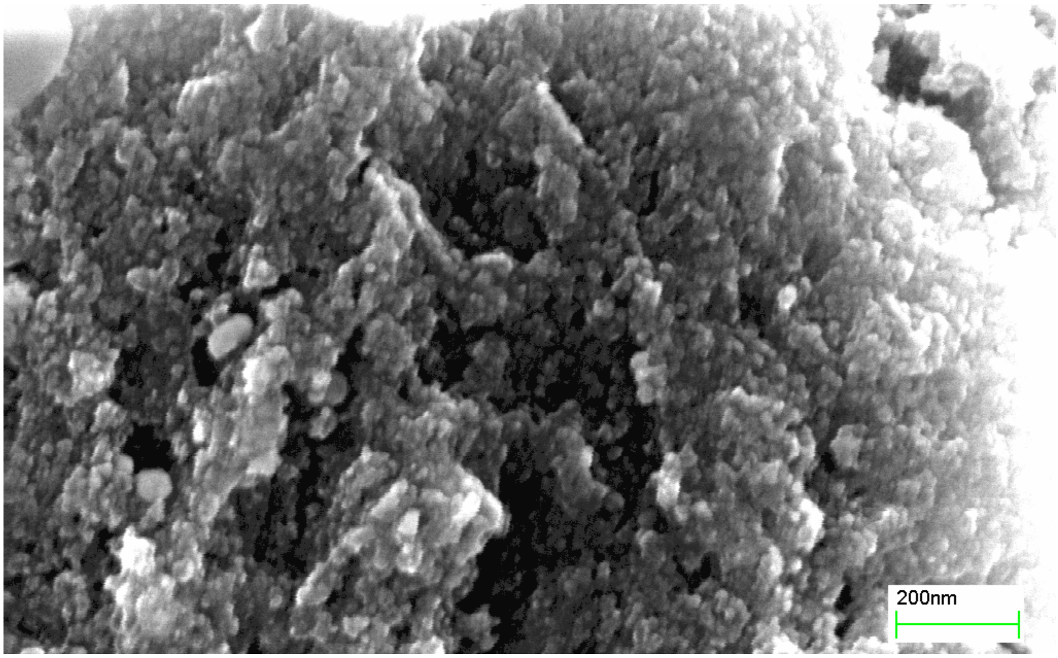

Figure 6.31: SEM cross-section of film reduction-annealed at 500˚C.

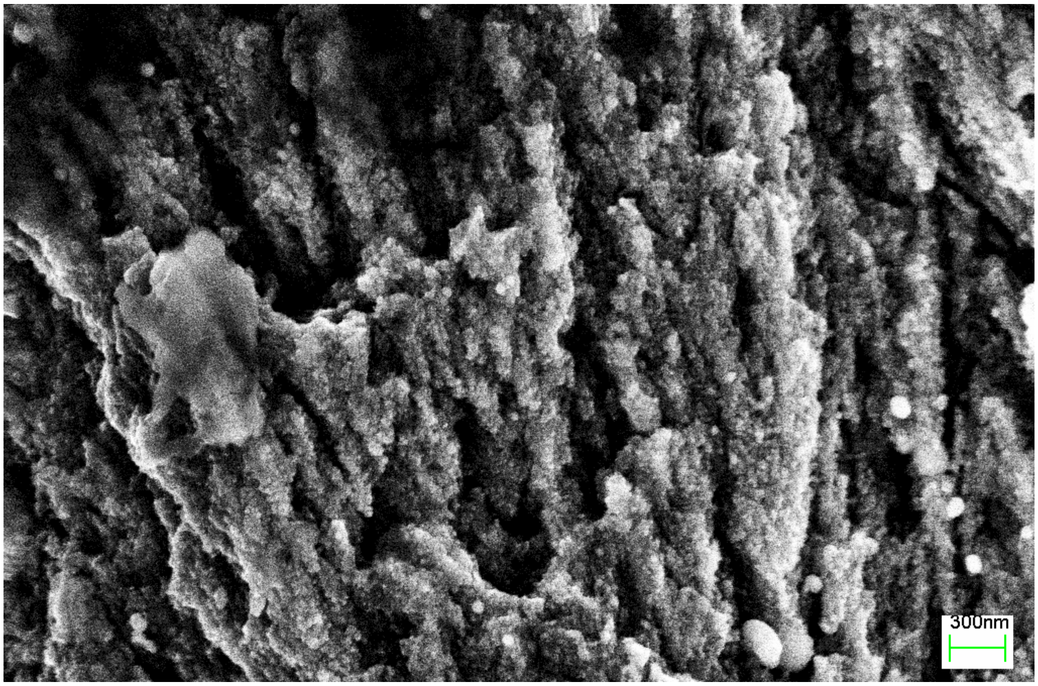

Figure 6.32: SEM cross-section of film reduction-annealed at 700˚C.

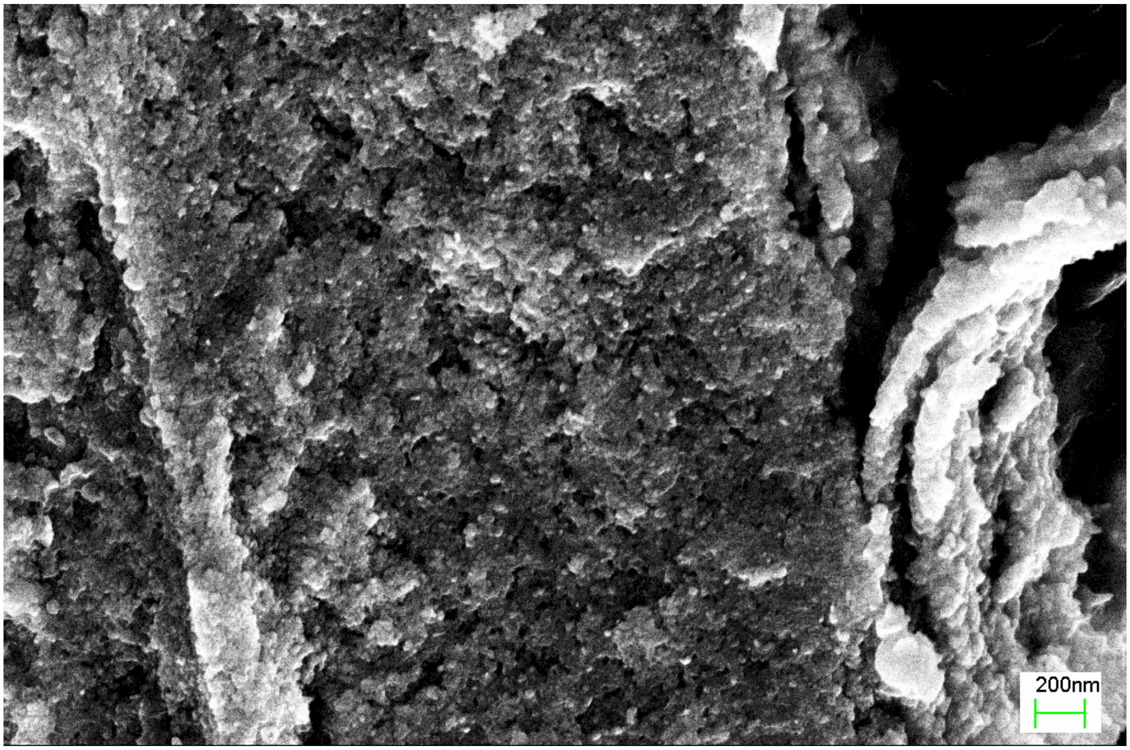

Figure 6.33: SEM cross-section of film reduction-annealed at 800˚C**.**

The striking attribute of the films as seen in the cross-sectional micrographs is the consistent feature size of the particles for all the annealing temperatures. There is no appreciable coarsening of particles or sintering. This is very different from what has been observed in silver nanoparticle films made by the LAM process which exhibit a much lower annealing temperature than bulk silver.[51]

6.7.3 Magnetic Properties of Reduction-annealed Films

Figures 6.34 – 6.35 show the hysteresis loops for the LAM films that were reduction-sintered. Figure 6.36 shows the saturation magnetization and coercivity of the films as a function of reduction-annealing temperature.

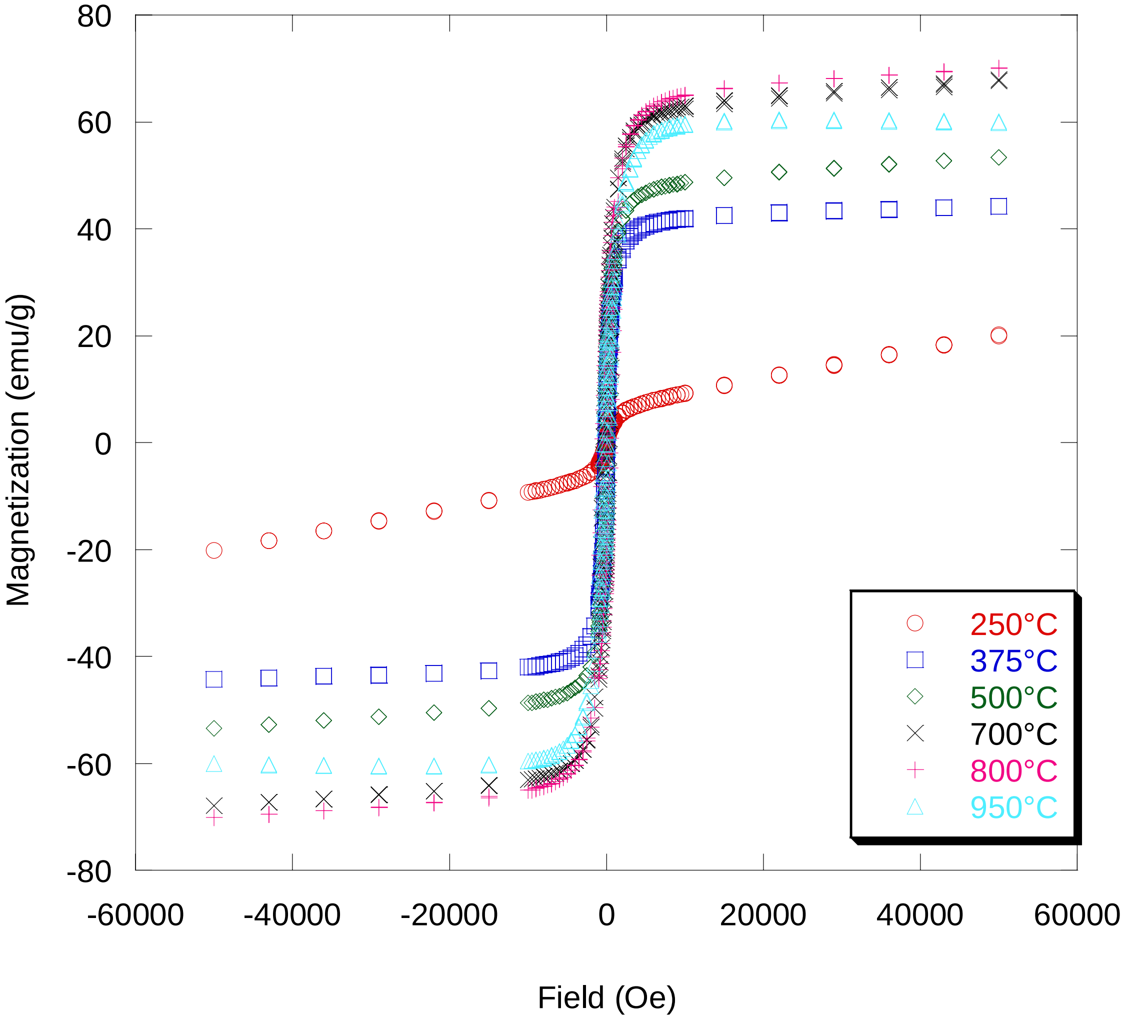

Figure 6.34: Hysteresis curves for reduction-annealed films.

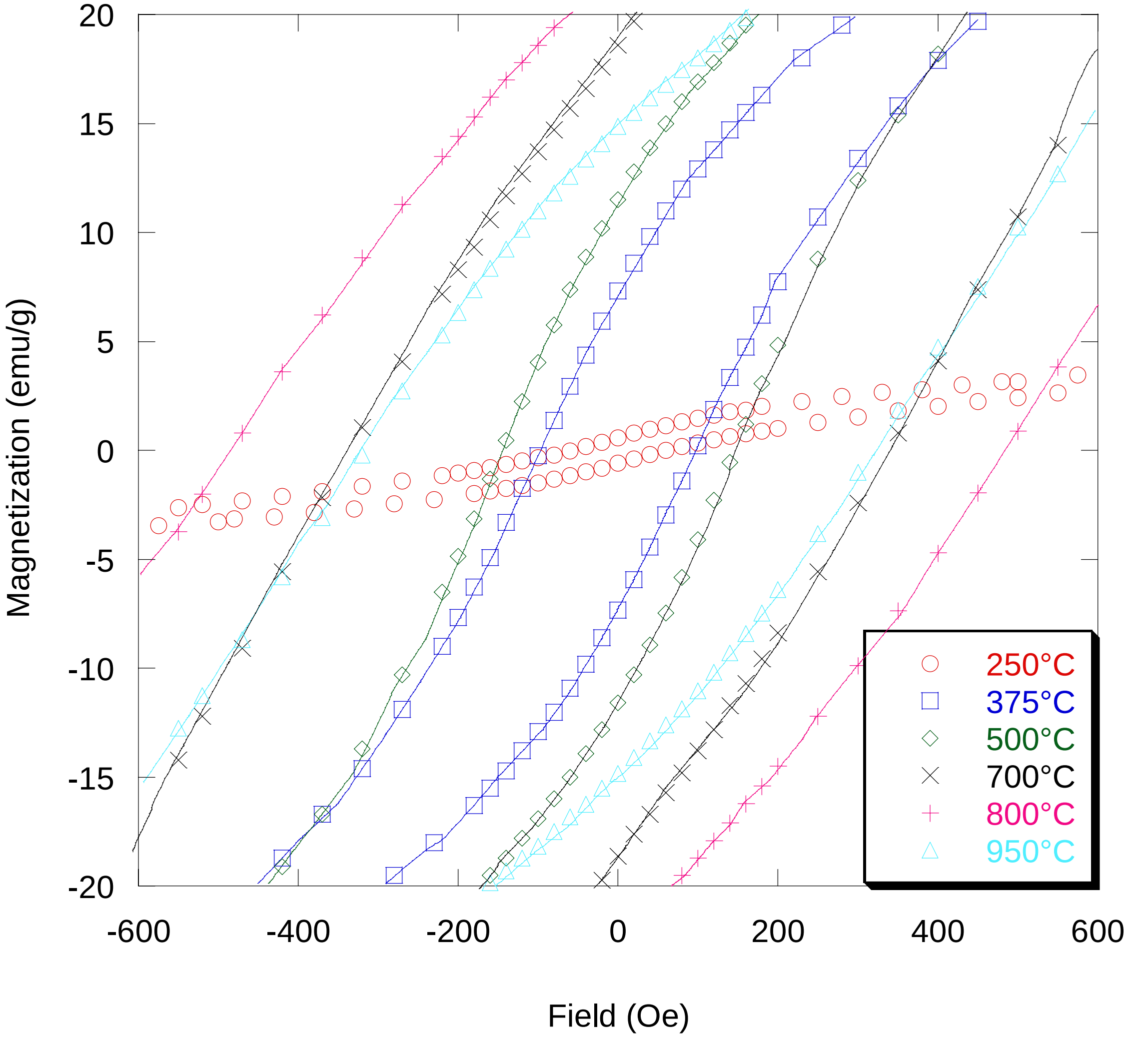

Figure 6.35: Low field hysteresis curve for reduction-annealed films. Numbers in legend indicate annealing temperature (˚C).

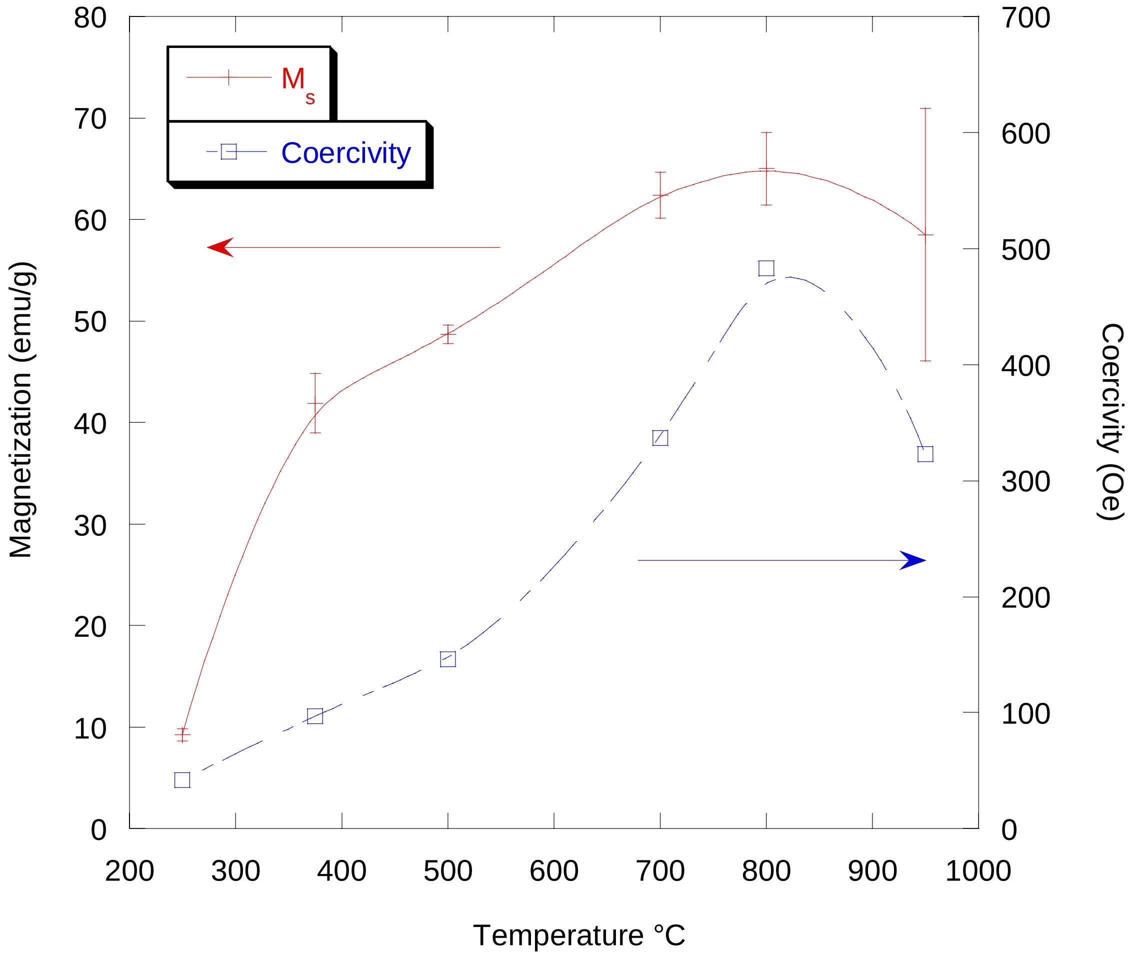

Figure 6.36: Saturation magnetization and coercivity of films as function of reduction-annealing temperature.

Saturation magnetization saturation increases sharply between 250˚-375˚C. It is likely that this increase in magnetization is due to the onset of reduction. At higher temperatures, M_s increases steadily from 375°-800° C due to nucleation and coarsening of α-Fe. The coercivity of the films follows a similar trend.

6.8 Nanoparticle Compositional Anaylsis

6.8.1 Introduction to Compositional Analysis

Although the TEM EDS results presented earlier on many nanoparticles showed that the composition of the LAM produced films was similar to the starting material, the inability to form the crystalline Laves phase even at high annealing temperatures does not agree with previous work on amorphous thin films. Those studies have all shown that crystallization occurs in amorphous thin films below 600˚C. Since crystallization requires diffusion, our annealing results suggest that crystallization is inhibited for LAM films of $Tb_{0.3}Dy_{0.7}Fe_{1.92}$. In an effort to find the cause of the inhibited crystallization, additional compositional analyses were performed.

6.8.2 TEM Compositional Analysis

TEM studies were performed using nanoarea EDS, nanobeam EDS and STEM on a JEOL 2010F microscope. The nanoparticles studied were made with LAM in helium and jet deposited onto lacey carbon grids. The probe size for the nanoarea studies was 5–100 nm. Nanobeam EDS spectra were taken with 1.0–1.5 nm probe sizes. STEM was preformed with a 1.0 nm electron beams. Nanoarea EDS spectra were taken with a variable beam size that was adjusted to cover only the particle of interest. The 1.5 nm probe was used for nanobeam EDS on particles larger than 40 nm. A 1 nm probe was used for all other particles. Groups of particles were often in intimate contact with each other on the TEM grid. To prevent complications of analysis from more than one particle, nanoarea studies were performed on particles that were separated from other particles when possible.

With the irregular starting $Tb_{0.3}Dy_{0.7}Fe_{1.92}$ feedstock powder that was ground with mortar and pestle, three types of particles were observed; small particles (<10 nm), intermediate particles (10-40 nm) and large particles (>40 nm). Figure 6.37 shows TEM images of the three sizes of particles.

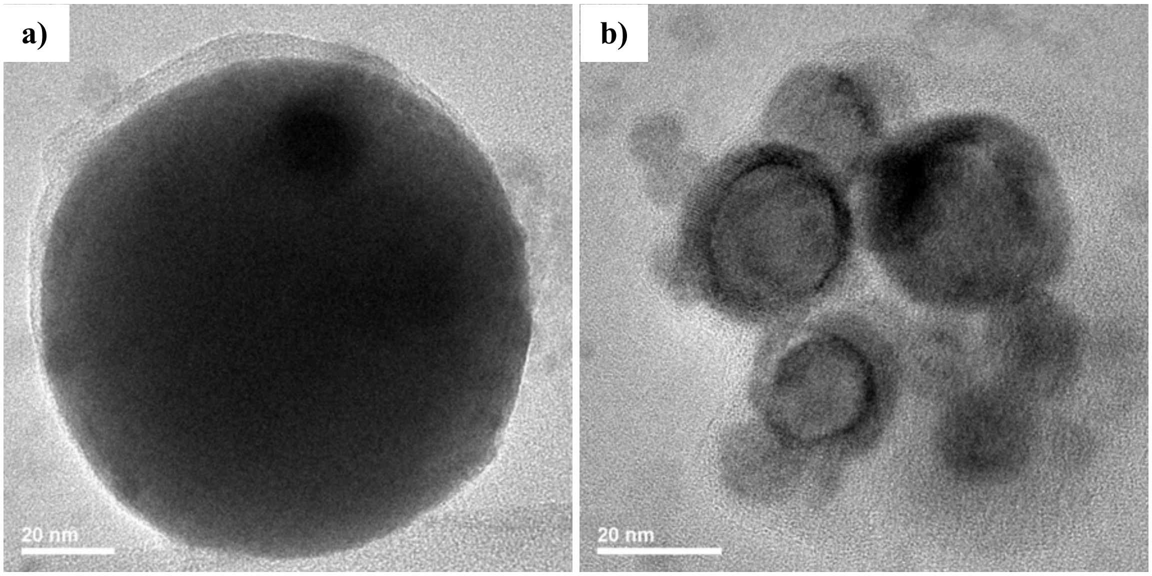

Figure 6.37: TEM bright field of a) large particles and b) intermediate particles. The small particles can be seen in both images around the other particles.

Statically there are only a few particles in the large particle size. Most of these particles are spherical however, some are not. The large particles are too big to have been ablated and thus resulted from feedstock material that was partially ablated, shadowed in the ablation process or missed by the laser. A larger fraction of the particles were between 10-40 nm. The intermediate particles were all spherical. From previous analysis on silver nanoparticles, these formed either in very dense regions of the plasma or by evaporation prior to breakdown.[26] The largest fraction of particles was between 1-10 nm. These particles are small and form by coalescence in the low pressure region behind the shock wave after breakdown. Compositions being referred to as rare earth rich or deficient are with respect to the starting material, $Tb_{0.3}Dy_{0.7}Fe_{1.92}$.

The range of compositions found in large particles determined by nanoarea EDS is $Tb_{0.16\text{-}0.27}Dy_{0.25\text{-}0.44}Fe_{0.31\text{-}0.59}$. The average composition is rare earth rich. The range from intermediate particles is $Tb_{0.09\text{-}0.14}Dy_{0.25\text{-}0.32}Fe_{0.53\text{-}0.66}$. The average composition here is iron rich. Nanoarea EDS of 3-4 of the smallest particles shows that they have a composition of $Tb_{0.09\text{-}0.12}Dy_{0.22\text{-}0.31}Fe_{0.56\text{-}0.69}$, similar in iron richness to the intermediate particles.. The nanoarea EDS results show that there is some segregation of the elements within individual particles and between particles.

Nanobeam EDS results of the outer portions of large particles show that the average stochiometry of the outer portions are rare earth rich and the inner portions are rare earth deficient. Nanobeam EDS of the intermediate particles shows that the outer region is also rare earth rich and the inner region is very rare earth deficient. Figure 6.38 shows two images of the same nanoparticles taken before and after nanobeam EDS was performed. From the damage by the TEM beam, it is clear where EDS spectra were taken. Nanobeam spectra from the shell showed that the composition of the shell is $Fe_{11}Tb_{27}Dy_{62.}$ Nanobeam EDS probes of the core shows a composition of $Fe_{82}Tb_{7}Dy_{11.}$

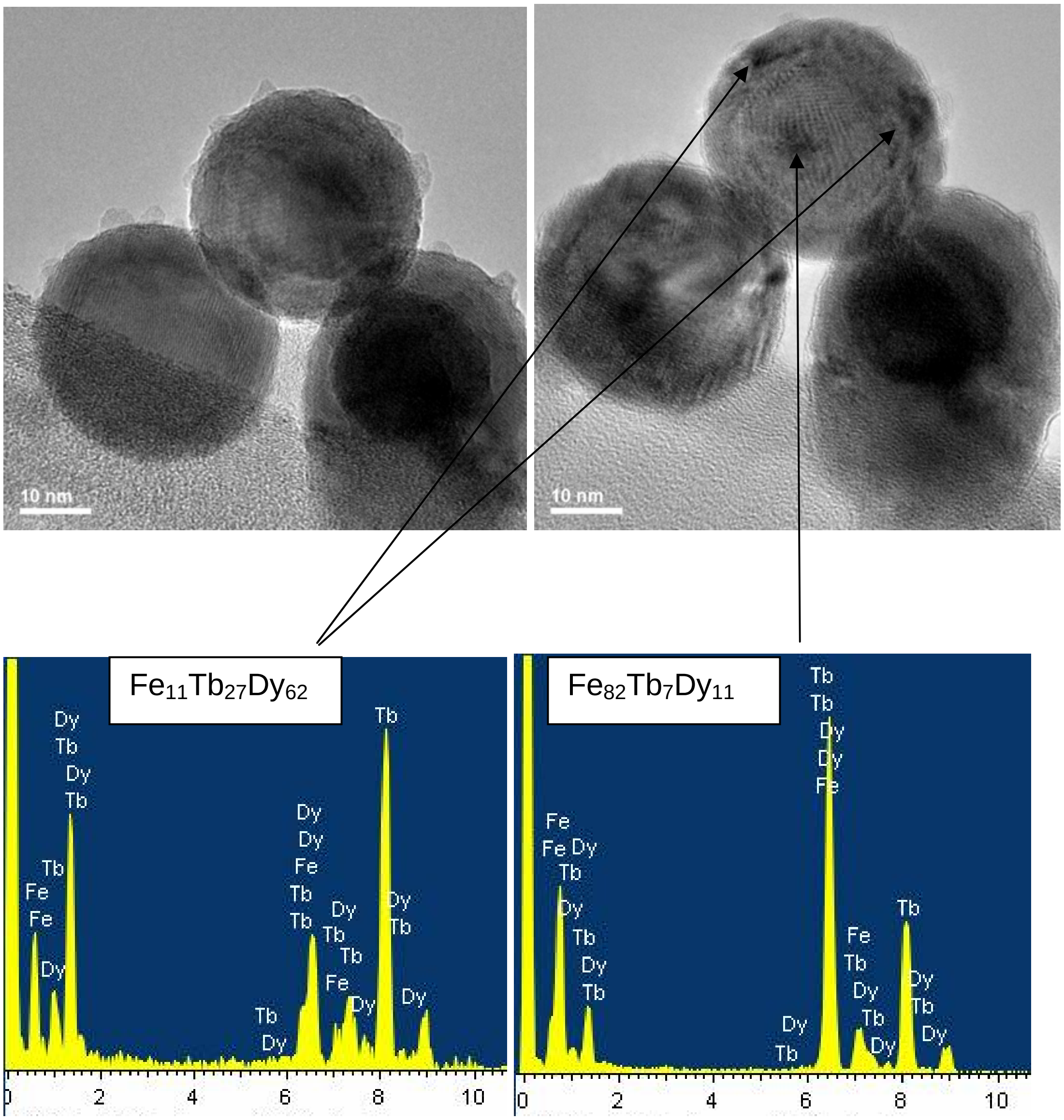

Figure 6.38: TEM nanobeam EDS spectra showing difference in composition between shell and core.

Nanobeam experiments showed that the outer regions of the large and intermediate particles are rare earth rich and the inner regions tend to be rare earth deficient. STEM was done to more clearly demonstrate this phenomenon. Figure 6.39 shows a STEM line scan of a particle with a diameter of 32 nm.

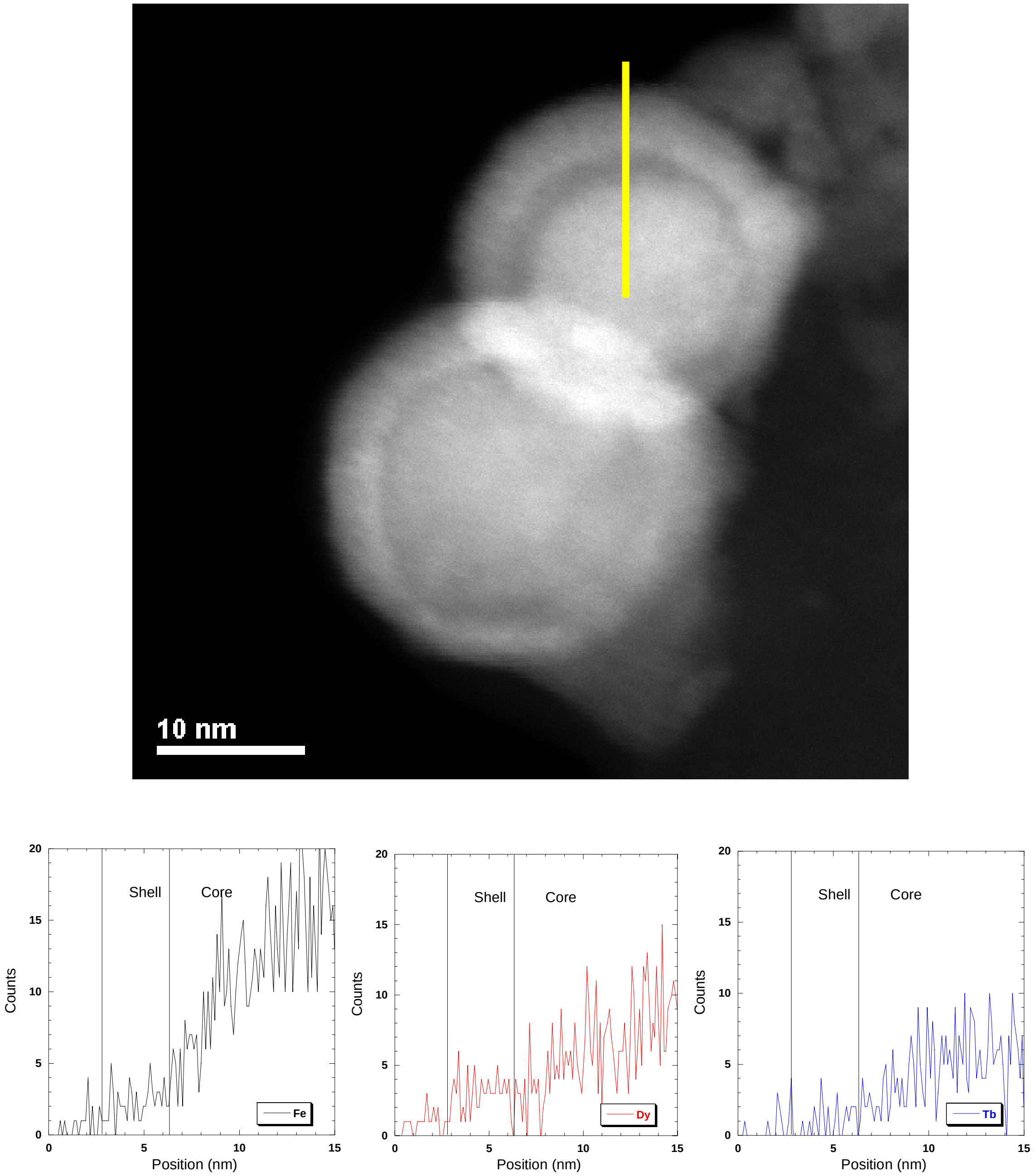

Figure 6.39: STEM line scan of LAM produced particle showing a core-shell structure.

The STEM images show a clear core-shell structure. The corresponding EDS line scan demonstrates that there is a rare earth rich outer region. Figure 6.40 shows more particles that exhibit this core-shell structure to rule out the notion that the image consist of one particle sitting on top of another.

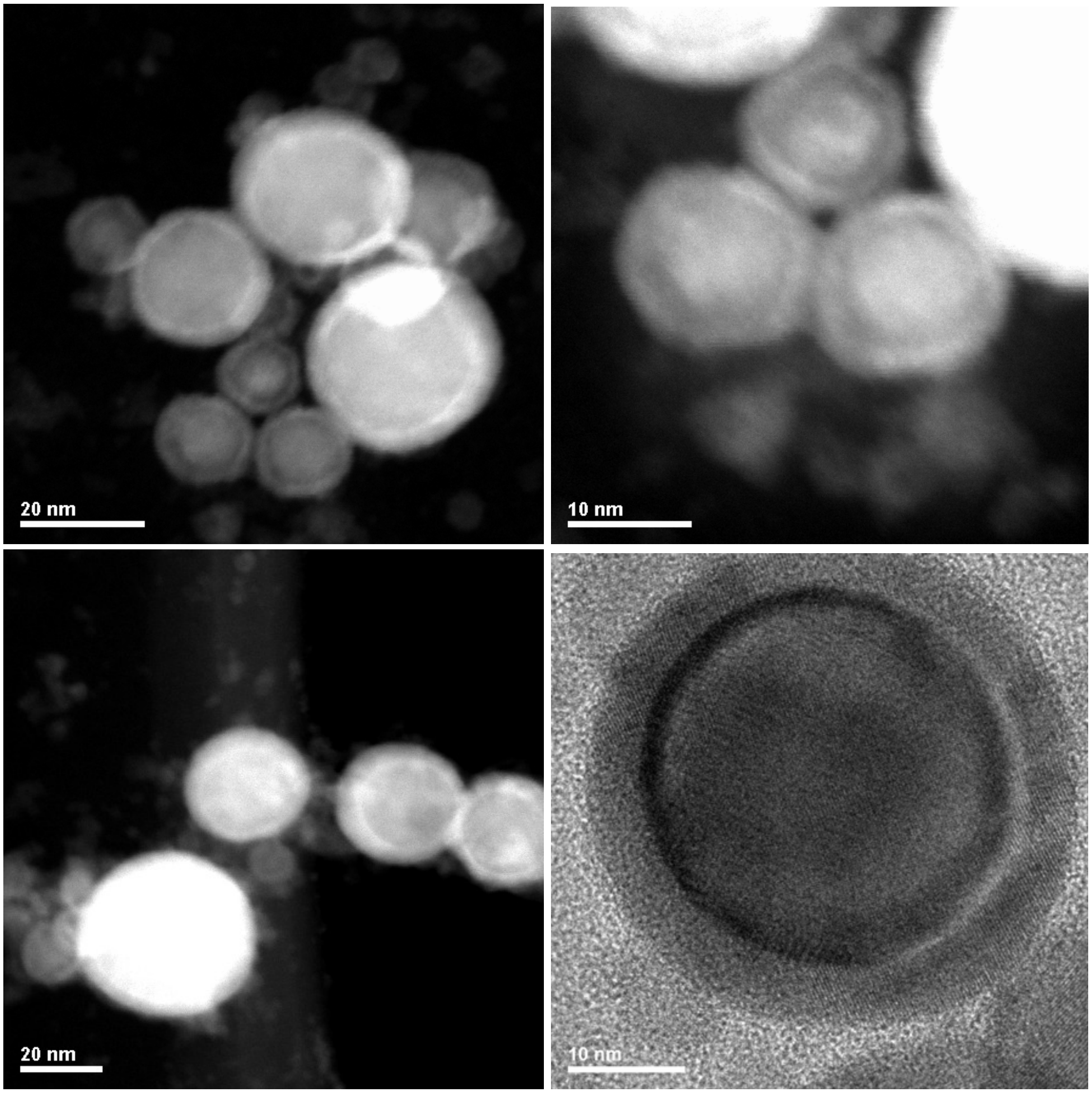

Figure 6.40: STEM and bright field images of core-shell particles.

TEM compositional results from nanobeam EDS and STEM show that there is segregation into a core-shell structure on the intermediate and large particles. The shell is rare earth rich and the cores have more iron. In addition, the STEM detector is an annular dark field detector and thus there is z-contrast data in the images. For a material with uniform composition, there is a monotonic decrease in contrast as thickness decreases. In the STEM images, the shells (which are thinner than the cores) are just as bright as the core which indicates that the shells are composed of elements with higher atomic mass than in the cores. The structure of small particles cannot be determined by these techniques due to the sample drift but are expected to have the same structure.

6.8.2 XPS Analysis

XPS studies were done on as deposited LAM films made in helium gas. Figure 6.41 shows the XPS spectra of iron and terbium for different argon sputtering times.

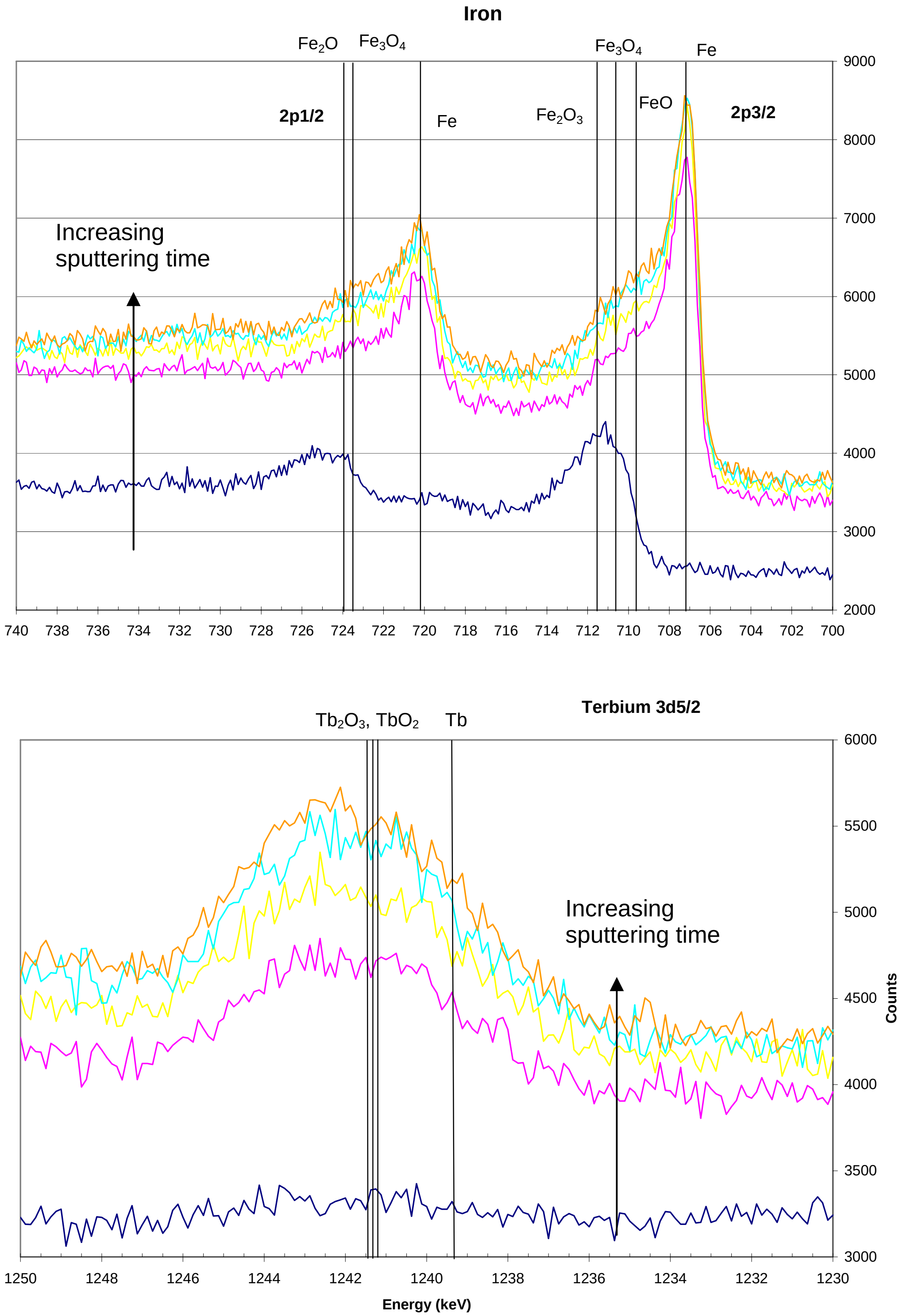

Figure 6.41: XPS spectra for iron and terbium with increasing sputtering time.

The depth of each XPS scan is unknown because sputtering rates are material dependant and calibration was not performed on jet deposited $Tb_{0.3}Dy_{0.7}Fe_{1.92}$ nanostructured films. The initial survey scan shows that there is only iron oxide (Figure 6.41 a). With increasing sputtering times, there is a shift from iron oxide to elemental iron. Terbium oxide is not present in the initial scan however it does persist throughout the rest of the depths surveyed and the spectrum does not shift towards elemental terbium (Figure 6.41 b). Terbium is not initially present and this can be explained with experiments on TbFe film by Dover et al. In oxidation experiments, they showed that the species segregate in a predictable pattern. In the films, a thin layer of Fe_2O_3 (2 nm) forms on the surface followed by a thicker layer of Tb_2O_3 (6 nm) before reaching the layer of sputtered (non-oxidized) film.[52] Combining Dover's experimental results with our XPS and TEM results, we can conclude that the nanoparticles produced in this study segregate into three layers: a thin iron oxide layer forms (not obvious in TEM images) on the nanoparticles that covers a thicker rare earth rich oxide. The rare earth elements preferentially oxidize which pushes the remaining iron into the core. In small nanoparticles, the volume of material is finite. Thus, magnetostriction is greatly reduced because the oxidized regions are not magnetostrictive and the composition of the unoxidized core is very iron rich and far from RFe_2.

6.9 Discussion

The LAM process was investigated as a method for producing thick films of magnetostrictive materials. Films made in helium show a higher magnetization and lower coercivity compared to films made with argon due to the smaller particle size and higher density. Both as-deposited films are amorphous and have a M_s lower than the thin films due to higher surface area and film porosity.

Attempts were made to increase the modulus and homogeneity (and thus M_s) by *in-situ* annealing. Films were deposited and annealed in vacuum from 300°-700°C for 1 hour. XRD showed that α-Fe nucleated at 500°C and proceeded to slowly coarsen as the annealing temperature increased. The Laves phase not found even at high annealing temperatures. The magnetization increased significantly between 400°- 500°C due to nucleation of α-Fe. Coarsening of α-Fe increased the magnetization for temperatures above 500°C. Cantilever films annealed *in-situ* showed little tip deflection because of the films cracked and delaminated due to the low film density and thermal expansion mismatch between the film and the substrate. Also, they did not form the RFe_2 Laves phase.

Films were also reduction-annealed from 250°-950°C for 1 hour in 99.999% hydrogen. XRD shows that α-Fe nucleated for films annealed at 375°C and higher, and continued to coarsen with increasing reduction-annealing temperature. Crystalline R_2O_3 was observed for samples reduction-annealed at 700°C and higher. Given the highly reducing atmosphere during annealing, it is likely R_2O_3 formed after the sample was taken out. Saturation magnetization increased considerably for films reduction-annealed at 250°C and 375°C which indicates that reduction had started. M_s continued to increase steadily for film reduction-annealed up to 800°C due to coarsening of the α-Fe. The Laves phase was not observed in the reduction-annealed films. Reduction-annealed films also cracked and did not show significant cantilever tip deflection. It was unexpected that the Laves phase did not form for either annealing treatment. Further investigation using STEM and nanobeam EDS showed segregation within intermediate particles (10-30 nm) into a rare earth rich shell and iron rich core due to preferential oxidation. XPS on an as-deposited LAM film verifies this by showing that a shift from iron oxide to elemental iron with increasing sputtering depth which indicates that there is an additional thin layer of iron oxide on the outside of the rare earth rich shell that was not observed in the TEM. No elemental terbium, only terbium oxide, was observed throughout the sputtering depth. These conclusions are consistent with studies performed on Fe-Tb thin films. In fact, Uchida et al. have shown that oxidation and segregation of TbFe thin films occurs even at 5×10^{-9} Torr of vacuum.[53] This also explains why only terbium oxide was observed in the XPS spectra.

Although not directly observed, it is likely that the core-shell structure seen in the larger particles also occurs in the smaller particles due to preferential oxidation. In the *in-situ* annealed films, the segregated and oxidized shell acts as a diffusion barrier for crystallization of the R_2Fe Laves phase. The oxide shell also slows the rate of oxidation and prevents further segregation even at high annealing temperatures and upon removal from the vacuum chamber. Since the oxidization continues, prolonged exposure of the $Tb_{0.3}Dy_{0.7}Fe_{1.92}$ film to the atmosphere probably resulted in a greater degree of oxidation and segregation of the iron to the core and rare earth elements to the shell. The oxide was reduced during reduction-sintering above 375°C. However, the iron crystallized and coarsened in the core and the rare earth coarsened on the shell. When the film was removed from the furnace, the rare earths oxidized and formed crystalline R_2O_3.

Both segregation and oxidation are detrimental to this material system because magnetostriction decreases quickly with iron rich compositions, and the oxides of the rare earths are not magnetostrictive.[43] Since oxidation and segregation is observed even in low partial pressures of oxygen (UHV vacuum), ablation at atmospheric conditions only increases the likelihood of oxidation. In addition, open porosity and high surface to volume ratio of nanoparticles increases the ratio of oxidized to non-oxidized material, further reducing the magnetization.

Chapter 7

Conclusions and Future Work

7.1 Conclusions

There has been an increased interest in magnetostrictive materials over the past decade for integration into MEMS devices. Of particular importance is the Fe_2R (R=Tb, Dy) intermetallic because the crystalline Laves phase has the largest room temperature magnetostriction. It is also an attractive material because it does not require physical connections and its motion is reversible. MEMS devices are intended to be small and thus the magnetic fields to operate the devices must also be small. Fe_2R has not been widely integrated into devices because its coercive force is high, thus it requires large external fields. Two ways to reduce the coercivity are by making it amorphous or reducing the crystallite size to less than 20 nm. In this study, three laser processing techniques were explored to fabricate magnetostrictive films of $Tb_{0.3}Dy_{0.7}Fe_{1.92}$. All three techniques produced amorphous films because the vaporized material was quickly quenched.

Magnetostrictive films produced by PLD were studied at two laser fluences. Both films were dense and exhibited good adhesion to silicon substrates. SEM and TEM EDS indicate the composition of the target was preserved in the films. Splattering due to recoil pressure on the Knudsen layer was observed and was larger for the films produced at high fluences. The splatters did not have a large effect on the magnetostriction. However, they may have increased the coercivity slightly. As expected, the amorphous films had a lower magnetization compared to bulk. Although comparisons to films produced by other methods are difficult due to large discrepancies in Youngs modulus and Poissons ratio, the PLD films fabricated here exhibited magnetostriction ($\lambda_{\|}= 305$) that compared favorably to films of similar composition deposited by other techniques.

The FPA technique was studied as a way to make films of $Tb_{0.3}Dy_{0.7}Fe_{1.92}$ rapidly using an aerosol process. This method utilizes jet deposition of relatively large amounts of nanoparticles (4.5 mg/hr with laser fluence at 2.5 J/cm^2 running at 10 Hz). However, the nanoparticles produced using this method had a broad size distribution which lowered the impaction energy for jet deposition and thus the films were not dense. Particle size generally increased with laser fluence, but magnetization did not. For films produced above the breakdown threshold, the saturation magnetization decreased with the number of laser shots on the target. In addition, segregation was observed between nanoparticles that were deposited. Segregation between particles was caused by extended expansion of a non-uniform vapor plume and target modification by repeated laser ionizations. Columnar structures were observed on the surface of the target after FPA, providing evidence that target modification contributed to the observed segregation in the nanoparticles. Segregation is detrimental to $Tb_{0.3}Dy_{0.7}Fe_{1.92}$ because iron-rich or iron-deficient compositions reduce magnetostriction and increase the anisotropy.

For these reasons, LAM offers a potentially better method (compared to FPA) for fabricating films of nanostructured $Tb_{0.3}Dy_{0.7}Fe_{1.92}$ using an aerosol process. In the LAM process, microparticles are ablated, and thus the surface modification should not be a factor. Also, the expansion of vaporized material during laser ablation is much smaller providing less opportunity for segregation. Films were fabricated by LAM in argon and helium. Although films produced in argon resulted in larger particles than films produced in helium, the measured magnetization was higher in the films made with helium because the films exhibited higher density. In addition, the coercivity of films made in helium was lower than for films made in argon due to the smaller particle size. However, TEM studies showed that the elements within a particle were segregated. The observed segregation was attributed to the preferential oxidation of the rare earth elements on the outside of the particle.

In an attempt to increase Youngs modulus and the density of LAM deposited films, *in-situ* annealing studies were performed. *In-situ* annealing did not result in the formation of the Laves phase crystal structure, and particle sintering was not observed even at high temperatures (700°C). The difficulty in crystallizing the Laves phase and in sintering was attributed to segregation and oxidation around each particle. The magnetization did increase with annealing temperature which resulted from crystallization and coarsening of α-Fe. However, the films cracked and delaminated because of the low density, no sintering due to core-shell structure and thermal expansion mismatch between the substrate and film. Cracking, segregation and oxidation of the films were causes of small magnetostriction of LAM produced films.

LAM films were also reduction-annealed in an attempt to densify the films and to reduced oxidized films. Reduction was observed for films annealed in hydrogen at 375°C or higher and crystallization of α-Fe was also seen for films annealed at 375°C or higher. Reduction and crystallization greatly increased the saturation magnetization. Further increases in temperature (up to 800°C) only coarsened the α-Fe, so a less dramatic increase in saturation magnetization was observed. Crystalline rare earth oxides were detected at films reduction-annealed above 700°C. This was due to prolonged film exposure to the environment prior to annealing and coarsening of iron in the core which caused extensive segregation of Fe, Tb and Dy and subsequent oxidation of the rare earths when exposed to air. Reduction of films even at temperatures as high as 950°C did not result in formation of the Laves phase due to this extensive segregation.

7.2 Future Work

Fabricating nanoparticles containing Tb and Dy elements presents an immense challenge because of the reactivity of the material. Although nanoparticles of TbDyFe compounds offer lower coercivity and better magnetic performance than bulk materials, the increased surface-to-volume ratio increases the likelihood of oxidation. It has been shown that terbium will getter oxygen even in UHV conditions. In addition, the difficulty in making nanoparticle films is the low film density means they possess a lower Youngs modulus. In addition, the films have open porosity which further exacerbates the problem of oxidation. A better understanding of when oxidation occurs in the ablation process and how to deposit or sinter nanoparticles in one continuous process is needed.

Segregation was observed to some extent between nanoparticles in all ablation processes studied here. In many ways FPA is similar to PLD. In these methods, the role of laser fluence on target surface modification has been studied. However, for LAM, the kinetics of particle formation behind the shock wave are not well understood. This is especially true for multicomponent materials. A better understanding of the formation processes would give keen insight on how to more effectively control laser ablation processes to produce more homogeneous materials with improved magnetic properties.

References

1 P. Janker, M. Christmann, F. Hermle, T. Lorkowski, and S. Storm, 'Mechatronics Using Piezoelectric Actuators', *Journal of the European Ceramic Society,* 19 (1999), p. 1127-31.

2 A.E. Clark, 'Chapter 7 Magnetostrictive Rare Earth-Fe_2 Compounds', in *Handbook of Ferromagnetic Materials,* ed. by E.P. Wohlfarth, (Amsterdam: Elsevier, 1980), p. 531-89.

3 G. Engdal, *Handbook of Giant Magnetostrictive Materials,* (New York: Academic Press, 2000).

4 D.C. Jiles, *Introduction to Magnetism and Magnetic Materials*. 2nd ed., (London: Chapman and Hall, 1990), p. 440.

5 B.D. Cullity, *Introduction to Magnetic Materials,* (Boston: Addison-Wesley, 1972).

6 A.E. Clark, 'Magnetic and Magnetoelastic Properties of Highly Magnetostrictive Rare Earth-Iron Laves Phase Compounds', *American Chemical Society,* (1974), p. 1015-29.

7 G. Herzer, 'Anisotropies in Soft Magnetic Nanocrystalline Alloys', *Journal of Magnetism and Magnetic Materials,* 294 (2005), p. 99-106.

8 M. Wada, H.H. Uchida, Y. Matsumura, H. Uchida, and H. Kaneko, 'Preparation of Films of (Tb,Dy)Fe_2 Giant Magnetostrictive Alloy by Ion Beam Sputtering Process and Their Characterization', in *Thin Solid Films:13th International Vacuum Congress and 9th International Conference on Solid Surfaces*, (Conference: Elsevier, 1996), p. 503-06.

9 G.P. McKnight, and G.P. Carman, 'Large Magnetostriction in Terfenol-D Particulate Composites with Preferred [112] Orientation', in *Proceedings of the SPIE: Smart Structures and Materials 2001: Active Materials: Behavior and Mechanics*, (Conference: SPIE-Int. Soc. Opt. Eng, 2001), p. 178-83.

10 N.J. Grabham, S.P. Beeby, and N.M. White, 'The Formulation and Processing of a Thick-Film Magnetostrictive Material', *Measurement Science & Technology,* 13 (2002), p. 59-64.

11 V.V. Dabhade, T.R. Rama Mohan, and P. Ramakrishnan, 'Nanocrystalline Titanium Powders by High Energy Attrition Milling', *Powder Technology,* 171 (2007), p. 177-83.

12 P. de la Presa, M. Multigner, M. P. Morales, T. Rueda, E. Fernandez-Pinel, and A. Hernando, 'Synthesis and Characterization of Fept/Au Core-Shell Nanoparticles', *Journal of Magnetism and Magnetic Materials,* 316 (2007), p.753-55.

13 F. Antolini, A. Ghezelbash, C. Esposito, E. Trave, L. Tapfer, and B.A. Korgel, 'Laser-Induced Nanocomposite Formation for Printed Nanoelectronics', *Materials Letters,* 60 (2006), p. 1095-98.

14 A.L. Rogach, A. Eychmuller, J. Rockenberger, A. Kornowski, H. Weller, L. Troger, M. Y. Gao, M. T. Harrison, S. V. Kershaw, and M. G. Burt, 'Thiol-Capped Cdse and Cdte Nanoclusters: Synthesis by a Wet Chemical Route, Structural and Optical Properties', in *Microcrystalline and Nanocrystalline Semiconductors*, (Conference: Mater. Res. Soc, 1998), p. 365-70.

15 W. Mahoney, M.D. Kempe, R.P. Andres, R. Bormann, G. Mazzone, R.D. Shull, R.S. Averback, R.F. Ziolo, R. Bormann, G. Mazzone, R.D. Shull, R.S. Averback, and R.F. Ziolo, 'Aerosol Synthesis of Metal and Metal Oxide, Nitride and Carbide Nanoparticles Using an Arc Evaporation Source', in *Metastable Phases and Microstructures,* (Conference: Mater. Res. Soc, 1996), p. 65-70.

16 D.B. Chrisey, and G.K. Hubler, *Pulsed Laser Deposition of Thin Films* (New York: John Wiley and Sons Inc., 1994).

17 T.G. Dietz, M.A. Duncan, D.E. Powers, and R.E. Smalley, 'Laser Production of Supersonic Metal Cluster Beams', *Journal of Chemical Physics,* 74 (1981), p. 6511-12.

18 M.F. Becker, J.R. Brock, C. Hong, D.E. Henneke, J.W. Keto, L. Jaemyoung, W.T. Nichols, and H.D. Glicksman, 'Metal Nanoparticles Generated by Laser Ablation', in *Nanostructured Materials*, (Conference: Elsevier, 1998), p. 853-63.

19 J.C. Miller, *Laser Ablation: Principles and Application*. ed. by R.M. Osgood, (Berlin: Springer, 1994), p. 187.

20 M. Ohring, *Material Science of Thin Films: Deposition and Structure*. 2nd ed., (New York: Academic Press, 2001), p. 800.

21 V.A. Marple, and K. Willeke, 'Impactor Design', *Atmospheric Environment,* 10 (1976), p. 891-96.

22 D.E. Henneke, 'Nanoparticles Produced Via Laser Ablation of Microparticles', Dissertation, University of Texas at Austin, (2001).

23 H. Chong, W.T. Nichols, D.T. O'Brien, M.F. Becker, D. Kovar, and J.W. Keto, 'Supersonic Jet Deposition of Silver Nanoparticle Aerosols: Correlations of Impact Conditions and Film Morphologies', *Journal of Applied Physics,* 101 (2007), p. 64902-61.

24 M.F. Becker, J.R. Brock, J.W. Keto, 'Process for the Production of Nanoparticles', US Patent 5,585,020, (1996).

25 J. Lee, M.F. Becker, and J.W. Keto, 'Dynamics of Laser Ablation of Microparticles Prior to Nanoparticle Generation', *Journal of Applied Physics,* 89 (2001), p. 8146-52.

26 W.T. Nichols, G. Malyavanatham, D.E. Henneke, D.T. O'Brien, M.F. Becker, and J.W. Keto, 'Bimodal Nanoparticle Size Distributions Produced by Laser Ablation of Microparticles in Aerosols', *Journal of Nanoparticle Research,* 4 (2002), p. 423-32.

27 W.T. Nichols, 'Production and Controlled Collection of Nanoparticles: Toward Manufacturing of Nanostructured Materials', Dissertation, University of Texas at Austin, (2002).

28 J.D. Snodgrass, McMaster, O. Dale, ' High Performance Rare Earth-Transition Metal Magnetostrictive Materials ', US Patent 6,273,966, (2001).

29 S. Svanberg, *Atomic and Molecular Spectroscopy: Basic Aspects and Practical Applications*. 3rd ed. Vol. 6, *Atomic, Optical, and Plasma Physics* (Berlin: Springer, 2001), p. 58.

30 R.E. March, 'Quadrupole Ion Trap Mass Spectrometry: A View at the Turn of the Century', *International Journal of Mass Spectrometry,* 200 (2000), p. 285-312.

31 H. Chong, 'Supersonic Jet Deposition of Laser Ablated Silver Nanoparticles for Mesoscale Structures', Dissertation, University of Texas at Austin, (2006).

32 J. Clarke, *Squid Sensors: Fundamentals, Fabrication and Applications*. ed. by H. Weistock, (Boston: Kluwer Academic Publishers, 1996).

33 R. Grossinger, H. Sassik, D. Holzer, and N. Pillmayr, 'Magnetic Characterization of Soft Magnetic Materials--Experiments and Analysis', *Journal of Magnetism and Magnetic Materials,* 254-255 (2003), p. 7-13.

34 E. du Tremolet de Lacheisserie, *Magnetostriciton: Theory and Applications of Magnetoelasticity*, (Boca Raton: CRC Press, 1993).

35 D.T. O'Brien, 'Laser Ablation of Terfenol-D Microparticle Aerosol and Subsequent Supersonic Nanoparticle Impaction for Magnetostrictive Thick Films', Dissertation, University of Texas, (2006).

36 K. Halback, 'Design of Permanent Multipole Magnets with Oriented Rare Earth Cobalt Materials', *Nuclear Instruments and Methods,* 169 (1980), p. 1-10.

37 A.G. Jenner, J.P. Hayes, L.A. Stone, H.V. Snelling, and R.D. Greenough, 'Pulsed Laser Deposition-an Alternative Route to the Growth of Magnetic Thin Films', in *Applied Surface Science Surface Processing: Laser, Lamp, Plasma*, (Conference: Elsevier, 1999), p. 408-12.

38 Q. Su, J. Morillo, Y. Wen, and M. Wuttig, 'Young's Modulus of Amorphous Terfenol-D Thin Films', *Journal of Applied Physics,* 80 (1996), p. 3604-06.

39 N.H. Duc, K. Mackay, J. Betz, Z. Sarkozi, and D. Givord, 'Magnetic and Magnetostrictive Properties in Amorphous $(Tb_{0.27}Dy_{0.73})(Fe_{1-X}Co_X)_2$ Films', *Journal of Physics: Condensed Matter,* 12 (2000), p. 7957-68.

40 A. Speliotis, O. Kalogirou, and D. Niarchos, 'Magnetostrictive Properties of Amorphous and Partially Crystalline Tbdyfe Thin Films', in *Journal of Applied Physics 41st Annual Conference on Magnetism and Magnetic Materials*, (Conference: AIP, 1997), p. 5696-98.

41 J. Koch, S. Schlamp, T. Rosgen, D. Fliegel, and D. Gunther, 'Visualization of Aerosol Particles Generated by near Infrared Nano- and Femtosecond Laser Ablation', *Spectrochimica Acta Part B: Atomic Spectroscopy,* 62 (2007), p. 20-29.

42 P.A. Dowben, W. Ning, N. Palina, H. Modrow, R. Muller, J. Hormes, Y.B. Losovyj, M. Chipara, O. Puglisi, R. Skomski, F.R. Jones, B.S. Hsiao, M. Chipara, O. Puglisi, R. Skomski, F.R. Jones, and B.S. Hsiao, 'Surface Segregation in Multicomponent Clusters', in *Degradation Processes in Nanostructured Materials. Symposium (Materials Research Society Symposium Proceedings Vol.887)* (Conference: Materials Research Society, 2005), p. 209-20.

43 A.E. Clark, and H.S. Belson, 'Giant Room-Temperature Magnetostrictions in $TbFe_2$and $DyFe_2$', *Physical Review B (Solid State),* 5 (1972), p. 3642-44.

44 P. Farber, and H. Kronmuller, 'Crystallization Behaviour and Magnetic Properties of Highly Magnetostrictive Fe-Tb-Dy Thin Films', *Journal of Magnetism and Magnetic Materials,* 214 (2000), p. 159-66.

45 S. Linderoth, 'Synthesis and Properties of Amorphous and Nanocrystalline Alloys', in *Science of Metastable and Nanocrystalline Alloys. Structure, Properties and Modelling. Proceedings of the 22nd Riso International Symposium on Materials Science*, (Conference: Riso Nat. Lab, 2001), p. 69-88.

46 C. Polak, R. Groessinger, H. Sassik, and G. Herzer, 'Comparison of the Magnetic Properties of Fe-Based Amorphous and Nanocrystalline Ferromagnets', *Journal of Magnetism and Magnetic Materials,* 104-07 (1992), p. 100-02.

47 K. Ried, M. Schnell, F. Schatz, M. Hirscher, B. Ludescher, W. Sigle, and H. Kronmueller, 'Crystallization Behaviour and Magnetic Properties of Magnetostrictive Tb Dy Fe Films', *Physica Status Solidi A,* 167 (1998), p. 195-207.

48 M. Wada, H. Uchida, and H. Kaneko, 'Effect of Annealing Treatment of the $Tb_{0.3}Dy_{0.7}Fe_2$ Thin Films on the Magnetic and Magnetostrictive Characteristics', in *Journal of Alloys and Compounds: International Conference on Giant-Magnetostrictive Materials- Fundamentals and Applications*, (Conference: Elsevier, 1997), p. 169-73.

49 A. Speliotis, and D. Niarchos, 'Magnetostrictive Properties of Amorphous and Crystalline Tb Dy Fe Thin Films', in *Sensors and Actuators A (Physical) 4th European Magnetic Sensors and Actuators Conference EMSA 2002*, (Conference: Elsevier, 2003), p. 298-301.

50 G. Herzer, 'Nanocrystalline Soft Magnetic Materials', (Conference: Elsevier, 1995), p. 133-36.

51 C. Huang, 'Supersonic Jet Deposition of Laser Ablated Silver Nanoparticles for Mesoscale Structures', Dissertation, University of Texas at Austin, (2006).

52 R.B. van Dover, E.M. Gyorgy, R.P. Frankenthal, M. Hong, and D.J. Siconolfi, 'Effect of Oxidation on the Magnetic Properties of Unprotected TbFe Thin Films', *Journal of Applied Physics,* 59 (1985), p. 1291-96.

53 H. H. Uchida, V. Koeninger, H. Uchida, M. Wada, H. Funakura, Y. Matsumura, T. Kurino, and H. Kaneko, 'Preparation and Characterization of (Tb,Dy)Fe/Sub 2/ Giant Magnetostrictive Thin Films for Surface Acoustic Wave Devices', in *Journal of Alloys and Compounds 10th International Conference on Internal Friction and Ultrasonic Attenuation in Solids,* (Conference: Elsevier, 1994), p. 455-59.

Vita

Dat Truong Ma was raised by his parents, Thuy and Khanh Ma, in Salem, IL. He graduated from James Bowie High School in May of 1997. His research career began in June of 2000 as an undergraduate research assistant while at the University of Texas at Austin. After completing his B.S. in mechanical engineering in 2002, he remained in Austin, TX to work under the supervision of Desiderio Kovar. He received his M.S. degree in materials science and engineering (MSE) in 2005 and Ph.D. in MSE in 2007 at the University of Texas at Austin.

Permanent address: 7704 Rochester Lane, Arlington, TX 76002
This dissertation was typed by the author.